Chair of Materials Physics

Master's Thesis

A laboratory total scattering approach for studying short-range order in a novel precipitation-strengthened compositionally complex alloy

Nicolas Erwin Bauer, BSc

January 2024

MONTANUNIVERSITÄT LEOBEN
www.unileoben.ac.at

EIDESSTATTLICHE ERKLÄRUNG

Ich erkläre an Eides statt, dass ich diese Arbeit selbständig verfasst, andere als die angegebenen Quellen und Hilfsmittel nicht benutzt, und mich auch sonst keiner unerlaubten Hilfsmittel bedient habe.

Ich erkläre, dass ich die Richtlinien des Senats der Montanuniversität Leoben zu "Gute wissenschaftliche Praxis" gelesen, verstanden und befolgt habe.

Weiters erkläre ich, dass die elektronische und gedruckte Version der eingereichten wissenschaftlichen Abschlussarbeit formal und inhaltlich identisch sind.

Datum 22.01.2024

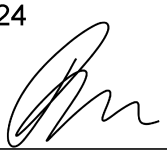

Unterschrift Verfasser/in
Nicolas Erwin Bauer

Danksagung

Die vorliegende Masterarbeit entstand größtenteils am Materials Center Leoben (MCL) im Rahmen eines betrieblichen Projekts. Daher bedanke ich mich für die finanzielle Unterstützung im Rahmen des COMET-Programms im K2 Zentrum „Integrated Computational Material, Process and Product Engineering (IC-MPPE)“ (Projektnummer 859480). Dieses Programm wird von den österreichischen Bundesministerien für Klimaschutz, Umwelt, Energie, Mobilität, Innovation und Technologie (BMK) und für Digitalisierung und Wirtschaftsstandort (BMDW), vertreten durch die österreichische Forschungsfördergesellschaft (FFG), und den Bundesländern Steiermark, Oberösterreich und Tirol gefördert.

Mein besonderer Dank gebührt meinem Betreuer Dr. Gerald Ressel, der mir immer das richtige Maß an konstruktiver Kritik und Motivation vermittelt hat. Bei meinem Zweitbetreuer Univ.-Prof. Dr. Jozef Keckes bedanke ich mich für die Unterstützung meiner Arbeit sowie für die Ermöglichung einer zweitägigen Strahlzeit am Deutschen Elektronen-Synchrotron (DESY) in Hamburg.

Weiters danke ich Dr. Paul Angerer und Bernhard Friessnegger vom MCL, die den technischen Teil der Arbeit maßgeblich vorangetrieben haben. Dr. Norbert Schell und Dr. Andreas Stark vom Helmholtz-Zentrum Hereon danke ich für die Unterstützung bei Messungen am DESY. Zuletzt ergeht ein herzliches Dankeschön an Dipl.-Min.in Dr.in rer.nat. Klaudia Hradil von der Technischen Universität Wien sowie Prof. Dr. Reinhard Neder von der Friedrich-Alexander-Universität Erlangen-Nürnberg. Sie haben keine Zeit und Mühe gescheut, um bei wichtigen Fragen Rat zu geben.

Ein ganz besonderer Dank geht an meine Familie für ihre bedingungslose Unterstützung während meines ganzen Studiums. Zu guter Letzt möchte ich mich bei meiner Freundin Carmen bedanken. Du hast mir immer Zuversicht gegeben, hast in schwierigen Phasen Verständnis für meine Sorgen gezeigt und mich immer ermutigt meinen Weg konsequent weiterzugehen. Danke für alles!

Leoben/Graz, am 22.01.2024

Table of Contents

Nomenclature and List of abbreviations

Term/abbreviation	Definition
(*hkl*)	crystallograhic plane with Miller indices *h*, *k* and *l*
(HR-)TEM	(High-resolution) Transmission electron microscopy/microscope
(X)NN	Nearest neighbor; Second (X=2), third (X=3) nearest neighbor
2θ	Scattering angle (angle between incident and scattered wave vector)
ADP	Atomic displacement parameter
APT	Atom-probe tomography
at.%	Atomic percent
BCC	Body-centered cubic
BSD	Back-scattered electron detector
δ_1, δ_2	Theoretical parameter describing linear/quadratic quadratic effect of correlated atomic motion on pair distribution function at high/low temperatures (software PDFgui)
CCA	Compositionally complex alloy
D8-1, D8-2	Laboratory settings for X-ray total scattering measurements conducted with diffractometer D8 Discover A25 from Bruker AXS
DESY	Deutsches Elektronen-Synchrotron
EBSD	Electron back scatter diffraction
EDX	Energy-dispersive X-ray (spectroscopy)
ESRF	European Synchrotron Radiation Facility
$F(Q)$	Reduced total scattering structure function

$f(Q)$	Atomic scattering factor
FC	Furnace-cooled
FCC	Face-centered cubic (Space group: Fm-3m)
FE-SEM	Field-emission scanning electron microscope
FWHM	Full width at half maximum
$G(r)$	(Reduced) pair distribution function
γ	Face-centered cubic matrix phase in Ni-Ti binary alloy and the CCA investigated in this work
γ'	$L1_2$-structured coherent secondary phase
HE	High-energy …
HEA	High-entropy alloy
HIP	Hot-isostatic pressing
HT	High-temperature …
I	(Measured) scattered intensity
$i…n$	component/element/data point index
I_{coh}	Coherent scattered intensity
ICP-OES	Inductively coupled plasma optical emission spectroscopy
LRO	Long-range order
MASS	Motorized Anti-Scatter Shield
MCL	Materials Center Leoben Forschungs GmbH
N_{diff}	Number of diffracting crystallites
P07B	Setting for X-ray total scattering measurements using synchrotron radiation (0.14235 Å) at beamline P07B at Deutsches Elektronen-Synchrotron
PDF	Pair distribution function

PM	Powder-metallurgy/powder-metallurgical
Q	Reciprocal-space coordinate; diffraction vector
Q_{broad}	Theoretical parameter for instrument-related peak broadening in pair distribution function (software PDFgui)
Q_{damp}	Theoretical parameter for instrument-related peak damping in pair distribution function (software PDFgui)
Q_{max}	Maximum Q-value for Fourier transform of $F(Q)$ to $G(r)$
$Q_{maxinst}$	Termination value for fitting range of polynomial correction function (software PDFgetX3)
QA	Quenched and aged
r	Real-space coordinate; interatomic distance (also: radius of coordination shell in ordered structures)
R(-factor)	Discrepancy index between two datasets; goodness of fit for refinement of measured/observed data (e.g. Rietveld refinement, PDF fitting)
r_{poly}	Real-space coordinate controlling degree of polynomial correction function (software PDFgetX3)
$S(Q)$	Total scattering structure function
SA	Solution annealing/solution-annealed
SE	Secondary-electron (detector)
SEM	Scanning electron microscopy/microscope
σ	Width parameter of Pseudo-Voigt fit function
σ_{PS}	Statistical error due to particle statistics
SRO	Short-range order
SS	Solid solution

$\langle u^2 \rangle$	Mean (isotropic) square atomic displacement
VCT	Variable Counting Time
vol.%	Volume percent
WQ	Water-quenching, water-quenched
wt.%	Weight percent
XRD	X-ray diffraction
XTS	X-ray total scattering
φ	Debye-Scherrer azimuthal angle

Abstract

Precipitation-strengthened compositionally complex alloys (CCAs), which are derived from the novel material class of high-entropy alloys (HEAs), show high potential for demanding high-strength high-temperature applications, but some of their properties such as serrated plastic flow are peculiar. The local ordering phenomenon termed short-range order (SRO) of different elements such as Ni and Ti may explain these peculiar properties. One method for studying such local phenomena that has risen to remarkable importance over the past few years is X-ray total scattering (XTS), or pair distribution function (PDF) analysis.

In the present thesis, first, a robust laboratory approach for PDF analysis devised at Materials Center Leoben Forschung GmbH (MCL) is presented and applied to Ni powder. The generated laboratory PDF data of Ni was validated with success against benchmark data generated with high-energy synchrotron radiation as well as data from literature.

The second aim of the present thesis is the investigation of ordering phenomena, in particular SRO, in a Ni-11 wt.% Ti binary alloy and a precipitation-strengthened CCA manufactured at MCL using the total scattering approach. Using Rietveld refinement and PDF refinement of both laboratory and synchrotron data in combination with scanning electron microscopy (SEM) and energy-dispersive X-ray spectroscopy (EDX), the evolution of γ' precipitation in the CCA was investigated in detail. The findings indicate that in the most rapidly quenched states of the CCA, early stages of γ' precipitation can be observed in the form of SRO, extending over only a few nanometers and acting as a precursor for subsequent γ' formation. In PDF analysis of laboratory and synchrotron data, indirect evidence of the transition from SRO to long-range ordered (LRO) γ' precipitation in the investigated CCA was found.

Hence, the present thesis proves that the presented laboratory total scattering approach is a valuable tool for investigating the local atomic structure in polycrystalline materials of varying chemical complexity up to CCAs.

1. Introduction

High-entropy alloys (HEAs) are novel structural materials that have sparked high research interest in the past two decades for their often exceptional combination of mechanical properties. These alloys are usually designed to form single solid solutions and belong to the broader class of compositionally complex alloys (CCA). In recent years, it was sought to further optimize the properties of HEAs by precipitation strengthening. Precipitation-strengthened CCAs show outstanding thermal stability and mechanical properties that can be retained to high temperatures, rivalling those of common Ni-based superalloys [1,2]. This makes them extraordinarily promising materials for high-temperature applications.

While the origin of many peculiar properties of HEAs and CCAs can be attributed to effects stemming from the mixing of multiple elements with mismatching atomic sizes [1,3], established theories fail to describe phenomena such as serrated plastic flow [4], and local chemical ordering in solution-annealed (SA) states [5].

The local ordering phenomenon termed short-range order (SRO) may explain these phenomena and have significant effect on mechanical properties of the alloy. SRO describes the preferred formation of unlike atom pairs over few atomic lengths in an otherwise disordered structure. While studies on SRO in binary alloys have drawn quite some attention in the past decades [6–11], the research of SRO in compositionally more complex materials, especially in HEAs and CCAs, is still vague and in need of improvement.

For the analysis of SRO, methods are necessary that allow insight into the local atomic environments in a crystal structure. One of these methods that has risen to remarkable importance is the total scattering method, or pair-distribution function (PDF) analysis method. Total scattering method means that both the Bragg scattering, resulting from the long-range average structure, as well as the diffuse scattering, containing information on local deviations from the average structure, are measured from a sample using X-rays or neutron radiation. The PDF can be calculated directly from the total scattering data and gives a histogram of atomic pairs in the investigated structure on an atomic length scale.

For a long time, the necessary accuracy of such measurements could only be achieved with high-energy radiation sources, e.g. synchrotron radiation sources or spallation neutron sources, at external research facilities. However, due to their technological improvement over the recent years, it is finally possible to also perform in-house laboratory total scattering and PDF analysis of high quality using laboratory diffractometers without the need to outsource experiments to research facilities.

Hence, the first aim of this work is to present and assess a laboratory approach for PDF measurement at Materials Center Leoben (MCL) using a diffractometer D8 Discover from Bruker AXS. Generated laboratory PDF data for standard Ni powder shall be assessed with respect to comparative synchrotron radiation PDF data as well as data from literature.

Using the presented laboratory approach, the second aim is to investigate ordering effects, in particular possible SRO of Ni and Ti, both in a Ni-11 wt.% Ti binary alloy and a precipitation-strengthened CCA manufactured by MCL. For this, Rietveld and PDF analysis shall be used in combination with microstructural and chemical characterization methods. Finally, a valid argument shall be made about whether the determination of SRO in the investigated materials is possible using the PDF analysis method in combination with the laboratory approach.

2. Fundamentals

In this chapter, the fundamental concepts underlying this work will be explored. First, the concept of HEAs and CCAs is presented, and their characteristic and peculiar properties are elucidated. In a next step, the term SRO is defined and a clear distinction is made between short-range and long-range order (LRO). Finally, the total scattering approach, its formalism used in the present work, the concept and interpretation of the PDF, as well as experimental limitations and requirements for PDF analysis are presented.

2.1. High-entropy alloys and compositionally complex alloys

HEAs are a novel class of CCAs that are composed of five or more principal elements, with the concentration of each element typically in the range from 5 to 35 at.% [1–3,12–15]. First investigations of this alloy concept began in 1996, most notably resulting in two publications in 2004 by Yeh et al. [16] and Cantor et al. [17].

Originally, HEAs were designed with the goal of achieving single solid solution (SS) phases with simple crystal structures such as face-centered cubic (FCC) and body-centered cubic (BCC) [1,3,12,18]. If the phase composition of HEAs deteriorates from the single-phase SS case, the term CCA is preferred [1,9]. The formation of stable single SS phases in HEAs is regarded to be favored by the high configurational entropy resulting from the complex compositions of these alloys [1,3,12,15].

The configurational entropy per mole of an ideal (i.e. random) n-component SS is given by

$$\Delta S_{\mathrm{conf}} = -R_{\mathrm{gas}} \sum_{i=1}^{n} x_i \ln x_i \tag{2.1}$$

where x_i is the mole fraction of the i^{th} component, and R_{gas} is the universal gas constant, 8.314 J/K/mol.

In the equimolar case, i.e. $x_i \equiv 1/n$, this expression yields

$$\Delta S_{\text{conf}} = R_{\text{gas}} \ln n \tag{2.2}$$

which shows that increasing the number of principal elements in an alloy leads to an increase in configurational entropy. For a five-component equimolar SS alloy, $\Delta S_{\text{conf}} = 1.61 R_{\text{gas}}$. In line with this, an alternative definition of HEAs can be given where alloys are considered as HEAs when their ideal molar configurational entropy $\Delta S_{\text{conf}} > 1.5 R_{\text{gas}}$, which necessitates at least five principal elements [1,15].

The thermodynamic tendency of HEAs to form single SS phases can be inferred from the Gibbs free energy change upon mixing of multiple elements in an alloy:

$$\Delta G_{\text{mix}} = \Delta H_{\text{mix}} - T\Delta S_{\text{mix}} \tag{2.3}$$

ΔH_{mix} and ΔS_{mix} are the enthalpy and entropy of mixing, respectively, and T denotes the absolute temperature. The enthalpy of mixing is governed by the nature and strength of the atomic interactions [12]. The entropy of mixing, on the other hand, is mainly constituted by the configurational entropy, although there are other minor contributions (such as vibrational, magnetic, and electronic entropy) [1]. Hence, it can be readily seen from equation (2.3) that in alloys with a high configurational entropy such as HEAs, the entropy of mixing may dominate the enthalpy of mixing even at ambient temperature, thus favoring the formation of single disordered SS phases over ordered intermetallic phases.

While many single-phase HEAs such as CoCrFeMnNi and CoCrFeNi show outstanding toughness and ductility at cryogenic and ambient temperatures, their tensile strength, ductility, and fracture toughness at elevated temperatures are rather poor [19,20]. Hence, efforts have been made to apply strengthening methods known from traditional alloys to HEAs, where in particular precipitation-strengthening showed great effect [21–23].

Precipitation-strengthened CCAs are a class of materials derived from HEAs which combine the high-entropy concept with precipitation strengthening [24,25]. In these alloys, through specific alloying additions and targeted heat treatment, the

precipitation of ordered second-phase particles is achieved which are dispersed in a SS matrix and can result in different strengthening effects [26]. Among them, the coherent ordered $L1_2$-structured γ' phase is known from Ni-based superalloys to be crucial for the high-temperature creep resistance of these alloys due to its prominent long-term microstructural and thermal stability [27].

Precipitation-strengthened CCAs with a microstructure of FCC γ matrix and γ' precipitates were shown to possess superior mechanical properties at elevated temperature levels, especially exceptional creep resistance [24,25,28,29]. In particular, one γ'-strengthened CCA investigated by Chang et al. [30] with the nominal composition $Al_{3.31}Co_{27.27}Cr_{18.18}Fe_{18.18}Ni_{27.27}Ti_{5.78}$ was found to exhibit outstanding high-temperature tensile properties with a yield strength of 126 MPa at 1000 °C at a strain rate of 10^{-3} s^{-1}. Based on this alloy composition, a similar CCA was manufactured in a predecessor project at MCL via the powder-metallurgical (PM) route, which is investigated in this work.

The outstanding properties of HEAs and CCAs such as the aforementioned exceptional combination of toughness and ductility [31], as well as high wear resistance [32,33], high hardness [34,35], and low diffusivity enhancing creep strength [1,3], can mainly be attributed to the mixing of multiple principal elements with different atomic radii, stabilizing single SS phases with severe lattice distortion [1,2,36,37]. In particular, the outstanding strength, ductility and toughness of FCC-based HEAs can be correlated with the stacking fault energy (SFE) of the material, reflecting the local interactions of dislocations with the atomic structure [38].

However, established theories fail to account for peculiar phenomena found in HEAs and CCAs such as serrated plastic flow [4] and solute clustering [5] in solution-annealed states. Both of these phenomena have been linked to the atomic-scale ordering of certain atom types, which is collectively referred to as short-range order (SRO) [5,39].

2.2. Short-range order

2.2.1. Definition and distinction of short-range order

In a disordered SS phase of an alloy containing multiple elements, the constituent atoms are distributed randomly on the sites of a single underlying lattice, e.g. an FCC lattice. However, the atomic-scale occupation of the sites is never perfectly random. Instead, the number of like and unlike atom pairs will always differ to some degree from the statistical average [40]. This is collectively referred to as SRO, the concept of which was proposed initially by Cowley in 1950 [41].

The degree and type of pairwise SRO in a binary SS alloy of given composition $A_{x_A}B_{1-x_A}$ can be quantified using the SRO parameters α_{lmn} defined by Warren and Cowley [42]:

$$\alpha_{lmn} = 1 - \frac{N_{lmn}^{AB}}{x_A x_B C_{lmn} N} \tag{2.4}$$

where the parameters lmn denote a particular coordination shell around an A atom at the origin, x_A and $x_B = 1 - x_A$ are the mole fractions of A and B atoms in the binary alloy, N_{lmn}^{AB} is the number of A-B pairs that can be found in the coordination shell lmn around an A atom at the origin, C_{lmn} is the coordination number of coordination shell lmn, and N is the total number of A and B atoms in the structure.

Only for perfectly random occupation of the lattice sites with A and B atoms, $\alpha = 0$. An SRO parameter of $\alpha > 0$ indicates clustering of like atoms (predominance of A-A and B-B pairs), while $\alpha < 0$ indicates ordering of unlike atoms (predominance of A-B pairs).

For interatomic distances in the disordered phase extending a few atomic diameters (in the range of angstroms or a few nanometers), the SRO parameters tends to zero, hence the term 'short-range' order. In scattering experiments, SRO gives rise to low-intensity modulations in the background between Bragg peaks (termed 'diffuse scattering') the magnitude of which is directly related to the values of the SRO parameters [40,43].

Experimental results dating back to as early as the 1960s motivated the formulation of three principal models of SRO [44–46] which are shown in Figure 1 (adopted from [46]). In line with the definition of Cowley, the **statistical model** (left) describes a homogeneous order throughout the structure where the probability of finding a B atom in a given coordination shell around any A atom differs from the nominal composition. In contrast, the disperse and the micro-domain model describe heterogeneous SRO confined to nanoscale coherent ordered regions within a disordered matrix. While in the **disperse model** (middle), the ordered regions have a different composition than the matrix, the regions in the **micro-domain model** (right) have the same composition as the matrix, and are only distinguished from the matrix by the change in the degree of order. All of these models share the fully coherent interface between SRO regions and disordered matrix.

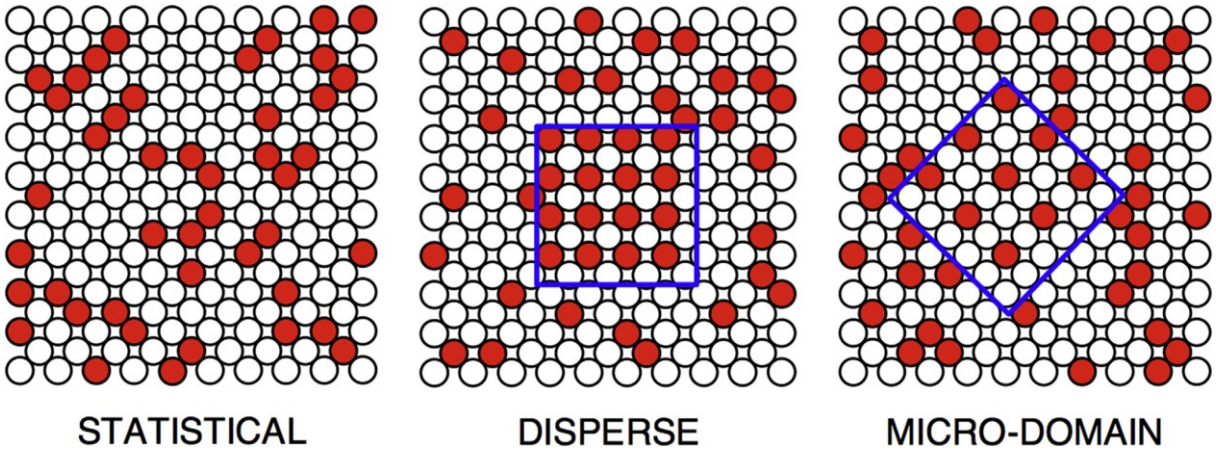

Figure 1: Examples of the three different models of SRO in a binary alloy as explained in the text (adopted from [46]). In the disperse and the micro-domain model, the SRO region is framed in blue.

Contrary to this, in ordered alloy phases atoms are distributed on the sites of specific sublattices in an ordered manner, i.e. a superstructure exits, over larger interatomic distances, usually at least some ten or hundred nanometers [43]. This type of long-ranging atomic correlation is termed long-range order (LRO), and gives rise to sharp Bragg peaks associated with the superstructure. Additionally, LRO phases can and will likely be incoherent with respect to the disordered matrix phase.

However, this distinction between SRO and LRO becomes blurred when the spatial extent of the two types of ordering becomes similar, e.g. when coherent particles,

exhibiting LRO in the sense of ordered distribution of atoms on sublattices, become nanosized and thus resemble the disperse SRO model. For lack of a clear quantitative distinction between what is 'long'-range and 'short'-range, there is an ongoing debate in literature as to whether such particles should be referred to as nanoscale LRO particles or SRO regions. In this work, however, such particles will be regarded as the latter, in line with the experimentally motivated SRO models above.

2.2.2. Research on SRO in alloys: History and state-of-the-art

Research on SRO in alloys commenced in the early 1960s, where diffuse scattering of X-rays was used to determine SRO in binary Cu-Al alloys in the Cu-rich composition range [44,47]. The SRO states of the investigated alloys were produced by slowly cooling, or by annealing after quenching from homogenization temperatures or deformation. Over time, evidence of SRO was also found in binary Ni-based alloys such as Ni-Mo alloys [11,48], Ni-Cr alloys [49–51] and Ni-Ti alloys [6,10] in the as-quenched state after annealing above a critical ordering temperature.

In more recent years, Ti-Al alloys such as Ti-6Al and Ti-6Al-4V were found to exhibit SRO from transmission electron microscopy (TEM), as well as atom probe tomography (APT) investigation [52–54]. SRO was also evident in Ti-6Al-4V alloy using *in-situ* straining experiments in TEM [55]. Similarly, *in-situ* TEM investigations revealed the interaction of SRO regions in the γ matrix phases of compositionally complex Ni-based superalloys with mobile dislocations [56,57]. Also, Monte Carlo (MC) simulations in combination with *ab-initio* calculations predicted SRO between Ni-Cr and Ni-Fe in equimolar ternary NiCrCo and quaternary NiCrCoFe model alloys [58].

With the development and rise of medium- (MEA) and high-entropy alloys, research effort in the field of SRO also branched into these novel classes of materials. Now, SRO has been widely reported in different types of MEAs and HEAs. For example, using energy-filtered TEM, Zhang et al. [59] were able to report structural features attributable to SRO in the NiCrCo MEA. Similarly, Chen et al. [60] used atomic-resolution imaging and chemical mapping via TEM to directly observe SRO of V-Co and V-Ni in the VCoNi MEA.

In equimolar FCC NiCrCoFe HEA, the formation of ordered nanodomains predicted by *ab-initio* calculations was confirmed by scanning TEM [61]. Furthermore, SRO in the form of nanosized γ′ precipitates enriched in Ni, Al and Cu was found in two different FCC AlCoCrCuFeNi-based HEAs from scanning TEM combined with APT [62] and from extended X-ray absorption fine structure (EXAFS) analysis [63]. Finally, Biermair et al. [64] found nanosized (2-3 nm) enrichments of Ni and Ti in SA and water-quenched (WQ) state of the FCC-based cast CCA $Al_{4.4}Co_{26}Cr_{19}Fe_{18}Ni_{27}Ti_{5.6}$ with highly comparable composition to the CCA investigated in this work, possibly hinting at SRO of Ni and Ti in this alloy.

2.2.3. Effects of SRO on material properties of HEAs and CCAs

As (statistical) SRO reflects fluctuations in local atomic configurations, it can profoundly affect the interaction with dislocations, and hence the deformation mechanism [65]. For example, it was found from *ab-initio* calculations that from tailoring the local chemical order in NiCrCo MEA, the SFE can be tuned in a wide range from -43 to 30 $mJ \cdot m^{-2}$ [66]. Improving on this, Zhang et al. [59] found that increasing SRO in thermomechanically processed NiCrCo MEA gave rise to both higher SFE and higher hardness of the alloy. Similarly, Neeraj and Mills [67] found that in Ti-6Al alloy, increase of SRO significantly increased creep strength, suggesting that the high creep resistance of HEAs may also partly be due to SRO.

Also, the presence of SRO can appreciably increase the slip barrier of dislocations. As it is generally understood, the destruction of SRO upon dislocation movement leads to an increase of the resistance for dislocation glide [68]. Hence, SRO strengthening can be a major contribution to the total strength of the alloy. For example, from atomistic simulations, Schön [69] estimated an SRO-induced increase of 100 MPa and above for the critical resolved shear stress of the main gliding system $\frac{a_0}{2}[111](0\bar{1}1)$ in the BCC HEAs VNbTaWAl and VNbWAl.

In FCC SS alloys, a correlation between SRO degree and the glide plane softening effect was found [70]. Here, SRO-induced dislocation glide resistance inhibits cross slip of dislocations and promotes planar slip, which was already shown to play a decisive role for simultaneously improving strength and ductility in Ni-Cr and Cu-Mn alloys [71,72].

The serrated plastic flow phenomenon refers to the occurrence of distinct serrations (i.e. steps) in the stress-strain curve during dynamic strain aging of a material in mechanical testing, and is usually regarded to be detrimental for the mechanical behavior of a material [4]. Besides some alloy classes such as Al alloys, Cu alloys, and steels, serrated flow has also been exhibited by various MEAs and HEAs containing small solute elements such as C [4], and was linked there to the SRO-induced dislocation glide resistance in combination with the interstitial 'hopping' of the small solute elements [39].

This brief review shall serve as an indication of the important, yet thus far neglected role of SRO in the mechanical properties of HEAs. Furthermore, by considering that through thermomechanical processing of the alloys, the degree of SRO can be tailored to some degree, this opens up new ways for tuning the mechanical behavior of HEAs [59].

2.3. Total scattering and pair distribution function analysis

2.3.1. Scattering theory: Bragg and diffuse scattering

Bragg scattering is the scattering arising from the periodic and discrete arrangement of atoms in a crystal structure, first described by Bragg [73]. According to Bragg's law, for a crystalline structure, maxima in intensity in a scattering pattern occur at specific angles θ which satisfy the condition

$$2d_{\mathrm{hkl}} \sin\theta = \lambda \tag{2.5}$$

where d_{hkl} is the interplanar spacing of a diffracting set of lattice planes (hkl), λ is the wavelength of incident radiation probing the structure, and θ is half the scattering angle 2θ between incident and scattered wave vector. Inherently, Bragg scattering only contains information about the long-range average structure of the material [74,75]. Information on local deviations from the idealized average structure is lost in this analysis, however.

Diffuse scattering comprises scattering contributions of any local deviations from the long-range average structure of a material, giving additional scattered intensity

that is distinct from Bragg scattering [41,74–77]. This must not be mistaken for background scattering coming from a sample's environment. Much rather, diffuse scattering completes the Bragg scattering to give the total scattering of a sample, containing all structural information on the material accessible by means of scattering. However, unlike the Bragg scattering which is strongly confined at certain discrete scattering angles 2θ, diffuse scattering is widely spread over the 2θ range [74,75]. Therefore, the diffuse scattering intensity is considerably weaker than the Bragg scattering, and consequently can be lost in the noise of the background.

The nature of diffuse scattering can perhaps most intuitively be understood from the attenuation of scattering caused by the thermal motion of particles, which was first described by Debye and Waller [78,79]. They found that, for a mean square displacement $\langle u^2 \rangle$ of atoms in the structure, the scattered intensity at a scattering vector Q is attenuated by the exponential Debye-Waller factor (DWF) of the form $\exp\left(-Q^2\langle u^2\rangle/3\right)$, and that the 'lost' intensity goes into the diffuse background [75]. Around 1950, diffuse scattering theory was extended by at least three groups of researchers: Huang [80] linked static site displacement in dilute solid solutions, resulting from atomic substitution, to diffuse scattering peaks. Warren et al. [77] noted a modulation of diffuse scattering with atomic size. And Cowley [41,42] remarked that SRO in solid solutions also results in variations in the observed diffuse scattering.

2.3.2. Definition and history

In the 1930s, the desire to study the local structure of amorphous materials, which by definition lack any long-range order, led to the development of the total scattering technique, in which both the Bragg and diffuse scattering from a sample are measured and analyzed simultaneously. Hence, the total scattering technique is a tool for structural analysis that gives access to the local structure of materials.

This becomes especially crucial for structural arrangements on the nanoscale, which is referred to as the 'nanostructure problem' [81]. The determination of nanostructures pushes standard crystallography to its limits since with increasingly smaller structures, the structural information evades into the diffuse scattering part. This necessitates more complex solutions than in the simple crystalline case, which only a

combination of the analysis of Bragg and diffuse scattering, i.e. the *total* scattering analysis, can give.

Since its advent, the total scattering method has been tied to the **pair distribution function (PDF)** analysis. In their seminal paper from 1927, Zernike and Prins [82] introduced the idea of a function that represents the probability that, at a distance *r* from the center of one particle (e.g. atom of type A, or a molecule), another particle (e.g. atom of type B, or another molecule) may be found. This probability function is the predecessor of the PDF as it is known today. Most importantly, this function can be directly determined from the scattering pattern by means of the Fourier transform.

The total scattering method, or, synonymously, the PDF analysis method, was first applied for structural studies of liquid and amorphous materials using X-rays. For example, liquid mercury was studied by Debye and Menke [83] in 1930, and liquid sodium by Tarasov and Warren [84] in 1936. In the following years, Warren and co-workers pushed forward the application of the method in local structure studies of silica glass, rhombic sulphur, carbon black, and water [85–88]. With the advent of spallation neutron sources in the late 1980s, the total scattering method was for the first time used to study disorder in quasi-crystalline [89,90] and crystalline materials [91]. In more recent years, the method has also been applied with some success to the study of phase transitions in perovskite materials, e.g. $Ba_{1-x}Sr_xTiO_3$ [92,93], and for the structural investigation of nanoparticles, e.g. Au nanoparticles [94], $Au_{144}(SR)_{60}$ nanoclusters [95,96], as well as PtPd [97], CdSe [98,99], and TiO_2 nanoparticles [100–102].

Only recently, it was begun to apply PDF analysis to CCAs and HEAs. For example, Guo et al. [103] used high-energy X-ray and neutron scattering to characterize the local atomic structure of BCC HEA ZrNbHf, while Owen et al. [104] used X-ray total scattering to investigate the local lattice strain in the FCC HEA CrCoFeMnNi. A few recent PDF studies on HEAs have also been aimed specifically at the investigation of possible SRO. For example, Zhang et al. [105] found no indication of SRO in a NiCoCr SS alloy from X-ray and neutron total scattering, but EXAFS revealed SRO between Cr-Ni and Cr-Co. In another attempt, Ma et al. [106] showed that a cluster-plus-glue atom model for SRO better approximated neutron total scattering data from quaternary HEAs containing Al, Co, Cr, Fe, and Ni than the average crystal structure,

indicating that SRO is present in these alloys. Still, PDF analysis using high-energy radiation, and much less in the laboratory, is far from an established method for investigation of SRO in HEAs.

2.3.3. Definition of the pair distribution function and total scattering formalism

The PDF G(r), as used in the present work, is related to the atomic structure through the relation

$$G(r) = 4\pi r \left[\rho(r) - \rho_0\right] \tag{2.6}$$

where ρ_0 is the atomic number density of the structure, and $\rho(r)$ is the atomic pair density, which gives the weighted density of neighbor atoms at a radial distance r from an atom at the origin [75,107–109]. The atomic pair density $\rho(r)$ is given by

$$\rho(r) = \frac{1}{4\pi r^2 N} \sum_i \sum_{j \neq i} \frac{f_i(Q) f_j(Q)}{\langle f(Q) \rangle^2} \delta(r - r_{ij}) \tag{2.7}$$

where the double sum over i and j goes over all atoms N in the structure; $f_i(Q)$ is the (X-ray) atomic scattering factor of atom i as a function of the magnitude of the scattering vector Q (described below); $\langle f(Q) \rangle$ is the average atomic scattering factor over all atom types in the structure; δ is the Dirac delta function; and r_{ij} is the distance between atoms i and j. Unless stated otherwise, the terms PDF and $G(r)$ will subsequently be used synonymously in this work.

As stated before, the PDF is directly obtained by Fourier transform of the total scattering pattern, i.e.

$$G(r) = \frac{2}{\pi} \int_0^\infty Q[S(Q) - 1] \sin(Qr)\, \mathrm{d}Q \tag{2.8}$$

where again Q is the magnitude of the scattering vector, and $S(Q)$ is the total scattering structure function. The scattering vector $\vec{Q}$ is the vector between incident and scattered wave vector. For coherent elastic scattering, its magnitude is given by

$$Q = \frac{4\pi \sin\theta}{\lambda} \tag{2.9}$$

where, as before, θ is half the scattering angle 2θ, and λ is the wavelength of incident radiation. In total scattering, measured intensity data is generally described in Q-space (i.e. reciprocal space) before Fourier transforming the data into the PDF described in r-space (i.e. real space).

The structure function $S(Q)$ is by definition obtained from the coherently scattered intensity $I_{\mathrm{coh}}(Q)$ of a structure according to

$$S(Q) = \frac{I_{\mathrm{coh}}(Q) - \langle f(Q)^2 \rangle + \langle f(Q) \rangle^2}{\langle f(Q) \rangle^2} \tag{2.10}$$

where $f(Q)$ is the atomic scattering factor, and the brackets denote an average over all atom types in the structure. Since $f(Q)$ and thus also $\langle f(Q) \rangle^2$ decreases rapidly with Q [75,110], the scattered intensity in the high-Q region of $S(Q)$ is naturally amplified with respect to the low-Q region. The mathematical limit of the $S(Q)$ function for $Q \to \infty$ is 1 (unity).

The function $Q[S(Q) - 1]$ is often defined as the reduced total scattering structure function $F(Q)$, i.e.

$$F(Q) = Q[S(Q) - 1] \tag{2.11}$$

which is then the direct Fourier transform of the PDF $G(r)$. The mathematical limit of the $F(Q)$ function for $Q \to \infty$ is 0 (zero).

In conclusion, the PDF gives a weighted histogram of the radial distances of atomic pairs in a structure, where the weight is given by the atomic scattering factors of each pair. As a reference for X-rays, the magnitude of the elemental scattering factors at low Q-values is approximately given by the atomic number Z of the element [110]. Hence,

for example, the contribution of Ni-Ni, Ni-Co, and Ni-Fe pairs to the X-ray PDF will be very similar ($Z = 26$, 27, 28 for Fe, Co, and Ni, respectively), but considerably different from the contributions of Ni-Al or Ni-Ti pairs ($Z = 13$, 22 for Al, and Ti, respectively). Importantly, this also means that X-ray PDFs will generally not give much contrast between elements with similar atomic number such as Ni, Co, and Fe, unless contrast is enhanced, e.g. by using radiation of tailored wavelength at the absorption edges for certain elements. Using neutron radiation is the easier option since the neutron scattering factors of elements are generally quite different from their X-ray counterparts.

It should also be stated here for reasons of completeness, that besides the PDF nomenclature chosen in the present work (which is the PDFgui/PDFgetX3 formalism [107,111]), various other total scattering formalisms and definitions of the PDF and related functions exist [108,109]. Moreover, generalizations of the PDF in higher dimensions have been formulated [75]. However, none of this will be further touched upon in this work.

2.3.4. The experimental pair distribution function in practice: Influences and limitations

The ideal PDF, as defined in equation (2.6), is only of theoretical nature. In practice, there will be several influences on the experimental PDF obtained from measured total scattering data, which will limit its accuracy, or will introduce errors to the PDF. While some influences can be mitigated by thoughtful experiment design or in subsequent data correction, others are inevitably entangled in the collected total scattering data, and a correction is hardly possible. Some important influences and possible error sources of experimental PDFs will be investigated in this section. As a visual aid, the effects of several structure- and instrument-related influences on the PDF mentioned in the text are shown in exemplary manner for simulated PDF data of Ni in Figure 2.

2.3.4.1 Physical influences

As mentioned before (section 2.3.1), the thermal (i.e. uncorrelated) motion of atoms in a structure gives rise to diffuse background in the scattering pattern. As a result, the ideal PDF (with Dirac delta peaks) is convoluted with a broadening

function, whose width is related to the mean square of the atomic displacement, $\langle u^2 \rangle$, which (in the isotropic case) is also called the (isotropic) atomic displacement parameter (ADP) [75]. Similarly, the correlated motion of atoms, e.g. lattice vibrations in crystalline structures, also leads to broadening of PDF peaks [75,107].

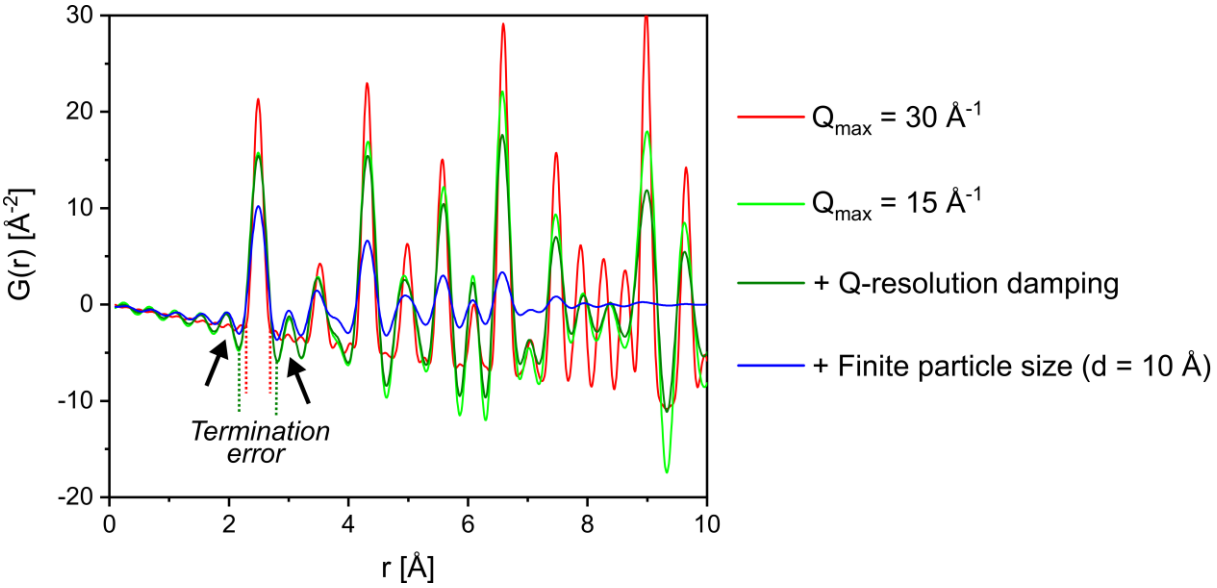

Figure 2: Overview of directly visible structure- and instrument-related effects on the PDF of Ni. Data was simulated with software PDFgui [107] using various built-in model parameters to account for the effects described in the text.

2.3.4.2 Structure- and sample-related influences

Structural coherence/crystallite size. Structural coherence in a material, described by the crystallite size in crystalline materials, is reflected both in the measured intensity data and in the PDF [112,113]. The renowned Scherrer formula relates the full width at half maximum FWHM(2θ) of a Bragg peak at scattering angle 2θ measured with X-rays of wavelength λ to the crystallite size D, FWHM(2θ) = $\lambda/(D \cos\theta)$ [114], i.e. Bragg peaks become ever broader with smaller crystallite size. The effect of this on the PDF is a decay of the magnitude in the PDF with r, until the PDF practically vanishes for $r > D$, i.e. for distances above the crystallite size [75,81,115]. This finite particle size effect is especially important for nanoparticles, as is shown in the simulated PDF of theoretical Ni nanoparticles with size $d = 10$ Å in Figure 2. In practice, this can be utilized for size determination of nanoparticles, as demonstrated in several recent works [95,96,98–102].

Microstrain. Microstrain can be caused in multi-phase alloys by lattice parameter mismatch between adjacent phases with semi- or incoherent interface such as the γ/γ′ interface in Ni-based superalloys [27]. Similar to decreasing crystallite size, increasing microstrain leads to broadening of Bragg peaks given by the formula FWHM(2θ) = 4e tan(θ), where $e = \Delta a/a_0$ is the magnitude of the microstrain as a result of the lattice parameter mismatch Δa, and a_0 is the un-strained lattice parameter [116]. The effect of microstrain on the PDF is a decrease of the PDF magnitude with r due to increased peak broadening [117].

Grain statistics. In PDF analysis, a high number of grains in diffracting position is crucial for achieving high statistical accuracy [118,119]. The statistical error due to grain statistics, σ_{GS}, can roughly be related to the number of diffracting crystallites in the sample, N_{diff}, by $\sigma_{GS} = \sqrt{N_{diff}}/N_{diff}$ [119]. For example, for the standard error, 2.3σ_{GS}, to be less than 5 %, N_{diff} should be greater than 2120 grains.

2.3.4.3 Instrument-related influences and error sources

Tuning the instrument parameters in order to mitigate erroneous influences on the PDF is the most crucial aspect for obtaining high-quality PDF data. The four most important instrument-related error sources in total scattering data collection are data termination, instrument resolution, counting statistics, and background scattering [75,120,121].

Termination errors are related to the fact that, in practice, the total scattering structure function $S(Q)$ cannot be collected up to a maximum Q-value of $Q_{max} = \infty$ as suggested by equation (2.6). Hence, for practical purposes, the equation for the experimental PDF $G(r)$ must be rewritten as

$$G(r) = \frac{2}{\pi} \int_{Q_{min}}^{Q_{max}} Q[S(Q) - 1] \sin(Qr)\, \mathrm{d}Q \tag{2.12}$$

where Q_{min} and Q_{max} are the lower and upper Q-limit, respectively, truncating the $S(Q)$ data used in the Fourier transform. The effect of a finite Q_{max} is the convolution of the ideal PDF with the Fourier transform of the truncation step function, i.e. with

$\mathrm{sinc}(r) = \sin(Q_{max}r)/(Q_{max}r)$ [75,121,122]. The termination error introduces spurious high-frequency oscillations into the PDF known as 'termination ripples' which are strongest at low r-values, and also leads to PDF peak broadening [74,75,120,123–132]. The 'termination ripples' are marked by arrows in Figure 2. With higher Q_{max}, the magnitude of the 'ripples' becomes ever smaller, which is why a high Q_{max} is always desired in PDF analysis. In theory, the termination error becomes negligibly small when $S(Q_{max})$ is sufficiently close to unity as a result of the attenuation due to the DWF, which is approximately the case for $Q_{max} > 1/\left(3\sqrt{\langle u^2\rangle}\right)$ [75]. For example, for an isotropic ADP of $\langle u^2\rangle = 0.0025$ Å^2, Q_{max} should be larger than 36 Å^{-1} for the termination error to be negligible.

In practice, Q_{max} is limited by the energy, or wavelength, of the employed radiation, and the maximum scattering angle 2θ accessible in the instrument. Additionally, the naturally increased noise at higher Q-values [75,120,121] means that often a compromise must be made to terminate the experimentally obtained $S(Q)$ data at an even lower Q_{max} value up to which the noise is still acceptable [75,121]. In order to maximize the Q-range in an X-ray total scattering experiment, radiation of high energy, or short wavelength, must be chosen.

Instrument *Q*-resolution. The inability of diffraction instruments to resolve all details leads to an instrument-related broadening of Bragg peaks, i.e. the true shape of a Bragg peak at position Q_0 is convoluted with an instrument resolution function, in the simplest case a Gaussian function with variance σ_G. As a result, the PDF is multiplied by an exponentially decaying envelope function $\exp\left(-\frac{1}{2}r^2\sigma_G^2\right)$ [75,120,121]. Hence, the effect of the finite instrument resolution is the damping of the experimental PDF with increasing r so that the magnitude of the PDF eventually reaches zero. In practice, the instrument resolution depends on a number of factors such as detector pixel solid angle, incident beam divergence, and diffractometer misalignment [75]. As a measure for the Q-resolution, the ratio $\Delta Q/Q$ can be used, where ΔQ is the difference between successive data points in the integrated scattering data.

Counting statistics. The estimated statistical error attributed to the observation of N counts of discrete scattering events is $\sigma_{CS} = \sqrt{N}/N$ [75,118,121]. Thus, in order to achieve good counting statistics, a large number of discrete scattering events must be observed. In PDF analysis, this is especially crucial for the data region at high

Q-values as, due to normalization, this data region contributes with higher weight to the PDF [120,123,126,127,133] (see section 2.3.3). In laboratory total scattering measurements, this requirement can be tackled with a variable counting time (VCT) strategy as proposed by te Nijenhuis et al. [134], i.e. by increasing counting time gradually from low to highest 2θ angles. For commonly used Si strip detectors, this necessitates long data collection times in the range of several hours. However, synchrotron radiation and large area detectors may reduce the necessary data collection time to several minutes or even seconds [120,124,125].

Background scattering. In total scattering analysis, emphasis is put on eliminating scattering contributions from the sample's environment (e.g. sample holder, air scattering) as they do not contain any structural information about the sample itself [75,100,120,123,126,127,132,133,135–137]. In transmission geometry, background scattering is usually eliminated by carrying out an independent scattering measurement without a sample (i.e. a measurement of the empty sample container) which only contains scattering from the apparatus and can then be subtracted from each subsequent measurement [75,121,126,129,133,134,136,138–140].

2.3.4.4 Data corrections

By definition, $S(Q)$ is related only to the *coherently* scattered intensity $I_{coh}(Q)$. Thus, the measured scattered intensity must be corrected for incoherent and inelastic scattering (e.g. Compton scattering, fluorescence), multiple scattering, absorption, polarization, and so on [75,111,123,132]. Usually, numerical corrections are applied in software for diffraction data evaluation such as DIFFRAC.EVA [141], GudrunX [142], and PDFgetX3 [111]. Additionally, in order to mitigate the termination error, $S(Q_{max})$ must be sufficiently close to unity. To ensure this, $S(Q)$ data can be normalized appropriately, as is the case in data reduction in PDFgetX3 [111].

2.3.5. Modelling and fitting of experimental pair distribution functions

When the atomic structure (i.e. the arrangement of atoms in space) of a material and the atomic scattering factors $f(Q)$ of all atom types in the structure are known, the ideal PDF of the material can readily be calculated from this information using equation (2.6). To account for the structure- and instrument-related influences

mentioned above, models exist which describe the deviations from the ideal PDF on a theoretical basis [75,107,117,121,129,143]. By using standard least-squares regression algorithms, the refinement of model structures through fitting of experimental PDF data is possible in software such as PDFgui [107] and DISCUS [115].

There, the effect of a finite Q_{max} is incorporated into the PDF calculation by convolving the ideal PDF with the box function, i.e. $\mathrm{sinc}(r) = \sin(Q_{max}r)/(Q_{max}r)$ [122]. The damping effect of the finite instrument resolution is approximated by the multiplicative term $\exp(-Q_{damp}^2 r^2/2)$ with the damping parameter Q_{damp}. The total width of a PDF peak, σ_{PDF}, at an interatomic distance r is described using the model equation

$$\sigma_{PDF} = \sigma_{ij}\sqrt{1 - \frac{\delta_1}{r} - \frac{\delta_2}{r} + Q_{broad}^2 r^2} \tag{2.13}$$

where σ_{ij} is the peak width calculated from the combined ADPs of atoms i and j, δ_1 and δ_2 are the linear and quadratic atomic correlation factors describing the broadening due to correlated motion of atoms (i.e. lattice vibrations) at different temperatures (δ_2 for low temperatures, δ_1 for high temperatures), and Q_{broad} is a parameter describing the broadening due to the finite instrument Q-resolution [144].

In practice, the instrumental parameters Q_{damp} and Q_{broad} are usually obtained from fitting of the experimental PDF of a highly crystalline (standard) material such as LaB_6 or Ni, and then fixed for subsequent refinements of data collected with the same setup.

2.3.6. Illustration of the pair distribution function of crystalline materials

The thoughtful interpretation of a PDF is just as important as the data acquisition and correction. For this, the reader is referred to Figure 3 which illustrates the connection between crystal structure and the PDF for the case of FCC Ni. In Figure 3a, the (100) plane of Ni is visualized, with coordination shells marked in green. In Figure 3b, a three-dimensional model of the corresponding unit cell is depicted. Figure 3c shows PDF data for FCC Ni calculated with software PDFgui [107] over the range from 0 to 15 Å with set values for the lattice parameter of $a_{lat} = 3.524$ Å, and

isotropic ADP $\langle u^2 \rangle = 0.003$ Å^2. Instrument-related model parameters were set to $Q_{max} = 30$ Å^{-1}, $Q_{damp} = 0.01$ Å^{-1} and $Q_{broad} = 0.01$ Å^{-1}.

As can be seen in Figure 3c, the PDF oscillates around zero, and shows peaks at certain interatomic distances r corresponding to the distances of atomic pairs in the structure visible in Figure 3a. For crystalline materials, these interatomic distances correspond to the radii of coordination shells around an atom at the origin and can be described by crystallographic directions [uvw]. For example, the peak at 2.50 Å corresponds exactly to the first coordination shell, i.e. the nearest-neighbor (NN) pairs, in the Ni structure. The equivalent crystallographic direction is [½ ½ 0]. In the same way, the peak at 3.52 Å corresponds to the second coordination shell, or the second-nearest-neighbor (2NN) pairs, which is equivalent to the [100] direction.

Structure-wise the height of a given peak in the PDF is determined by the coordination number for the corresponding coordination shell, and by the combined scattering factors of the atomic pairs of that shell. In the case of monatomic materials such as pure Ni, the scattering factor weight of each pair is the same. Additionally, as explained before, the magnitude of the PDF will be damped with increasing r as a result of the finite instrument resolution. This was accounted for in the calculation of the PDF by setting the damping parameter Q_{damp} to a moderate value of 0.01. As a result, the calculated PDF eventually reaches zero at an r-value of approximately 200 Å (not shown here).

The width of the PDF peaks depends on several factors including the thermal (i.e. uncorrelated) and the correlated atomic motion in the structure at a given temperature, as well as the broadening due to the finite Q_{max}, i.e. the termination error. In this example, the peak width was tuned by setting values for the (isotropic) ADP $\langle u^2 \rangle$ and Q_{max}.

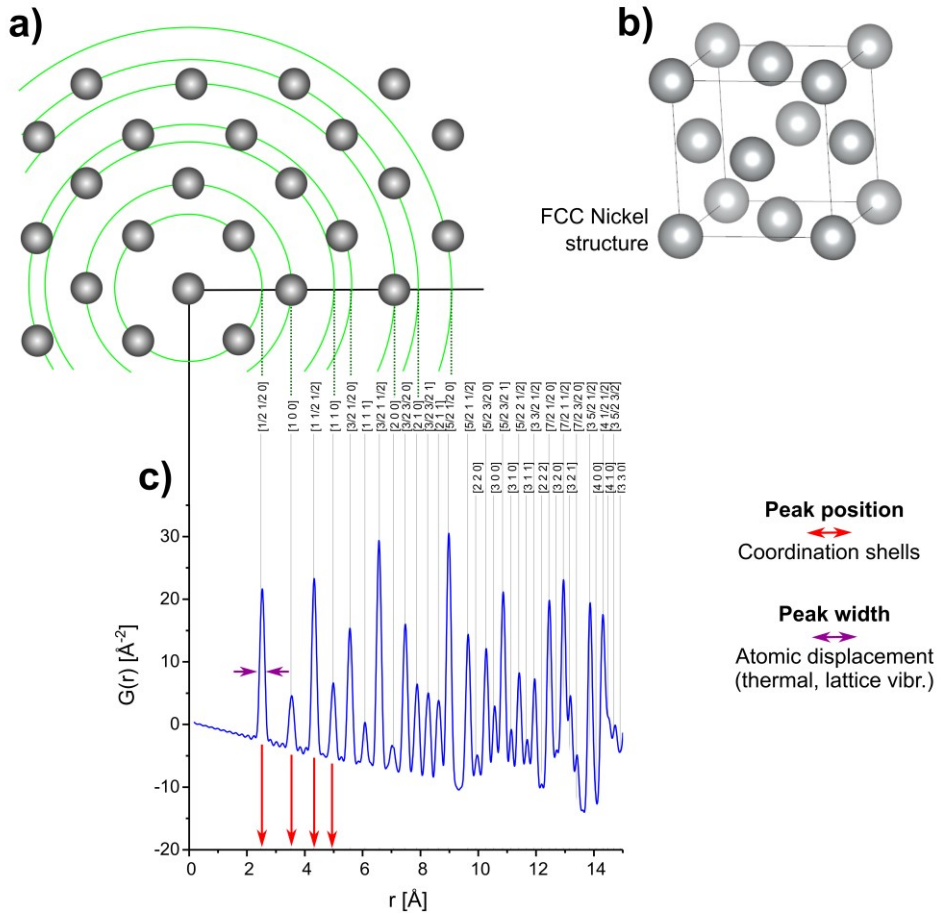

Figure 3: From crystalline structure to the PDF by the example of Ni. (a) (100) lattice plane of FCC Ni. (b) Three-dimensional model of FCC Ni unit cell. (c) PDF of Ni calculated with PDFgui from the model structure with Q_{max} = 30 Å^{-1}, Q_{damp} = 0.01 Å^{-1} and Q_{broad} = 0.01 Å^{-1}.

3. Experimental and computational methods

The approach of this work can be summarized as a complementary analysis of X-ray total scattering (XTS) data both in reciprocal space, i.e. scattering intensity as a function of scattering angle 2θ, and in real space, i.e. PDF analysis. XTS experiments were performed with an in-house diffractometer and at a high-energy synchrotron radiation beamline on samples from three different materials. PDFs were calculated from the collected scattering data. The experimental PDFs were then analyzed and compared in order to validate the in-house laboratory measurement, and characterize the local structure of the investigated samples. Additionally, the microstructure and chemistry of the samples was characterized by means of scanning electron microscopy (SEM) and energy-dispersive X-ray (EDX) spectroscopy.

3.1. Sample preparation

Samples were prepared from three materials with increasing compositional complexity: starting from pure Ni powder, followed by a binary Ni-11 wt.% Ti alloy, and finally the CCA containing Al, Co, Cr, Fe, Ni, and Ti.

The Ni-Ti alloy and the CCA were manufactured via the powder-metallurgical (PM) route from gas-atomized metallic powders using hot-isostatic pressing (HIP). Samples of different geometries (platelet, and cylindrical) were machined from the solution-annealed (SA) bulk material in both cases, and further heat treatment was conducted on these smaller samples. Using a quenching dilatometer DIL805L/A from BÄHR in vacuum with He as cooling gas, the cylindrical samples from Ni-Ti alloy and the CCA were SA at different temperatures for 30 min, and then quenched with distinct cooling times from 800 °C to 500 °C, $t_{8/5}$, ($t_{8/5}$ = 5, 10, 30, 100, 300 s). Additionally, one cylindrical sample of each material was quenched as fast as possible with no further constraints, where subsequent data analysis revealed that $t_{8/5}$ was approximately 2.5 s in this case. The series of SA samples from Ni-Ti alloy and the CCA quenched with varying cooling times are subsequently referred to as 'Ni-Ti series' and 'CCA series', respectively.

The solid samples from Ni-Ti alloy and CCA were then prepared for XTS analysis by conventional grinding. The cylindrical samples were grinded to half their original

diameter, i.e. to 2 mm thickness. For microstructural and chemical characterization, the samples were hot-mounted, and ground using up to 2500 grade SiC grit-paper. Polishing was done using 3 μm and 1 μm diamond suspensions as well as 0.25 μm silicon oxide suspension, before the sample surfaces were plasma-cleaned as a final step.

An overview of specifications of the samples investigated in this work, showing their labels used in this thesis, their dimensions, and the state of the sample material achieved with heat treatment, is given in Table 2. A more specific description of sample preparation for each material is given in the dedicated sections to follow.

3.1.1. Nickel powder

Commercially available Ni powder with spherical grain shape, grain size below 40 μm (d_{50} = 12.9 μm), and purity of > 99.8 % was obtained from Alfa Aesar, Thermo Fisher Scientific Inc., Germany. For laboratory XTS analysis, the metallic powder in the as-delivered state was distributed evenly in the platelet-shaped cavity with dimensions 70 x 25 x 1 mm^3 of a sample holder made from glass, compressed by hand, and smoothened with a razor blade.

3.1.2. Ni-Ti binary alloy

For the binary Ni-Ti alloy with a nominal composition of 89 wt.% Ni and 11 wt.% Ti, metallic powder was Ar gas-atomized from the liquid phase with appropriate composition at NANOVAL GmbH & Co. KG, Germany. The smaller grain fraction with d_{50} = 19.0 μm was then consolidated by HIP (1140 °C, 6 h, 100 MPa) in a sealed, evacuated cylindrical capsule with a diameter of 40 mm and a length of 45 mm.

A semi-cylindrical specimen was machined from the bulk material. From this specimen, smaller cylindrical samples (Ni-Ti SA 1200-X, X = Q, 5, 10, 30, 100, 300) with a diameter of 4 mm and a length of 40 mm were eroded and subsequently subjected to further heat treatment, as aforementioned. Additionally, a quarter-cylindrical specimen was machined from the bulk material and SA at 1200 °C for 30 min, followed by furnace cooling (FC) of the specimen with a cooling time of $t_{8/5}$ = 19,560 s. From this second specimen, a platelet-shaped sample (Ni-Ti SA FC) was cut.

3.1.3. CCA investigated in this work

The CCA investigated in this work was manufactured in a predecessor project at MCL via the PM route. The metallic powder was Ar gas-atomized from the liquid phase of suitable composition at NANOVAL GmbH & Co. KG, Germany, which yielded a powder with d_{50} = 33.4 μm. The powder was then consolidated by HIP (1140 °C, 6 h, 207 MPa) in a sealed, evacuated cylindrical capsule with a diameter of 60 mm and a length of 200 mm, and the bulk material was homogenized. The chemical composition of the bulk alloy was determined by inductively coupled plasma-optical emission spectrometry (ICP-OES). The overall composition of the alloy, showing only the normalized atomic fractions of the main elements Al, Co, Cr, Fe, Ni, and Ti, is given in Table 1.

Table 1: Chemical composition of the CCA investigated in this work in at.% determined by ICP-OES. Only main elements are shown.

Element	Al	Co	Cr	Fe	Ni	Ti
Atomic fraction[a] [at.%]	3.29	27.38	18.05	18.13	27.29	5.87

Cylindrical samples (CCA SA 1050-X, X = Q, 5, 10, 30, 100, 300) with a diameter of 4 mm and a length of 40 mm were eroded from the bulk material and subjected to further heat treatment, as aforementioned. Additionally, a cylindrical specimen was machined from the bulk material, SA at 1050 °C for 30 min, followed by WQ and tempering at 750 °C for 50 h. From this quenched & aged (QA) specimen, a platelet-shaped sample (CCA QA) was machined.

[a] Atomic fraction normalized with respect to sum of the measured fractions of elements in the table.

Table 2: Specifications of samples investigated in the present work

Sample label	Dimensions [mm³]	Material state/ Heat treatment	Cooling time $t_{8/5}$ [s]
Ni (powder in cavity)	70 x 25 x 1	–	–
Ni-11 wt.% Ti binary alloy			
Ni-Ti SA 1200-Q	40 x 4 x 2	SA 1200 °C/30 min + cooling	~2.5
Ni-Ti SA 1200-5	"[b]	"	5
Ni-Ti SA 1200-10	"	"	10
Ni-Ti SA 1200-30	"	"	30
Ni-Ti SA 1200-100	"	"	100
Ni-Ti SA 1200-300	"	"	300
Ni-Ti SA FC	40 x 15 x 2	Machined from bulk material SA 1200 °C/30 min + FC	19,560
CCA			
CCA SA 1050-Q	40 x 4 x 2	SA 1050 °C/30 min + cooling	~2.5
CCA SA 1050-5	"	"	5
CCA SA 1050-10	"	"	10
CCA SA 1050-30	"	"	30
CCA SA 1050-100	"	"	100
CCA SA 1050-300	"	"	300
CCA QA	40 x 15 x 2	Machined from bulk material SA 1050 °C/30 min + WQ + aged 750 °C/50 h	–

[b] Sign " indicates that value above it is repeated

3.2. Methods for microstructural and chemical characterization

Microstructural characterization of selected Ni-Ti binary alloy and CCA samples was performed via SEM, and chemical characterization via EDX spectroscopy, both on a field-emission scanning electron microscope (FE-SEM) GeminiSEM 450 from ZEISS. For both Ni-Ti binary alloy and the CCA, selected samples were the cylindrical samples with maximum quenching rate (Q), and with cooling times $t_{8/5}$ = 30 s and 300 s. Additionally, the furnace-cooled Ni-Ti state (Ni-Ti SA FC) and the aged CCA state (CCA QA) were investigated.

SEM was performed using two sets of parameters. Acceleration voltage was set to 5 keV and 2 keV, sample current to 3 nA and 500 pA, and working distance to 8.5 mm and 3.3 mm, respectively. Resolutions ranged from 200 μm to 200 nm, and from 2 μm to 40 nm, respectively. With the first set of parameters, a secondary electron (SE) detector, back-scattered electron detectors (BSD), and an InLens-SE detector were applied. With the second set of parameters, the InLens-SE detector was used together with an InLens energy-selective BSD. For EDX spectroscopy, the first set of SEM parameters was used together with an Ultim Extreme silicon drift detector. Spectra were recorded for all identified phases of the microstructure.

Linear intercept grain sizes of the bulk samples were evaluated from SEM images with software Stream Desktop 2.5 from OLYMPUS in compliance with standard test method ASTM E112-13 [145]. More than 1,000 intercepts were obtained for each image, hence the relative error of grain size measurement can be estimated to be ± 5 % [146]. Quantitative phase analysis of the CCA states SA 1050-300 and QA was also performed using the same software.

3.3. X-ray total scattering (XTS) experiments

XTS experiments were conducted at two different facilities: Laboratory XTS experiments were performed with an in-house diffractometer using two different experimental settings at MCL. Complementary to this, XTS experiments using high-energy synchrotron radiation were performed at beamline P07B at the Deutsches Elektronen-Synchrotron (DESY) [147]. A synoptic comparison of the different experimental set-ups is given in Table 3.

3.3.1. Laboratory XTS experiments

Laboratory XTS experiments were performed using a diffractometer D8 Discover A25 from Bruker AXS with a Mo anode as X-ray source. The radiation used was that of the MoK$\alpha_{1,2}$ peak doublet with wavelengths of 0.7093 Å and 0.7136 Å, respectively. A Goebel mirror was applied in primary beam optics for parallel beam geometry and filtering of MoKβ radiation. Experiments were performed in symmetrical θ-θ reflection geometry, with a primary goniometer radius of 350 mm. Secondary goniometer radius was different, depending on the detector, as specified below. Samples were mounted onto a platelet-shaped sample holder made from glass. The sample stage was oscillated horizontally with an amplitude of 8 mm and a frequency of 10/s during the experiment.

On that basis, two different experimental settings were prepared, denoted as D8 Setting 1 (D8-1) and D8 Setting 2 (D8-2) subsequently.

(1) **D8 Setting 1 (D8-1)**: Scattering data was collected using a Si strip detector LYNXEYE XE-T from Bruker AXS in one-dimensional mode (opening angle 2.348 °, 192 channels acting as receiving slits with 0.012 ° angular width each) with a 0.6 mm primary slit, and a secondary 2.5 ° axial Soller slit. Secondary goniometer radius was equal to the primary radius of 350 mm in this setting. Additionally, a Motorized Anti-Air Scatter Shield (MASS) from Bruker AXS was mounted above the sample to shield off air scattering at low 2θ angles. Data collection over the total angular range of $5\,° < 2\theta < 150\,°$ was split into five subranges with varying counting time, 2θ step size, and shielding aperture of the MASS. As can be seen in Table 4 detailing the data collection strategy for setting D8-1, counting time was successively increased between the subranges from 0.75 to 12 s, while step size was increased from 0.01 to 0.06 °. Aperture of the MASS was gradually increased from 0.4 to 2.0 mm.

(2) **D8 Setting 2 (D8-2)**: Here, an area detector EIGER2 R 500K from Bruker AXS with 1024 x 512 pixels of pixel size 75 x 75 μm² on a sensitive area of 77.3 x 38.6 mm² was used in azimuth-optimized mode[c]. Primary beam was collimated two times with a 1 mm pinhole slit and a 1 mm snout-pinhole

[c] Azimuth-optimized mode: Detector was mounted so that the wider side of the sensitive area pointed in the direction of the azimuthal angle φ perpendicular to the 2θ scanning direction during scanning.

collimator to obtain a point focus. Secondary goniometer radius was decreased to 179.9 mm in this setting. The MASS had to be omitted in this setting. Scanning of the total angular range of $0\,° < 2\theta < 155\,°$ was split into six (overlapping) subranges. As shown in Table 5, the detector was moved along the goniometer circle first in steps of 1.25 ° up to 40 °, then 2.5 ° from 40 ° to the end, and the counting time per step was increased from 25 to 200 s between subranges.

Setting D8-2 was used for XTS measurements on all samples. In contrast, setting D8-1 was only used for comparative measurements on Ni powder, due to the inability in this setting to confine the lateral spot size of the beam onto the slimmer Ni-Ti binary alloy and CCA samples of 4 mm width.

For data evaluation, the software DIFFRAC.EVA version 6.0.0.7 from Bruker AXS was used. For setting D8-1, data from the individual subranges was combined and normalized to give the scattering intensity in counts per second. For setting D8-2, the collected two-dimensional frames were merged and the resulting data was integrated with a full cursor over the angular range of $3\,° < 2\theta < 150\,°$ with a step size of 0.01 °.

3.3.2. Synchrotron XTS experiments

Synchrotron XTS experiments were conducted in ambient atmosphere at beamline P07B at DESY [147] with high-energy synchrotron radiation of wavelength 0.14235 Å in transmission geometry. Due to missing harmonic rejection optics at this beamline, the radiation also contained a low amount of the second-order harmonic component with half the primary wavelength, i.e. with wavelength 0.07115 Å.

Ni powder was measured inside a plastic capsule. Additionally, a measurement of only the apparatus was done. The sample-to-detector distance (SDD) was refined to 375.3 mm using Ni as a calibrant [148].

Full Debye-Scherrer rings were recorded, with data collected over the angular range of $0\,° < 2\theta < 37.6\,°$ using a Perkin Elmer XRD 1621 Flat Panel detector with 2048 x 2048 pixels of size 200 x 200 μm^2 on a sensitive area of 409.6 x 409.6 mm^2. Spot size of the beam on the samples was set to the maximum value of 1.0 mm x 1.0 mm by opening the horizontal and vertical beam slits as wide as possible. Exposure time was 0.1 s per image, and 10 images were summed up for each measurement.

Azimuthal integration of the collected two-dimensional image data along the Debye-Scherrer azimuthal angle φ was performed using the software DIOPTAS version 0.54 [149]. Measured data of the apparatus was subtracted from every measurement.

Table 3: Overview of experimental settings for XTS measurements used in the present work

	Laboratory settings		**Synchrotron set.**
	D8-1	D8-2	P07B
Device/facility	Diffractometer D8 Discover A25 (Bruker AXS)		Beamline P07B at DESY
Radiation	MoK$\alpha_{1/2}$		Synchrotron
Wavelength [Å]	0.7093 (MoKα_1), 0.7136 (MoKα_2)		0.14235, 0.071175[d]
Energy [keV]	17.5		87.1
Geometry	Symmetrical θ-θ reflection		Transmission
Angular range (2θ) [°]	5-150	0-155	0-37.4
Maximum Q-value [Å^{-1}]	17.1	17.1	28.5
Detector system	Si strip detector LYNXEYE XE-T (Bruker AXS)	Area detector EIGER2 R 500K (Bruker AXS)	Area detector Perkin Elmer XRD 1621

Table 4: Data collection specifications of setting D8-1

D8-1 Subranges	**1**	**2**	**3**	**4**	**5**
Angular range [°]	5-15	15-49	49-103	103-122	122-150
Step size [°]	0.01	0.015	0.02	0.04	0.06
Counting time per step [s]	1.5	0.75	3	6	12
MASS aperture [mm]	0.4	0.4	0.5	0.9	2

[d] This is the second harmonic component of the synchrotron radiation at beamline P07B.

Table 5: Data collection specifications of setting D8-2

D8-2 Subranges	**1**	**2**	**3**	**4**	**5**	**6**
Angular range [°]	0-15	6.25-45	37.5-80	72.5-110	102.5-125	117.5-155
Step size of detector [°]	1.25	1.25	2.5	2.5	2.5	2.5
Counting time per step [s]	25	25	50	100	200	400

To quantify the particle statistics in the laboratory measurements of solid samples, the number of grains in the irradiated sample volume as a function of the scattering angle 2θ was estimated. For this, the irradiated sample volume as a function of 2θ was approximated as a cuboid with the length given by the beam footprint on the sample calculated from geometrical considerations (height of the beam was 0.6 mm), a constant width of 1 mm, and the depth approximated by the penetration depth of the used radiation (MoKα) in solid Ni. The penetration depth, i.e. the depth corresponding to 90 % attenuation of the incident intensity, as a function of 2θ was calculated with software AbsorbX from Bruker AXS. Also, the additional length component of 8 mm due to the oscillation of the sample was taken into account.

3.4. Computational methods

3.4.1. Analysis of XTS data

Fitting of selected peaks in the collected XTS data of Ni-Ti binary alloy and CCA samples was conducted to quantify peak height, relative peak intensities, and full width at half maximum (FWHM) of the peaks. In the case of laboratory XTS data, the presence of both MoKα_1 and MoKα_2 radiation was considered with the theoretically expected peak intensity ratio of 2:1.

Boundaries of the fitting range for each peak were automatically determined using a difference of Gaussians algorithm [150] on the scattering data. A linear background

was subtracted from the data in each fitting window. Peak shape was fit using a Pseudo-Voigt fit function, i.e. a linear combination of a Gaussian (G) and a Lorentzian component (L) [151–153], given by

$$pV(2\theta; 2\theta_0, A, \sigma, \eta) = (1-\eta)\ \frac{A}{\sigma_G\sqrt{2\pi}}\exp\left[-\frac{(2\theta-2\theta_0)^2}{2\sigma_G^2}\right] + \eta\ \frac{A}{\pi}\ \frac{\sigma}{(2\theta-2\theta_0)^2+\sigma^2} \tag{3.1}$$

where $2\theta_0$ denotes the center position of the peak, A is the amplitude, σ is the width parameter ($\sigma_G = \sigma/\sqrt{2\ln(2)}$), and η ($0 < \eta < 1$) determines the weight of the components. The parameters $2\theta_0$, A, σ, and η were refined in the peak fitting process.

Following the definition above, the FWHM of a fitted peak can be approximated by [154]

$$\text{FWHM} \cong 0.5346\sigma + \sqrt{0.2166\sigma^2 + \sigma_G^2} \tag{3.2}$$

The peak height was defined as the maximum intensity of the fitted peak profile with respect to the linear background in the fitting range of the peak.

In addition to this, Rietveld refinement of the collected XTS data was peformed using the software MAUD version 2.992 [155]. The structural data for η phase and TiC identified in certain Ni-Ti states from SEM and EDX analysis were retrieved from the Crystallography Open Database [156]. For lack of structural data from the literature, the γ matrix phase in case of Ni-Ti binary alloy was modelled as a disordered SS phase with FCC structure (space group $Fm\bar{3}m$) and the nominal composition of the alloy, i.e. 86.8 at.% Ni, and 13.2 at.% Ti. Similarly, for structural refinement of the CCA data, two crystalline phases, one for the disordered γ matrix with FCC structure (space group $Fm\bar{3}m$) and one for possibly present $L1_2$-ordered γ′ phase (space group $Pm\bar{3}m$), were created. The composition of the γ phase was modelled after the normalized atomic fractions of the main elements Al, Co, Cr, Fe, Ni, and Ti obtained from ICP-OES of the homogenized bulk material. The composition of γ′ phase was modelled after data for

actual γ′ phase present in the QA state of a similar CCA obtained from APT reconstructions in a predecessor project at MCL [64].

The background of the scattering data was interpolated between manually set and approximately linearly spaced data points. Sample-related peak broadening from crystallite size was considered. Crystallite orientation was assumed to be randomly distributed, i.e. no texture was considered.

Instrument-related peak broadening was accounted for by refinement of the Caglioti parameters U, V and W commonly used in Rietveld refinement, which describe the angular dependence of the FWHM of a diffraction peak at angle θ as [157,158]

$$\mathrm{FWHM}(\theta) = U\tan^2\theta + V\tan\theta + W \tag{3.3}$$

The goodness of Rietveld fits of the measured data was quantified using the well-established (weighted) profile R-factor given by [159]

$$R^2 = \frac{\sum_i w_i \left(y_{\mathrm{calc},i} - y_{\mathrm{obs},i}\right)^2}{\sum_i w_i \left(y_{\mathrm{obs},i}\right)^2} \tag{3.4}$$

where the index i goes over all datapoints, w_i is the weight of datapoint i, and $y_{\mathrm{calc},i}$ and $y_{\mathrm{obs},i}$ are the calculated and observed (i.e. measured) value, respectively. In the present work, w_i was uniformly set to 1, i.e. all datapoints were ascribed equal weight.

3.4.2. Calculation and analysis of experimental pair distribution functions

Experimental PDFs were calculated from the collected scattering data in the range from 0 to 300 Å using software PDFgetX3 version 1.1.2 [111]. $F(Q)$ data to include in the Fourier transform was truncated at $Q_{\mathrm{max}} = 16.9$ Å^{-1} and $Q_{\mathrm{max}} = 25.8$ Å^{-1} for the laboratory settings, and the synchrotron setting, respectively. This way, spurious and noisy signal at high Q-values was excluded and it was ensured that $F(Q_{\mathrm{max}})$ was close to zero. In both cases, the cut-off value for the data range of the $F(Q)$ correction polynomial, i.e. Q_{maxinst}, was set to the same value as Q_{max}. The limit value r_{poly}, which, together with Q_{maxinst}, controls the degree of the correction polynomial, was

subsequently set to yield a polynomial of degree 8 in both cases. The set values for the parameters, as listed in Table 6, were hereafter held constant for all evaluations within each XTS data set, i.e. laboratory or synchrotron data, respectively.

Table 6: Set parameter values for calculation of experimental PDFs with PDFgetX3

Experimental setting	**PDFgetX3 parameters** [111]		
	Q_{max} [Å^{-1}]	$Q_{maxinst}$ [Å^{-1}]	r_{poly} [Å]
Laboratory settings (D8-1, D8-2)	16.9	16.9	1.48
Synchrotron setting (P07B)	25.8	25.8	0.97

Experimental PDF data from settings D8-2 and P07B of Ni, the Ni-Ti binary alloy and the CCA investigated in this work was analyzed with respect to peak positions, peak height, and peak width in the range from $r = 0$ Å to 15 Å using software Origin Pro version 2023. Using the same software, upper and lower envelope curves were calculated for each dataset with 300 smoothing points in order to visualize the general decay of the experimental PDFs with increasing r-value.

Additionally, the experimental PDF data from all three investigated materials was fitted with software PDFgui version 1.0 [107]. Fitting was conducted over the range from 0 to 30 Å in case of Ni-Ti and CCA data, and 0 to 50 Å in case of Ni. In refinement of Ni data, the refined parameters were the lattice parameter, the isotropic ADP $\langle u^2 \rangle$, and the quadratic atomic correlation factor δ_2, as well as the instrumental parameters Q_{damp} and Q_{broad}.

In refinement of Ni-Ti binary alloy and CCA data, structural models for the different phases, i.e. γ phase, η phase, and TiC in Ni-Ti binary alloy, and γ and γ′ phase in the CCA, were taken over from Rietveld refinement. The refined values for Q_{damp}, Q_{broad}, $\langle u^2 \rangle$, and δ_2 were taken over from the Ni refinement, and only the lattice parameters and scale factors (i.e. phase fractions) of all considered phases were refined.

When comparing experimental PDF data to fitted PDF data, or to other experimental PDF data, the R-factor, as defined above in equation (3.4), was used as a measure for the goodness of fit, or the discrepancy, respectively.

4. Results

4.1. Microstructural and chemical characterization of Ni-Ti binary alloy and the CCA samples

The microstructures of selected states of Ni-Ti binary alloy (states Q and FC) and the CCA (states Q, 300 and QA) are shown in SEM images in Figure 4 and Figure 5, respectively. Grain size analysis of SEM images revealed linear intercept grain sizes of 12.24 μm ± 5 % and 12.70 μm ± 5 % for the Ni-Ti Q and FC states, respectively. Grain size was significantly higher in the CCA states Q and QA, where values of 23.18 μm ± 5 % and 15.99 μm ± 10 % were found, respectively.

In Figure 4a-c, the microstructure of Ni-Ti SA 1200-Q is shown to consist of equiaxed grains, with circular and vermicular black phases segregated at the former grain boundaries of powder particles, which were identified from EDX spectroscopy to be largely TiC and TiN (marked by cyan-colored arrows in Figure 4b, c, e and f). In the Ni-Ti SA FC state, shown in Figure 4d-f, grain size and the appearance of segregated carbides and nitrides are similar to the Q state. However, in Figure 4f, also cuboid-shaped precipitates of the η phase phase with sizes below approximately 100 nm can be identified as darker grey particles dispersed in the lighter grey FCC γ matrix (marked by pink arrows in Figure 4f).

The microstructure of CCA SA 1050-Q state is shown in Figure 5a to consist of equiaxed grains of the FCC γ matrix phase. SEM revealed no secondary phases in this state and neither the CCA state 30. On the contrary, in both CCA states 300 and QA depicted in Figure 5b-e, spherical precipitates of ordered γ′ phase with sizes of approximately 10 to 20 nm (bright particles marked by red arrows) were found to be dispersed homogeneously in the γ matrix. Furthermore, in the grain boundary regions of the QA state shown in Figure 5d, elliptical γ′ precipitates with lengths of several 100 nm and widths of approximately 50 to 100 nm could be found (also marked by red arrows). This shape of γ′ phase results from discontinuous precipitation [160].

The volume fraction of γ′ phase in the CCA SA 1050-300 state was estimated from several SEM images to be 18.2 ± 3.3 vol.%. In the QA state, a higher γ′ phase fraction of 31.8 ± 4.8 vol.% was estimate.

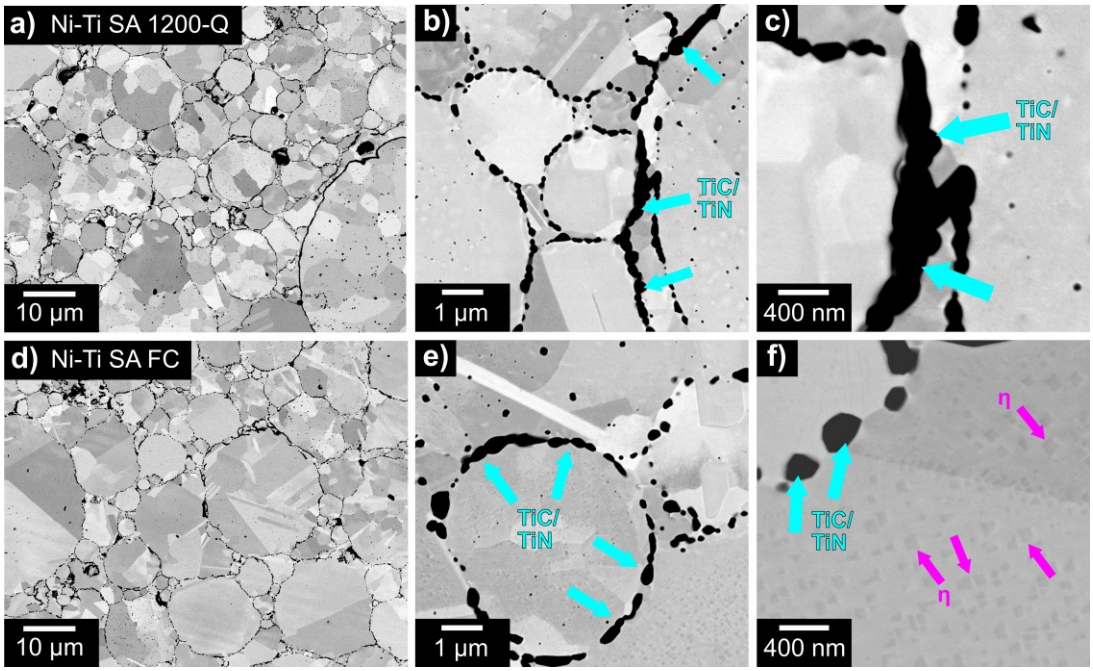

Figure 4: SEM images of Ni-Ti states SA 1200-Q (a, b, c) and SA FC (d, e, f) show micrometer-sized equiaxed grains. In both states, vermicular TiC and TiN phases (cyan) have segregated to former powder particle boundaries. In the FC state, cuboid-shaped η particles (pink) with sizes below 100 nm were identified.

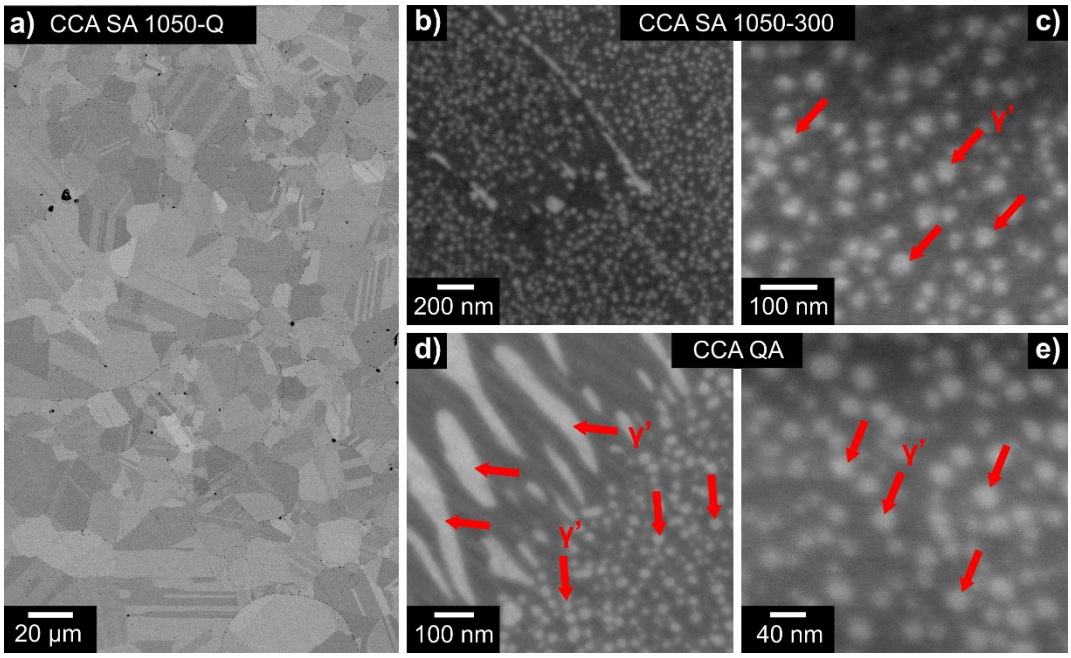

Figure 5: SEM images of the CCA states SA 1050-Q (a), SA 1050-300 (b, c), and QA (d, e) show micrometer-sized equiaxed grains. No secondary phases were identified in the Q state. In the 300 and QA states, spherical and elliptical γ' precipitates (red) with sizes between 10 and 20 nm were identified.

4.2. Methodological aspects of laboratory and synchrotron XTS experiments

4.2.1. Particle statistics in laboratory setting D8-2

The oscillation of samples during the XTS experiments has a significant effect on the irradiated sample volume and hence the particle statistics. This is shown in Figure 6, where the calculated irradiated sample volume is plotted as a function of the scattering angle 2θ with (blue curve) and without (red curve) sample oscillation with an amplitude of 4 mm as in the laboratory setting.

In the case of static sample (red), the dependence of the footprint and the penetration depth on 2θ cancel out exactly, giving constant irradiated volume of $1.66 \cdot 10^7$ μm³. When the sample is oscillated as specified instead, the irradiated sample volume increases from $1.66 \cdot 10^7$ μm³ for $2\theta = 0$ ° to $2.33 \cdot 10^8$ μm³ for $2\theta = 155$ °, i.e. an increase of more than one order of magnitude.

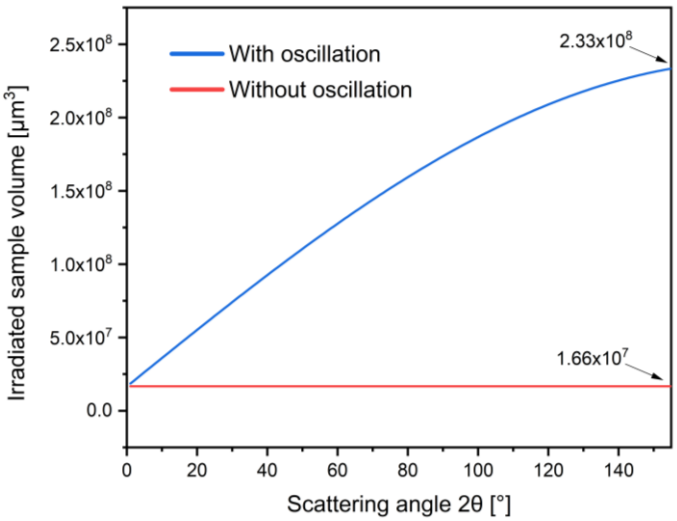

Figure 6: Estimated irradiated sample volume of solid samples in laboratory XTS measurements as a function of scattering angle 2θ with and without sample oscillation

The irradiated volume was then divided by the cubed mean grain sizes of the maximally quenched (Q) states of Ni-Ti binary alloy and CCA determined from SEM images to obtain the mean number of irradiated grains in the Ni-Ti and the CCA samples. In the Ni-Ti SA 1200-Q state, the mean grain size was 12.24 μm, hence the

number of irradiated grains was estimated as 9,000 without oscillation, and up to 125,000 at 2θ = 155 ° with oscillation, which is almost 13 times as high.

4.2.2. Analysis and comparison of two-dimensional XTS data from laboratory and synchrotron setting

Preliminary to analyzing and comparing integrated scattering data, the two-dimensional detector frames from laboratory setting D8-2 and synchrotron setting P07B shall be investigated.

In Figure 7, recorded sections of the (111) and (200) Debye-Scherrer rings at scattering angles 2θ = 20 ° and 23 °, respectively, from laboratory measurements are shown for three selected samples, i.e. Ni powder (Figure 7a), Ni-Ti SA 1200-100 (Figure 7b), and CCA SA 1050-30 (Figure 7c). The directions of the scattering angle 2θ and the azimuthal angle φ are marked with arrows in the legend graph. It can be seen from Figure 7 that the diffraction rings become broader with increasing azimuthal angle φ in all measurements. Image analysis was used to determine the full width of the (111) diffraction ring, i.e. FWHM(2θ,φ), in the center, i.e. at φ = 0 °, and at the edge of the detector frame. For the measurement of Ni, FWHM(2θ,φ) increased from 0.29 ° at φ = 0 ° to 0.77 ° at φ = 32 ° (shown by measure bars in Figure 7a). Other laboratory measurements produced similar values. However, while the rings in the measurement of Ni powder appear uniform in brightness, this is not the case for the solid samples from Ni-Ti binary alloy and the CCA (Figure 7e and f). For these samples, the rings are much rather riddled with many secluded bright spots, i.e. they show a distinct ‘spotiness’.

In line with this, Figure 8 compares the scattering intensity of diffraction peak (200) as a function of the azimuthal angle φ from laboratory measurements of Ni (red) and Ni-Ti SA 1200-100 (blue). It can be seen that the variation of the azimuthal intensity distribution is higher for the Ni-Ti binary alloy sample compared to Ni powder, and that there are several prominent peaks in the intensity distribution for the Ni-Ti sample (marked with arrows). The standard deviation of the (200) intensity distribution in the measurement of Ni is 17 counts, whereas in the measurement of Ni-Ti SA 1200-100 it is 24 counts.

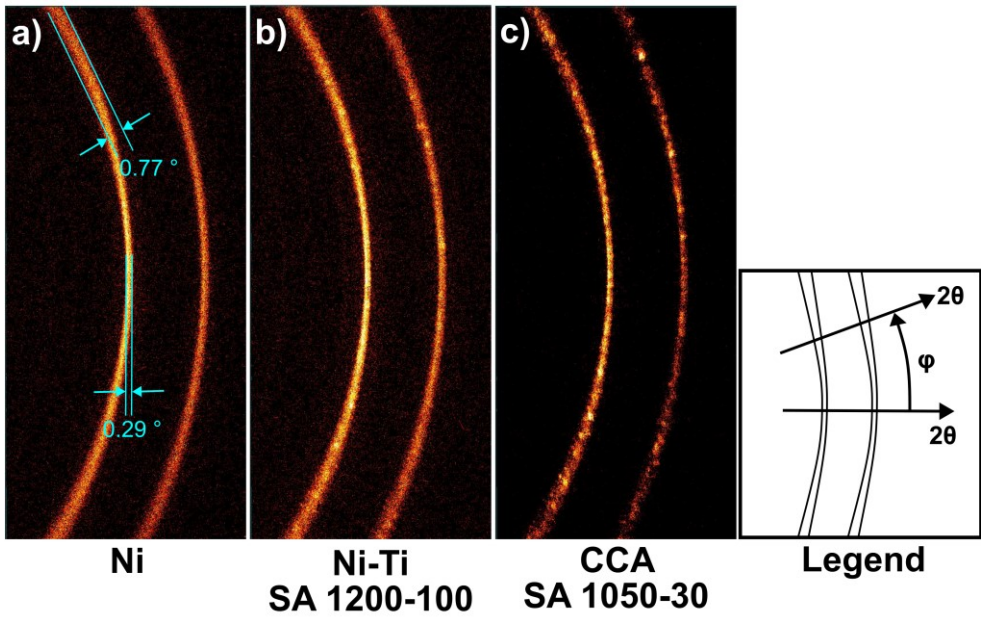

Figure 7: Recorded sections of (111) and (200) diffraction rings in laboratory setting D8-2 for (a) Ni, (b) Ni-Ti SA 1200-100, and (c) CCA SA 1050-30. Ring width increases with azimuthal angle φ from center to edge of the frames (measure bars in cyan in (a)). Diffraction rings of Ni-Ti and the CCA sample show distinct 'spotiness' compared to Ni.

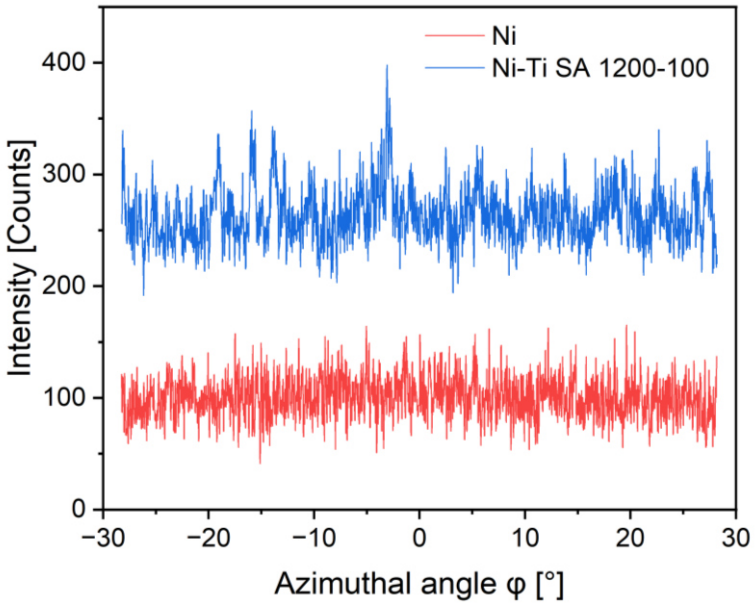

Figure 8: Intensity of (200) diffraction ring as function of azimuthal angle φ for Ni (blue) and Ni-Ti SA 1200-100 (red). Date from the Ni-Ti sample shows larger variation and visible spikes compared to data from Ni.

4.3. Analysis of XTS data from Ni powder

4.3.1. Comparison of XTS data from Ni powder generated with laboratory and synchrotron settings

Scattered intensity data from Ni powder as a function of Q, i.e. $I(Q)$, measured with the three experimental settings used in the present work, i.e. the two laboratory settings D8-1 and D8-2, as well as the synchrotron setting P07B, is depicted in Figure 9. The square root of the relative intensity (relative to intensity of (111) peak) is plotted as a solid line for D8-1 (black), D8-2 (red), and P07B (green), respectively. The full range of $I(Q)$ data is shown in Figure 9a, with selected subranges of the full data depicted in Figure 9b-e for better visual comparison. In Figure 9c, the position of diffraction peaks is marked by vertical lines.

The higher value of Q_{max} achieved with the synchrotron setting (25.8 $Å^{-1}$) compared to the laboratory settings (16.9 $Å^{-1}$) can easily be inferred from Figure 9a and b. On the other hand, the synchrotron data shows lower instrumental resolution in reciprocal space compared to the laboratory data. This is evident in Figure 9c and d, which show broader diffraction peaks for setting P07B compared to settings D8-2 and D8-1 both in the low- and high-Q region, respectively. Further illustrating this, the width parameters σ in units of Q, i.e. $Å^{-1}$, extracted from Pseudo-Voigt fits of the (111), (331), and (533) peaks positioned at approximately $Q = 3.1$ $Å^{-1}$, 7.8 $Å^{-1}$, and 11.7 $Å^{-1}$, respectively, are displayed in Table 7 for all three experimental settings. As can be seen, setting D8-1 produced the sharpest Bragg peaks, closely followed by setting D8-2. Setting P07B, however, generated much broader peaks, where the ratio of σ-values from setting P07B to D8-1 varies between 5.22:1 for the (111) peak and 7.57:1 for the (533) peak.

Data from both laboratory settings shows visible diffraction peak splitting (see Figure 9b, d and e) as a result of Kα_1 and Kα_2 components in the employed Mo radiation. In the synchrotron data in Figure 9c, on the other hand, harmonic diffraction peaks of the (111) and (200) peak at approximately $Q = 1.5$ $Å^{-1}$ are visible.

Comparison of the data in the Q-range below 2.5 $Å^{-1}$, shown in Figure 9e, reveals different background intensity between the three settings. Setting D8-2 brought the highest increase in background intensity for Q-values below 2.5 $Å^{-1}$ compared to

higher Q-values, while D8-1 produced lower change, and data from P07B shows lowest intensity in this range.

In Figure 10, the relative peak heights of diffraction peaks (relative to (111) peak) extracted from Pseudo-Voigt fits of the $I(Q)$ data measured with settings D8-1 (black squares), D8-2 (red circles), and P07B (green triangles) are compared. It can be seen that the relative peak heights obtained with settings D8-1 are in general lower compared to setting D8-2, with setting P07B producing intermediate values. For example, the relative height of the (200) peak varies between 42.34 % and 47.39 % (ratio of 1.12:1) for setting D8-1 and D8-2, respectively, while for the (311) peak the variation is between 23.35 % and 30.79 % (ratio of 1.32:1), and for the (600) peak between 1.16 % and 1.93 % (1.66:1).

The signal-to-noise ratio is satisfactory in data from both settings D8-1 and D8-2, with estimated values above 10 (i.e. signal is 10 times as high as noise), also in the high-Q region above 10 $Å^{-1}$. An indication of this can be seen in Figure 9d and e. Apart from this, the instrumental Q-resolution, $\Delta Q/Q$, was in the order of 0.01 % for both laboratory settings D8-1 and D8-2, compared to 0.1 % for the synchrotron setting P07B.

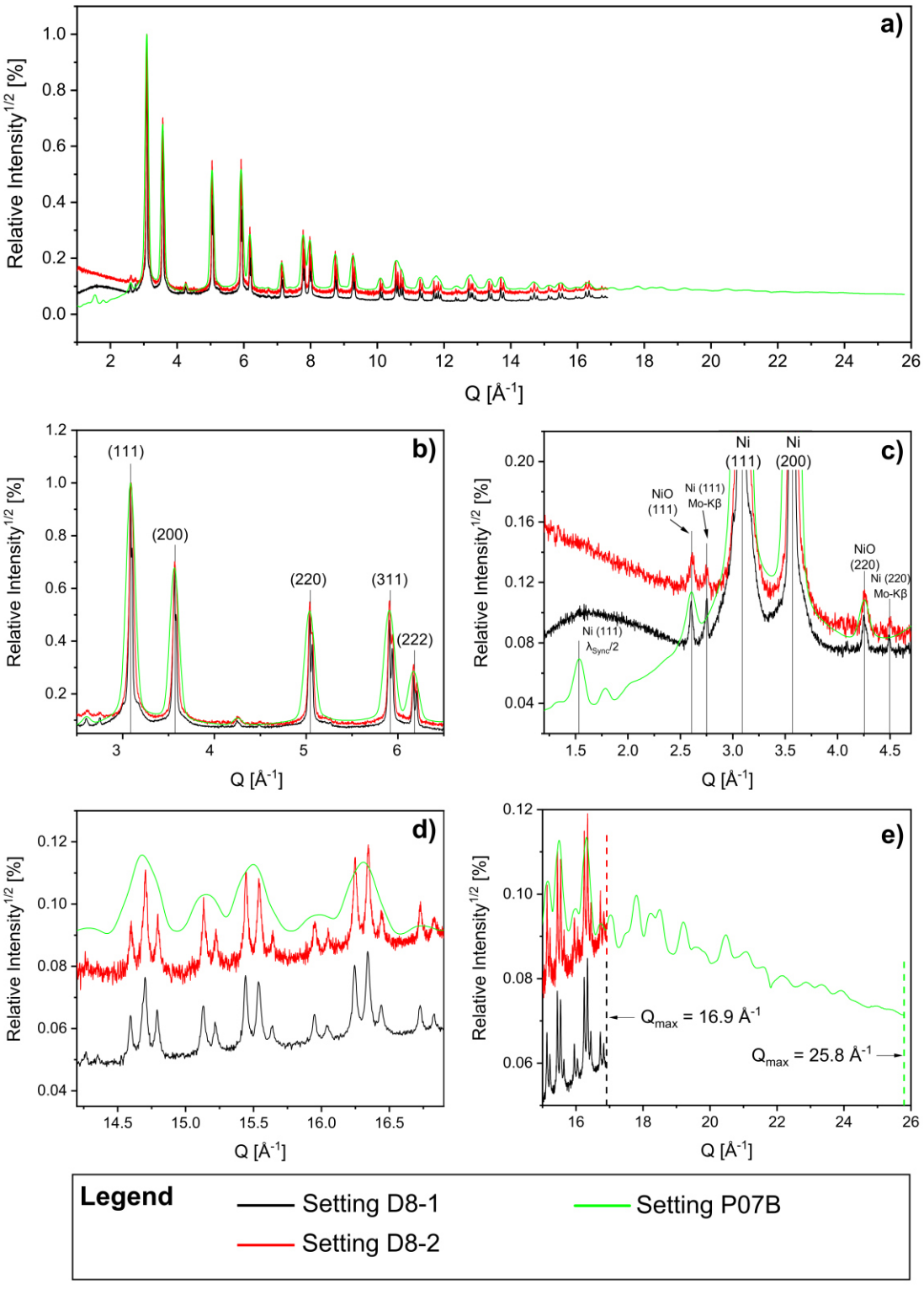

Figure 9: Scattered intensity data from Ni powder as a function of Q collected with laboratory settings D8-1 (black), and D8-2 (red), and synchrotron setting P07B (green). Full range of data is shown in (a), with subranges plotted in (b)-(e). The higher Q_{max} (25.8 Å^{-1}) but lower instrumental Q-resolution achieved with setting P07B compared to the laboratory settings (16.9 Å^{-1}) can be seen.

Table 7: Values of width parameter σ extracted from Pseudo-Voigt fits of diffraction peaks (111), (331), and (533) measured with the three different settings D8-1, D8-2, and P07B. While setting D8-1 produced the sharpest Bragg peaks before D8-2, setting P07B generated much broader peaks than the laboratory settings, indicating poorer reciprocal-space resolution.

Experimental setting	Width parameter σ from Pseudo-Voigt fits of diffraction peaks [Å^{-1}]		
	(111)	(331)	(533)
Laboratory settings			
D8-1	0.00846	0.00933	0.01097
D8-2	0.0164	0.01226	0.01257
Synchrotron setting			
P07B	0.04415	0.06248	0.08304

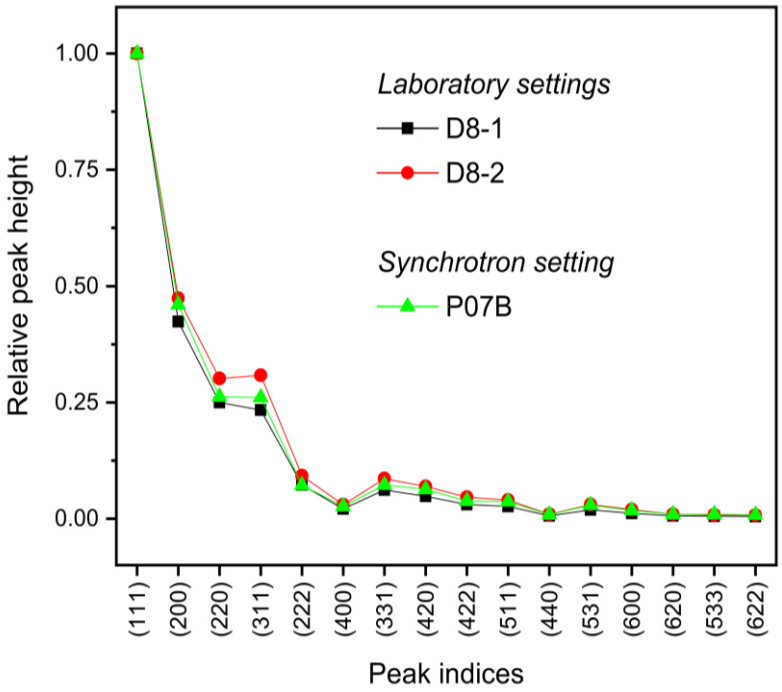

Figure 10: Relative peak height of diffraction peaks (relative to (111) peak) from settings D8-1 (black squares), D8-2 (red circles), and P07B (green triangles). Peak heights were extracted from Pseudo-Voigt fits of measured data. Considerable differences are apparent between the settings.

4.3.2. Rietveld refinement of XTS data from Ni powder

Rietveld refinement of measured intensity data from Ni powder was performed for all three experimental settings. Calculated (red solid line) and measured intensity data (blue open circles) as a function of scattering angle 2θ is plotted in Figure 11. For all three experimental settings, the difference (green solid line) is plotted with offset.

The best fit was obtained for setting P07B with an *R*-factor of 2.67 %. The fitting results for both laboratory settings are worse, however the discrepancy between calculated and measured data in the full fitting range is still better for setting D8-2 ($R = 6.39$ %) than for setting D8-1 ($R = 11.11$ %). The largest difference between calculated and measured data for setting D8-1 occurs for the (111) and (200) diffraction peaks, which is improved for setting D8-2.

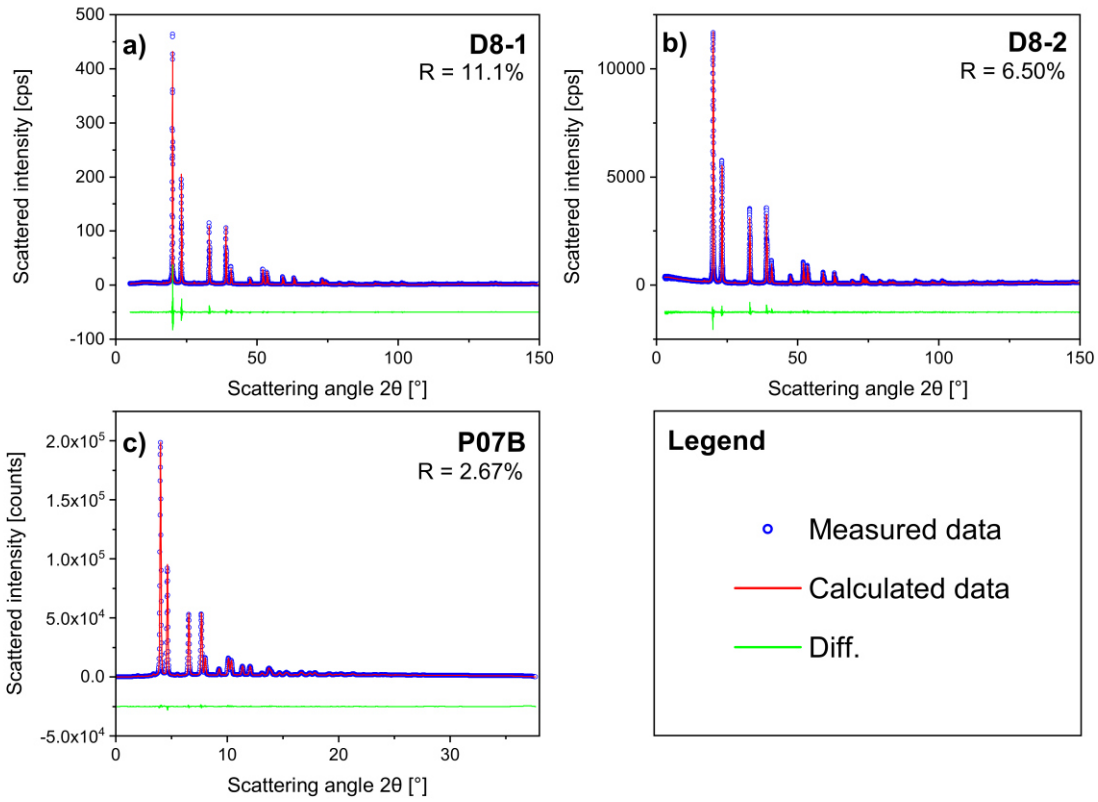

Figure 11: Calculated data (red solid line) from Rietveld refinement of measured intensity data (blue open circles) from Ni powder as a function of scattering angle 2θ obtained with settings (a) D8-1, (b) D8-2, and (c) P07B. Difference (green solid line) plotted with offset. Fit for setting P07B is excellent. Fit of first Bragg peaks is slightly better for setting D8-2 than D8-1.

While the refined Caglioti parameters *U* and *V* for the synchrotron setting P07B are in the same order of magnitude, albeit even slightly lower, compared to the laboratory settings D8-1 and D8-2, the third parameter *W* is significantly larger by one order of magnitude. The refined Caglioti parameters for Ni data, as listed in Table 8 together with the achieved *R*-factors, were then held constant for Rietveld analysis of Ni-Ti and the CCA states.

Table 8: Results from Rietveld refinement of measured intensity data from Ni powder for all three experimental settings of the present work.

Rietveld refinement parameter	Experimental setting		
	D8-1	D8-2	P07B
R [%]	11.11	6.39	2.67
Caglioti parameters [-]			
U	1.49E-2 ± 2.3E-4	4.53E-2 ± 6.2E-5	1.01E-2 ± 1.4E-4
V	-0.106 ± 1.3E-3	-0.138 ± 3.1E-4	-7.87E-2 ± 5.0E-3
W	0.140 ± 2.5E-3	0.111 ± 4.1E-4	2.36 ± 0.04
Structural parameters			
Lattice parameter [Å]	3.5221 ± 5E-5	3.5236 ± 1E-4	3.5208 ± 8E-5
Crystallite size [Å]	484.9 ± 2.0	467.9 ± 3.3	412.0 ± 2.8

4.4. Analysis of PDF data from Ni powder

4.4.1. Fitting of measured PDF data from Ni powder

The observed (blue open circles) and calculated PDFs (red solid line) of Ni from PDF refinement with software PDFgui [107] are plotted over the fitting range from 0 to 50 Å in Figure 12a, b, and c for settings D8-1, D8-2, and P07B, respectively. The difference (green solid line) is plotted in each case with a vertical offset. The refined values for the employed fit parameters, i.e. a multiplicative scale factor, Q_{damp}, Q_{broad}, a_{lat}, $\langle u^2 \rangle$, and δ_2, are given for each fit in Table 9 together with the achieved *R*-factor.

As can be seen from Figure 12, the best agreement of the calculated Ni PDFs with the observed data was obtained for synchrotron setting P07B (R = 9.26 %), with the laboratory settings ranking considerably lower (R = 16.63 % and R = 15.95 % for settings D8-1 and D8-2, respectively). The largest differences between calculated and observed data can generally be found in the low-r region from 0 to 15 Å, but for the laboratory PDFs, the difference increases again above approximately 40 Å.

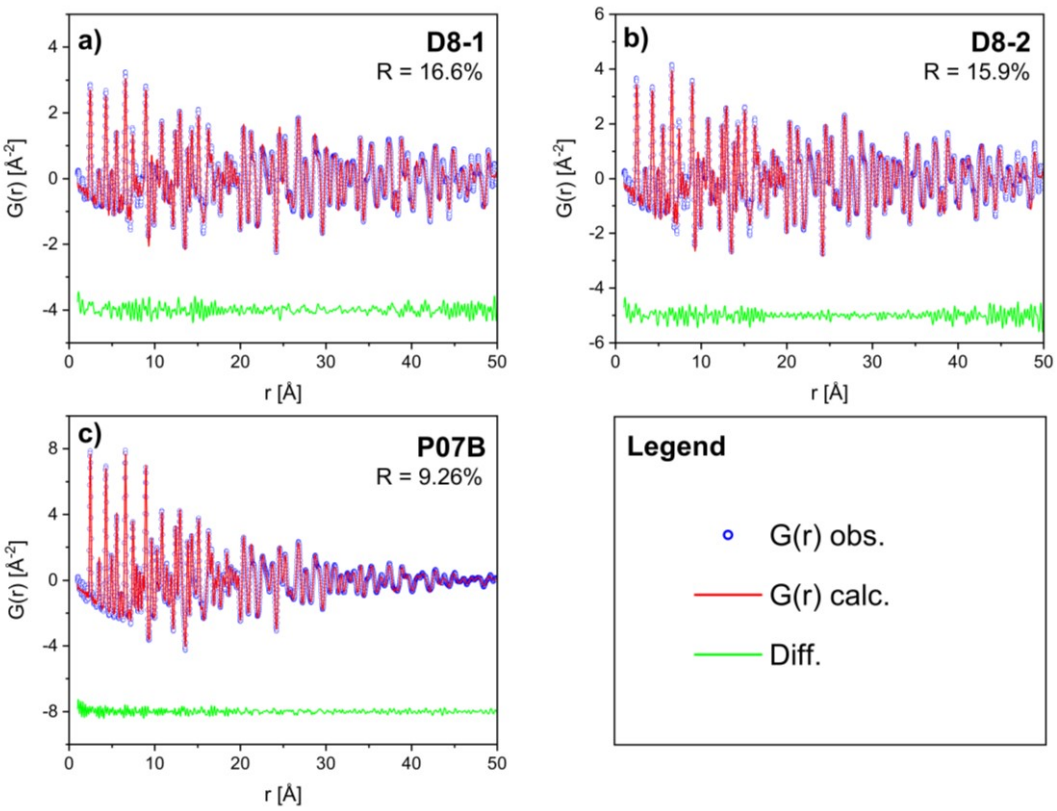

Figure 12: Calculated (red solid line) and observed Ni PDF data (blue open circles) from settings (a) D8-1, (b) D8-2, and (c) P07B in the fitting range from 0 to 50 Å. Data was fitted using software PDFgui [107]. *Difference (green solid line) is plotted with offset. Best fit was obtained for setting P07B with R = 9.26 %, with settings D8-1 and D8-2 both yielding higher, i.e. worse R-factors.*

For the laboratory settings D8-1 and D8-2, Q_{max} only made up for 47.5 % and 45.7 % of the threshold, respectively, while for the synchrotron setting P07B at least a 59.1 % fulfilment was reached. This is also reflected in the refined values of damping parameter Q_{damp} in Table 9, which are an order of magnitude lower in the laboratory settings than in the synchrotron setting.

Table 9: Refined values for employed parameters in fitting of Ni PDF data from the three experimental settings of this work

Fit parameter	Experimental setting		
	D8-1	D8-2	P07B
R [%]	16.63	15.52	9.26
Instrumental parameters			
Scale factor [-]	0.188 ± 0.01	0.234 ± 0.01	0.376 ± 0.01
Q_{damp} [Å^{-1}]	0.0081 ± 0.008	0.0136 ± 0.004	0.035 ± 0.002
Q_{broad} [Å^{-1}]	0.033 ± 0.004	0.032 ± 0.003	0.053 ± 0.004
Structural parameters			
Lattice parameter [Å]	3.5190 ± 6E-4	3.5169 ± 5E-3	3.5214 ± 5E-4
$\langle u^2 \rangle$ [Å^2]	7.1E-3 ± 0.7E-3	6.6E-3 ± 0.5E-3	4.7E-3 ± 0.3E-3
$3/\sqrt{\langle u^2 \rangle}$ [Å^{-1}]	35.6 ± 1.8	37.0 ± 1.5	43.6 ± 1.3
δ_2 [-]	1.76 ± 1.3	1.82 ± 1.0	2.27 ± 0.5

The fit parameters determining the PDF peak width, i.e. Q_{broad}, δ_2, and $\langle u^2 \rangle$, are different between the synchrotron setting and the laboratory settings. The refined value for Q_{broad} is significantly higher for the synchrotron setting than for the laboratory settings (0.053 Å^{-1} compared to 0.033 Å^{-1}). On the other hand, the refined values for $\langle u^2 \rangle$ and δ_2 are both lower for the synchrotron setting.

4.4.2. Comparison of laboratory, synchrotron and literature PDF data from Ni powder

Experimental Ni PDFs obtained with the three experimental settings in the present work, i.e. D8-1, D8-2, and P07B, were compared with literature data used as a benchmark. The reference data was collected at beamline 6-ID-D at the Advanced Photon Source (APS) by Juhas et al. (Juhas2013) [111], and at beamline ID15A at the European Synchrotron Radiation Facility (ESRF) by Zea-Garcia et al. (subsequently referred to as Zea-Garcia2019) [125], respectively. The truncation value Q_{max} used for PDF calculation in the reference works is comparable to that used for the synchrotron XTS data in the present work (26 Å^{-1} compared to 25.8 Å^{-1}).

Figure 13 shows the Ni PDF data obtained in this work in comparison to the reference data. Relative magnitude of the PDF, i.e. $G(r)$, (relative to magnitude of the Ni-Ni peak at 2.50 Å) is plotted as a function of the real-space interatomic distance r in Å in different colors for settings D8-1 (black), D8-2 (red), P07B (green), and the reference works by Juhas2013 [111] (blue), and Zea-Garcia2019 [125] (cyan). The full computed range of the PDFs from 0 to 250 Å is shown in Figure 13a, with subranges of 0-15 Å, 15-30 Å, and 30-100 Å displayed in Figure 13b-d, respectively. In Figure 13b, additionally, positions of theoretical Ni-Ni peaks of a model FCC structure are marked by vertical lines.

Focusing first on the full range of the Ni PDFs shown in Figure 13a, major differences become apparent between the laboratory and the synchrotron PDFs, both from this work and from the literature, in the damping of the peak magnitudes with increasing r-value. While in the synchrotron PDFs, the magnitudes virtually reach zero at 100 Å at the most (in case of the PDF from Zea-Garcia2019 [125]), rather already at 60 to 70 Å (PDFs from this work and Juhas2013 [111]) they still significantly differ from zero up to 200 Å in the laboratory PDFs.

The synchrotron PDF obtained at beamline P07B in the present work, and the reference PDF obtained by Juhas2013 appear to be quite similar over the range from 0 to 100 Å in Figure 13a and subsequent graphs b, c and d,. Contradicting this, the R-factors between the two datasets for the subranges 0-15 Å, 15-30 Å, and 30-100 Å are rather high at 12.47 %, 23.11 %, and 60.11 %, respectively, indicating larger differences in the details of the two PDFs.

Inspecting the low-r range from 0 to 15 Å depicted in Figure 13b, it can be seen that the measured positions of Ni-Ni peaks in this range agree well with the theoretical peak positions for an FCC structure in all compared PDFs. From comparison of the laboratory (black, red) and synchrotron data (green, blue, cyan) in this figure, it can be said that, qualitatively, the laboratory PDFs are similar to the synchrotron PDF obtained with setting P07B in the low-r range.

As can be seen, position, magnitude, and shape of peaks in this range of the PDFs are largely comparable between laboratory and synchrotron setting. Still, the R-factor between the laboratory PDF from setting D8-2 (red) and the synchrotron PDF from setting P07B (green) in the range from 0 to 15 Å is quite high with 32.39 %.

The two laboratory PDFs (black, red) are very similar in the low-*r* region, yet the difference increases with *r*. Quantifying this, the *R*-factors in the ranges 0-15 Å, 15-30 Å, 30-100 Å, and 100-300 Å are 7.86 %, 13.81 %, 36.63 %, and 70.79 %, respectively. The nature of these differences between the laboratory PDFs, which is that of a low-frequency curve in *r*, reflects the intensity differences at low *Q*-values found in the reciprocal-space data.

From the comparison of the laboratory and synchrotron PDFs, it can be seen that some theoretically expected peaks are less prominent or completely missing in the laboratory PDFs as compared to the synchrotron PDF, e.g. the [111] peak at 6.08 Å, the [211] peak at 8.62 Å, and the [220] peak at 9.92 Å. Also, peak widths at low *r*-values are larger in the laboratory PDFs as compared to the synchrotron PDF from the present work. The FWHM of the Ni-Ni peaks at 2.50 Å, 3.52 Å, and 4.31 Å, corresponding to the NN, 2NN, and 3NN Ni-Ni pairs, respectively, is given in Table 10 for the three experimental settings. It can be seen that the FWHM of the considered peaks is on average between 15.4 % (2NN) and 41.0 % (NN) higher in the laboratory PDFs compared to the synchrotron PDF. Finally, the termination ripples in the range from 0 to approximately 4 Å are more prominent in the laboratory PDFs compared to the synchrotron PDFs.

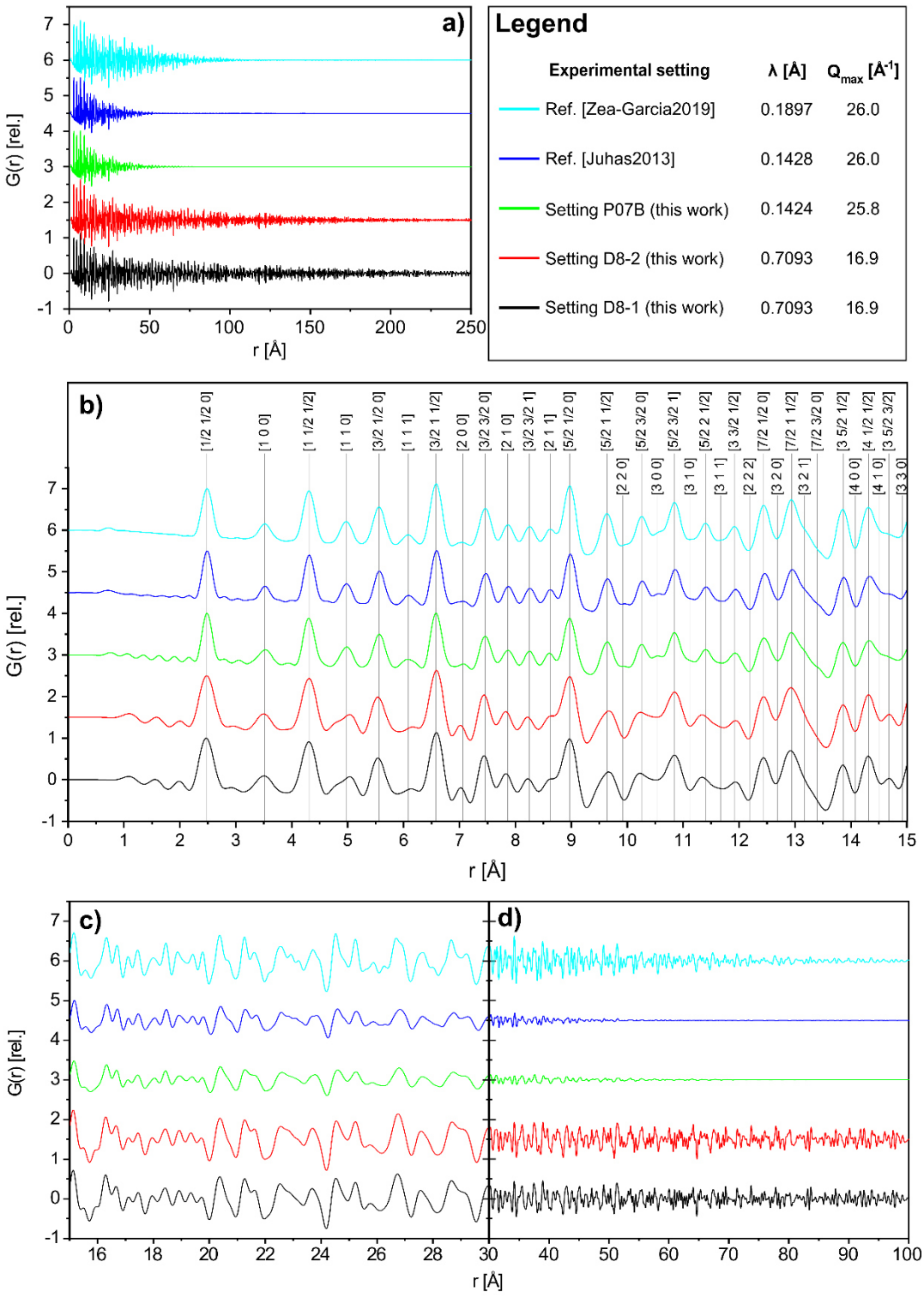

Figure 13: PDFs of Ni obtained from XTS measurements in the present work with laboratory settings D8-1 (black), D8-2 (red), and synchrotron setting P07B (green) in comparison with reference synchrotron data from literature [111] (blue), and [125] *(cyan). Full range of data plotted in (a), subranges 0-15 Å, 15-30 Å, and 30-100 Å plotted in (b)-(d). In (b), theoretical Ni-Ni peaks are marked by vertical lines. The substantially larger spatial extent of the laboratory PDFs up to 200 Å as opposed to the synchrotron PDFs (60-70 Å) can be seen.*

Table 10: FWHM of first three Ni-Ni peaks (NN, 2NN, 3NN) in the PDFs from the three experimental settings of the present work

Experimental setting	FWHM of Ni-Ni peaks in the PDF [Å] (position)		
	NN (2.50 Å)	2NN (3.52 Å)	3NN (4.31 Å)
D8-1	0.30352	0.29072	0.29307
D8-2	0.29235	0.33421	0.29693
P07B	0.20737	0.27088	0.23202

4.5. Analysis of XTS and PDF data from Ni-Ti binary alloy

4.5.1. Analysis of laboratory XTS data from Ni-Ti binary alloy samples

In Figure 14, the scattering patterns of the Ni-Ti samples are shown as a function of the scattering angle 2θ. Patterns are scaled relative to the (111) peak and are plotted with offset. Line colors gradually change from green for the maximally quenched Ni-Ti state (Q) to red-orange for the Ni-Ti state with $t_{8/5}$ = 300 s, and red for the Ni-Ti SA FC state. Full angular 2θ range of the data is shown in Figure 14a, with subranges depicted in Figure 14b-d. Visible Bragg peaks of all identified phases from Rietveld quantitative phase analysis are marked by vertical lines, with each phase ascribed its own color (grey, cyan, or magenta).

The scattering patterns of all considered Ni-Ti states show the regular FCC peaks reflecting the basic FCC crystal structure of the matrix in the Ni-Ti binary alloy. From comparison of the high-2θ region of the data in Figure 14d, it can be seen that the Bragg peaks tend to become broader with increasing cooling time. For example, the FWHM of the (620) peak at a scattering angle $2\theta \cong 78$ ° increases from 0.57 ° for the Q state to 0.75 ° for the 300 state, and 0.84 ° for the FC state.

Apart from this, some considerable systematic differences in relative peak intensities were found in the laboratory Ni-Ti data. This can for example be seen in Figure 14b, where there is a drastic drop in relative peak height of the (200), (220), (311), and (222) peaks for the Ni-Ti SA 1200-100 state (orange) compared to the other states. For example, compared to the Q state, the relative peak height of the (200) peak at a scattering angle $2\theta \cong 23$ ° decreases from 47.4 % to 44.3 % in the 100 state, and that of

the (222) peak decreases from 9.8 % to 7.1 %. In the 300 and the FC state, the relative peak intensities in the 300 and the FC state appear to be generally lower than in other states. For the 300 state, the relative difference in relative peak height increases from 2.3 % for the (200) peak at $2\theta \cong 23$ ° to 42.2 % for the (622) peak $2\theta \cong 83$ ° compared to the Q state. Similarly, for the FC state, there is a comparable increase from 9.0 % for the (200) peak to 46.6 % for the (622) peak.

In Rietveld refinement of the laboratory Ni-Ti data, the refined lattice parameter for the FCC γ matrix phase was found to decrease from 3.5670 ± 3E-5 Å for the Q state to 3.5648 ± 4E-5 Å for the 300 state, and 3.5616 ± 4E-5 Å for the FC state. On the contrary, in refinement of synchrotron data, the γ lattice parameter first increased from 3.5590 ± 3E-4 Å in the Q state to 3.5616 ± 3E-4 Å in the 300 state, before dropping to 3.5547 ± 3E-4 Å in the FC state. Apart from the matrix phase, TiC and η phase were identified from Rietveld analysis of the laboratory and synchrotron Ni-Ti XTS data, in compliance with the results from SEM and EDX analysis (see section 4.1). In Figure 14c, the visible peaks in the laboratory XTS data ascribed to each secondary phase are marked by vertical lines and arrows in pink and cyan for TiC and η phase, respectively. While TiC was identified in all Ni-Ti states with similar phase fractions ranging between 3.59 ± 8E-4 at.% and 4.11 ± 9E-4 at.% (weighted mean value: 3.81 at.%), the η phase was only identified from Rietveld analysis in the FC state. Here, a refined η phase fraction of 6.65 ± 5E-4 at.% was found.

4.5.2. Comparison of laboratory PDF data from Ni-Ti binary alloy samples

Laboratory PDF data from samples of the Ni-Ti series and the FC state obtained with setting D8-2 are shown in Figure 15. The PDFs are normalized with respect to the [½ ½ 0] peak at 2.52 Å. Full range of the PDFs from 0 to 300 Å is plotted in Figure 15a, and subranges of 0-15 Å, 15-30 Å, and 30-100 Å in Figure 15b, c and d, respectively. Line color of the PDF curves changes gradually with material state from green (Q) to red-orange (300), and finally red (FC). In Figure 15b, the position and corresponding crystallographic direction of theoretical PDF peaks in the range 0-15 Å is marked by vertical lines. Differences of the PDFs with respect to the PDF of the Q state are plotted as superimposed curves in lighter colors.

From comparison of the low-*r* region in Figure 15b, it can be seen that the positions and shapes of the peaks in the PDF are similar between the considered Ni-Ti alloys due to the average FCC structure of the Ni-Ti binary alloy. However, with increasing *r*-value, as depicted in Figure 15c and d, differences with respect to the Q state systematically increase with cooling time up to the FC state, where they are largest. This can be attributed to an increasing shifting of PDF peaks towards smaller *r*-values with cooling time.

4.5.3. Fitting of PDF data from Ni-Ti binary alloy samples

In fitting of laboratory PDF data, fit quality was generally good with weighted profile *R*-factors between 13.1 % and 15.0 %. A significantly worse result was obtained solely for the Ni-Ti SA 1200-100 state with *R* = 20.7 %. The refined phase fraction of TiC was negligibly small for all Ni-Ti states, but with a high degree of uncertainty (weighted mean value: 0.03 ± 3.75 at.%). The refined phase fraction of η phase significantly differed from zero in the Ni-Ti states Q to 300, with a weighted mean value of 4.25 ± 1.12 at.%, before rising to 11.63 ± 2.50 at.% in the FC state. This is in contrast to the results from SEM and EDX analysis (see section 4.1) as well as Rietveld refinement (see section 4.5.1), where no indication of η phase was found in the quenched Ni-Ti states, except for the FC state. Hence, the elevated η phase fractions from PDF refinement of laboratory data must be dismissed as implausible.

In contrast to this, the refinement of synchrotron PDF data (*R* between 14.1 % for FC state and 18.9 % for Q state) yielded refined phase fractions of η phase and TiC consistent with the results from SEM and EDX as well as Rietveld analysis. In all states except the FC state, the refined η phase fraction was virtually zero (in the order of 10^{-3} %), but with high uncertainties (about 1 %), and that of TiC varied between 5.45 and 9.95 at.% (weighted mean value: 8.26 ± 1.02 at.%). In the FC state, an η phase fraction of 3.33 ± 1.7 at.% was found.

Additionally, in the refinement of laboratory data, a decrease of the refined lattice parameter of the γ matrix from 3.5634 ± 6E-4 Å in the Q state to 3.5555 ± 6E-4 Å in the FC state was found.

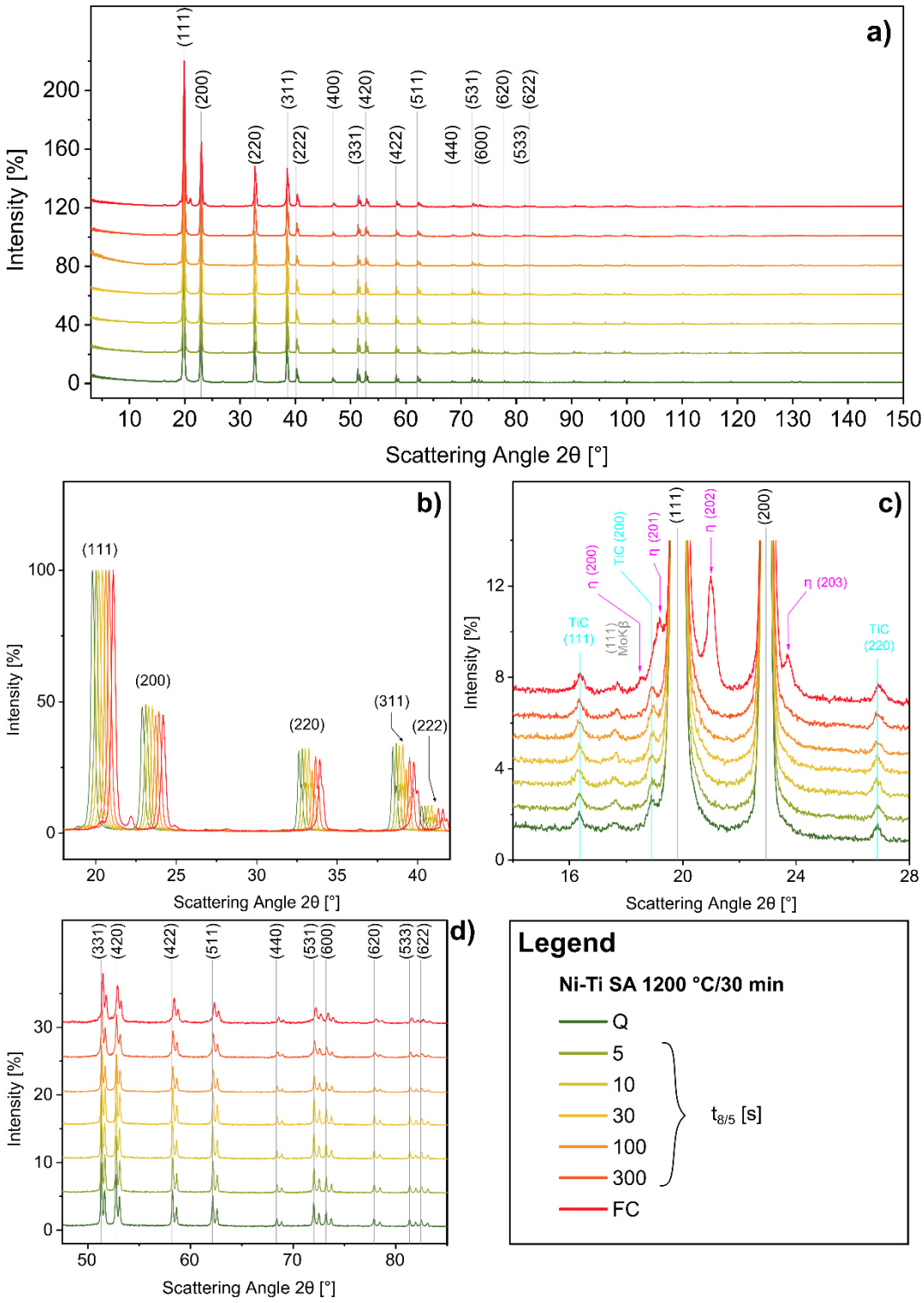

Figure 14: Scattered intensity patterns of Ni-Ti SA 1200 samples measured with laboratory setting D8-2. Full data range in (a), low- and high-2θ region in (b)-(d). Bragg peaks of all identified phases (matrix, TiC, and η phase) are marked by vertical lines and arrows. TiC peaks (pink) were identified in patterns of all Ni-Ti states, while η peaks (cyan) were identified only in the FC state. Regular Bragg peaks of the matrix become broader with cooling time from the Q state to the FC state.

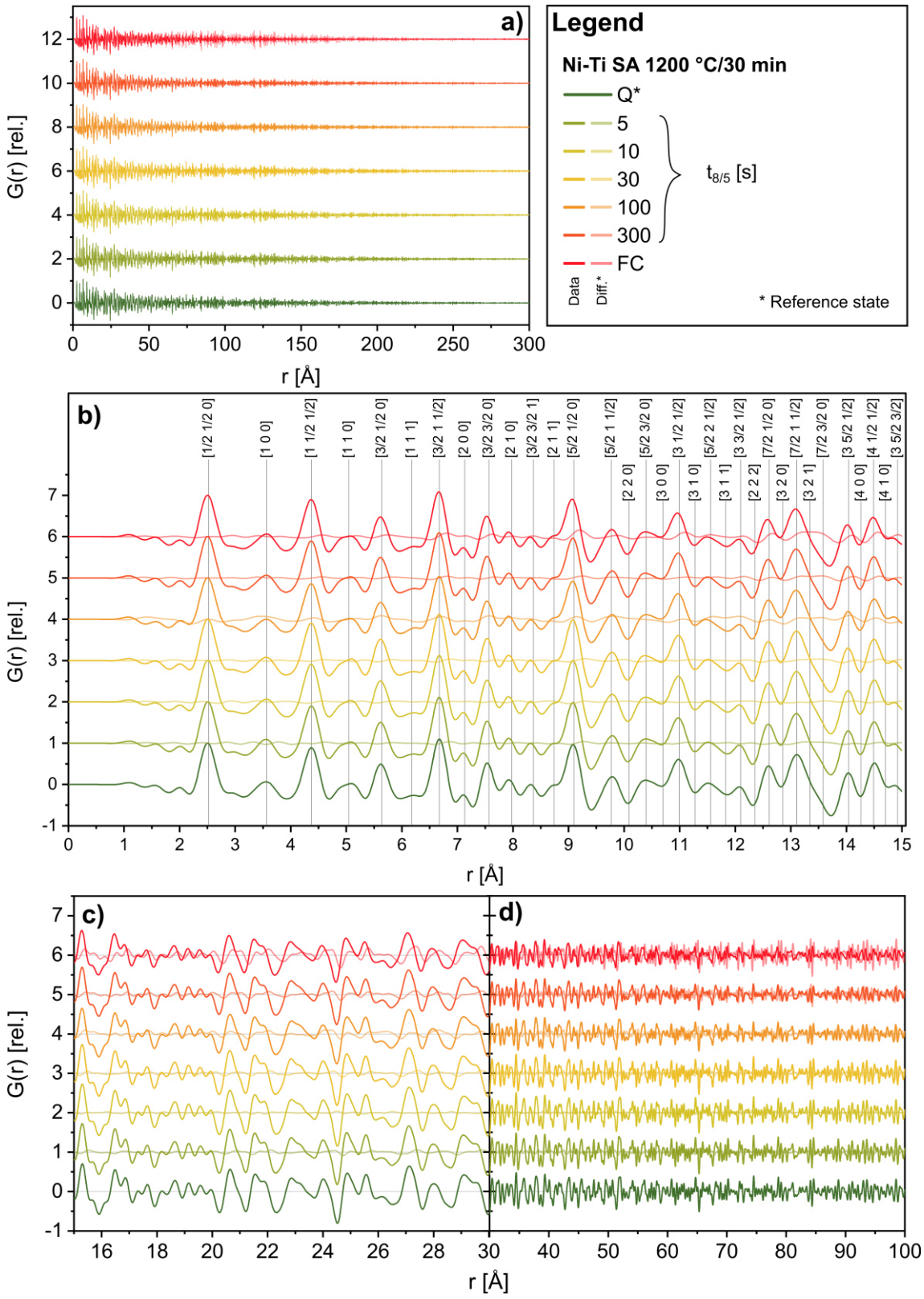

Figure 15: Laboratory PDF data from Ni-Ti SA 1200 samples obtained with setting D8-2. Full computed data (0-300 Å) in (a), subranges 0-15 Å, 15-30 Å, 30-100 Å in (b)-(d). Differences with respect to the PDF of the Q state are plotted superimposed on PDF data in lighter colors. In (b), theoretically expected PDF peaks for the matrix structure are marked by vertical lines.

4.6. Analysis of XTS and PDF data from CCA samples

4.6.1. Analysis of XTS data from CCA samples

Similar to the Ni-Ti binary alloy, peak analysis and Rietveld refinement were performed on laboratory and synchrotron XTS data (collected with settings D8-2 and P07B, respectively) from samples of the CCA series, as well as the QA reference state. In Figure 16, the laboratory scattering patterns of the considered the CCA states are displayed as a function of the scattering angle 2θ. Patterns are scaled relative to the (111) peak and are plotted with offset. Line colors gradually change from green for the maximally quenched CCA state (Q) to red-orange for the CCA SA 1050-300 state, and red for the CCA QA state. Full angular 2θ range is shown in Figure 16a, with subranges depicted in Figure 16b-d. Peaks of all identified phases are marked by vertical lines.

Again, the regular FCC Bragg peaks appear in the scattering patterns of all considered CCA states, as seen in Figure 16a. Still, as was the case for the laboratory Ni-Ti data, major irregular differences in relative peak height between the considered CCA states were revealed, especially for the peaks at scattering angles 2θ below approximately 40 °. To further illustrate this, the evolution of relative peak height of the (h00) Bragg peaks (h = 2, 4, 6) with cooling time (and aged state as reference) is shown in Figure 17. As can be seen in this figure, the relative height of the (200) peak at 22.8 ° varies between 33.36 % for the CCA QA state and 46.87 % for the state with $t_{8/5}$ = 30 s, with a considerable drop for the state with $t_{8/5}$ = 10 s. Contrary to this, in the data for the (400) and the (600) peak, a drop in peak height occurs for the state with $t_{8/5}$ = 5 s.

Besides the regular FCC peaks, superstructure peaks of FCC type with varying height and width were identified in the laboratory XTS patterns of all considered CCA states. The observed superstructure peaks were (100) at a scattering angle 2θ of 11.3 °, (110) at 16.4 °, and (210) at 25.5 °. The evolution of superstructure peaks in the CCA as a function of material state is shown in Figure 16b and c, where they are marked by vertical lines and colored text labels (magenta for (100), green for (110), cyan for (210)). Calculated Pseudo-Voigt fit curves (dashed) of the same colors are superimposed as a guide to the eye.

It can be seen in Figure 16c that the superstructure peaks become less pronounced with decreasing cooling time down to the state with maximum quenching rate (Q), as compared to the aged reference state (QA). To illustrate this, relative peak heights and FWHM of the superstructure peaks in the CCA samples were extracted from the Pseudo-Voigt fit curves. In Figure 18a, relative peak height of the superstructure peaks, i.e. (100), (110), and (210), in percent is shown as a function of material state (represented by cooling time $t_{8/5}$, with QA state as a reference). Figure 18b depicts the evolution of the fit FWHM of the superstructure peaks in degrees.

It can be seen that the superstructure peak heights correlate positively with the cooling time from the maximally quenched to the aged CCA state. Despite considerably strong variations in the FWHM evolution from quenched to aged state, still a slight trend of decreasing peak width with increasing cooling time can be postulated.

In Rietveld refinement of the synchrotron data, the average lattice parameter of the CCA γ matrix phase was found to decrease with cooling time by 0.43 % from 3.5932 ± 2E-4 Å for the Q state to 3.5778 ± 2E-4 Å for the QA state. In the refinement of laboratory data, the decrease of the lattice parameter was similar, from 3.5902 ± 3E-5 Å (Q) to 3.5820 ± 4E-5 Å (QA). At the same time, in refinement of synchrotron data, the γ' lattice parameter was found to increase with cooling time by 0.41 % from 3.5932 ± 2E-4 Å (Q) to 3.6045 ± 4E-4 Å (300), followed by a slight decrease to 3.5996 ± 2E-4 Å (QA). From laboratory data, the refined γ' lattice parameter for the Q state and QA state were 3.6002 ± 6E-3 Å and 3.5935 ± 6E-5 Å, respectively.

From the refined lattice parameters of the matrix and the coherent γ' phase, the coherency strain at the phase boundary was computed, where a steady increase of coherency strain from 0.10 ± 0.10 % for the Q state to 0.54 ± 0.01 % for the 300 state, and 0.61 ± 0.01 % for the QA state was found from the synchrotron data, and a less significant increase from laboratory data (Q – 0.28 ± 0.15 %; 300 – 0.31 ± 0.01 %; QA – 0.32 ± 0.01 %).

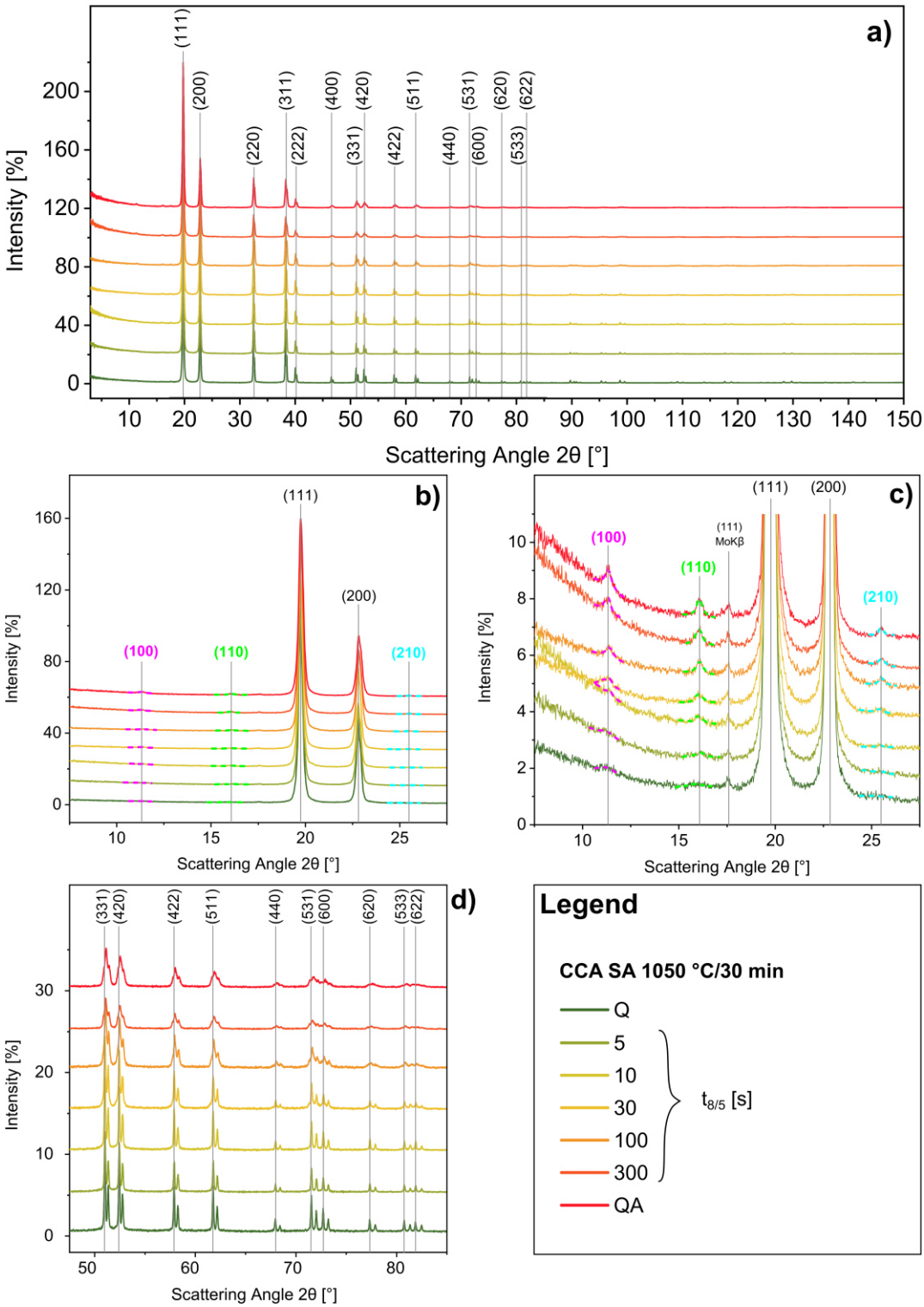

Figure 16: Scattered intensity patterns of CCA SA 1050 samples measured with laboratory setting D8-2. Full data range in (a), low- and high-2θ region in (b)-(d). Bragg peaks are marked by vertical lines. Identified superstructure peaks (100), (110), and (210) are highlighted, for which Pseudo-Voigt fit curves are superimposed on the measured data. It can be seen that regular Bragg peaks become broader with cooling time from the Q state to QA state, while superstructure peaks become sharper.

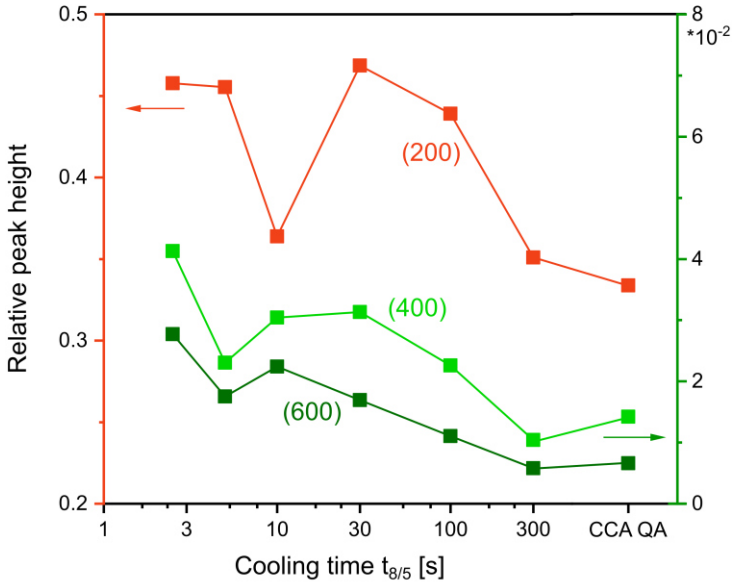

Figure 17: Evolution of relative peak height (relative to (111) peak) of (h00) Bragg peaks (h = 2, 4, 6) in laboratory XTS data from CCA SA 1050 samples as a function of cooling time. The general trend of lower peak height with increased cooling time is corrupted by irregular drops in peak height.

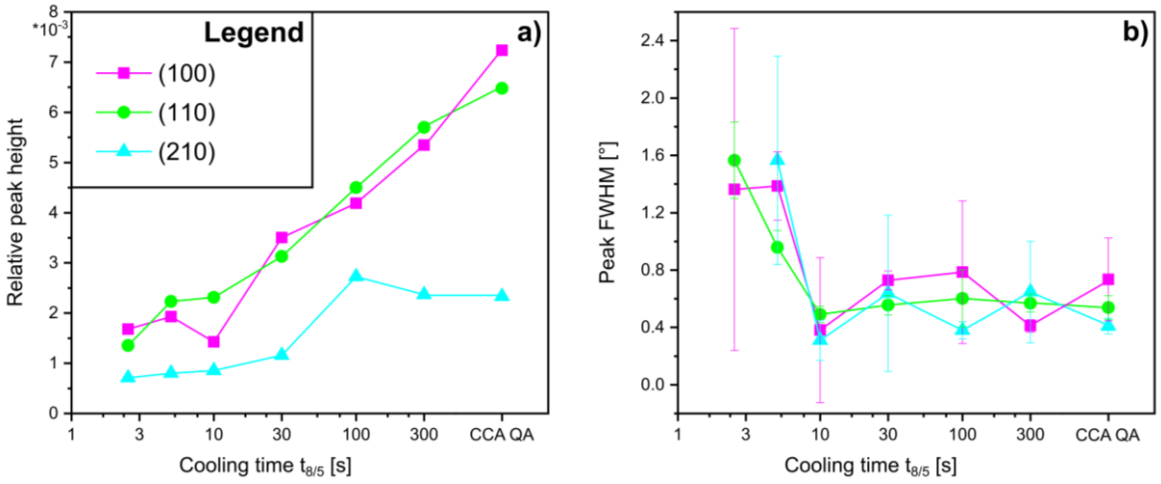

Figure 18: Evolution of superstructure peaks in CCA SA 1050 samples as a function of cooling time. (a) Relative peak height (relative to (111) peak) of superstructure peaks (100), (110), and (210), and (b) FWHM were extracted from Pseudo-Voigt fits. Uncertainties in the case of the FWHM are shown by error bars. There is a transition of the superstructure peaks from broad diffuse 'bumps' at short cooling times to sharp Bragg peaks (higher peak height, lower FWHM) at longer cooling times, and in the QA reference state.

From Rietveld refinement of the laboratory CCA data, the refined γ′ phase fraction was found to increase with cooling time from 0.76 ± 0.28 at.% for the Q state to 31.98 ± 0.74 at.% for the 300 state, and 38.04 ± 0.50 at.% for the QA state. In refinement of the synchrotron data, an increase of 4.68 ± 0.54 at.% (Q) to 29.03 ± 0.79 at.% (300), and 35.06 ± 0.62 at.% (QA) was found. At the same time, the refined crystallite size of the γ′ phase was found to increase from 109.3 ± 2.1 Å for the Q state to 336.3 ± 9.4 Å for the 300 state, and 396.8 ± 1.0 Å for the QA state in laboratory data (synchrotron: Q – 196.6 ± 1.5 Å; 300 – 380.9 ± 0.2 Å; QA – 548.3 ± 0.2 Å).

In advance, it shall be remarked here that graphical results from Rietveld refinement of laboratory and synchrotron XTS data from the CCA states will be given in Figure 27 in section 4.6.3.

4.6.2. Comparison of PDF data from the CCA samples

Laboratory PDF data from samples of the CCA series and the QA state obtained with setting D8-2 is shown in Figure 19. The PDFs are normalized with respect to the [½ ½ 0] peak at 2.53 Å. Full range of the PDFs from 0 to 300 Å is plotted in Figure 19a, and subranges of 0-15 Å, 15-30 Å, and 30-100 Å are depicted in Figure 19b, c and d, respectively. Line color of the PDF curves changes gradually with material state from green (Q) to orange (300), and red (QA). In Figure 19b, theoretical PDF peaks in the range 0-15 Å are marked by vertical lines. Differences of the PDFs with respect to the PDF of the Q state are plotted as superimposed curves in lighter colors. Complementary to the laboratory PDFs, synchrotron PDF data of the investigated CCA states, i.e. Q, 30, 300, and QA, obtained with setting P07B is plotted in Figure 20. Here, the PDFs were only computed up to 100 Å, as their magnitude reaches zero at approximately 60 Å. Again, full data range is plotted in Figure 20a, with subranges plotted in Figure 20b-d.

From comparison of the full PDF range depicted in Figure 19a and Figure 20a, as well as the higher-*r* regions (15-30 Å, and 30-100 Å) depicted in Figure 19c and d, and Figure 20c and d, respectively, it can be seen that in both laboratory and synchrotron data, the PDFs of CCA states with higher cooling time, and of the QA state are more damped than the PDFs of states with lowest cooling times.

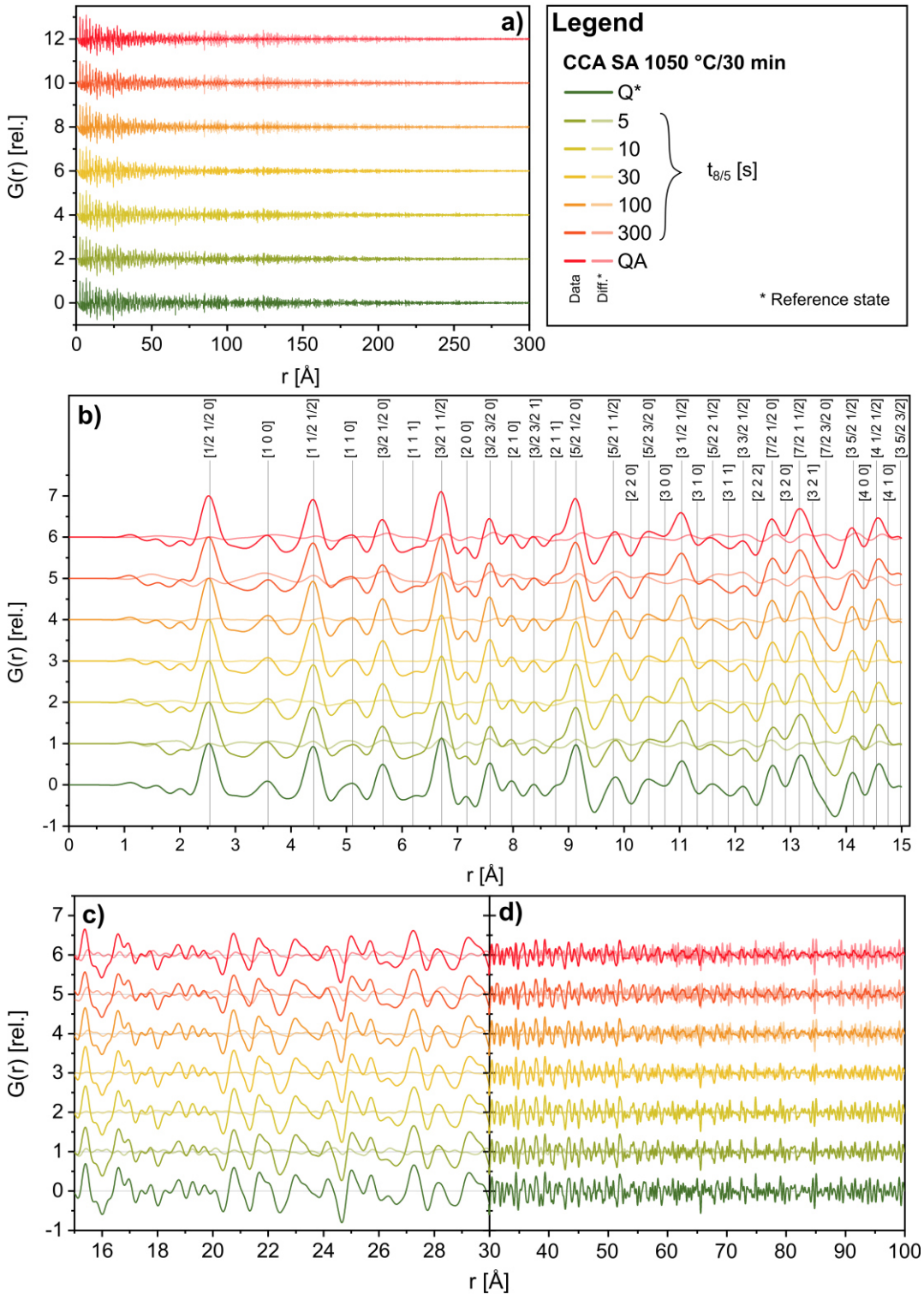

Figure 19: Laboratory PDF data from CCA SA 1050 samples obtained with setting D8-2. Full computed data (0-300 Å) in (a), subranges 0-15 Å, 15-30 Å, 30-100 Å in (b)-(d). Differences with respect to the PDF of the Q state are plotted superimposed on PDF data in lighter colors. In (b), theoretically expected PDF peaks for the matrix structure are marked by vertical lines.

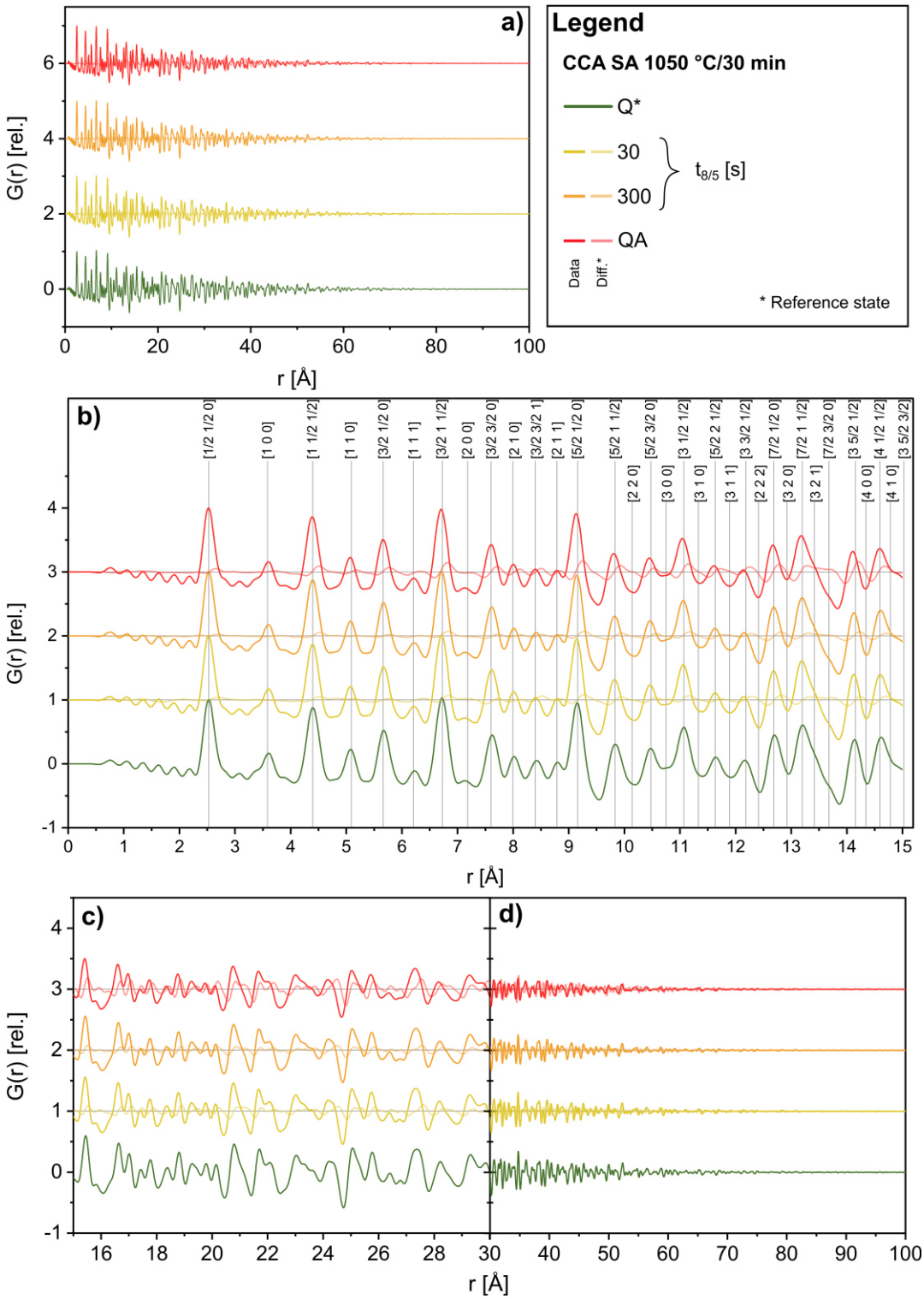

Figure 20: Synchrotron PDF data from CCA SA 1050 samples obtained at beamline P07B. Full computed data (0-100 Å) in (a), subranges 0-15 Å, 15-30 Å, 30-100 Å in (b)-(d). Differences with respect to the PDF of the quenched state (Q) are plotted superimposed on PDF data in lighter colors. In (b), theoretically expected PDF peaks for FCC structure are marked by vertical lines.

For example, in the laboratory PDF data, the magnitude of PDF oscillations in the region from 150 to 250 Å is substantially higher in the Q state (green) than in the 300 (red-orange) and the QA state (red), where the oscillations already decrease to almost zero at approximately 150 Å (see Figure 19a).

To confirm this visual impression, upper and lower envelope curves were calculated for the normalized laboratory and synchrotron PDF data of all considered CCA states and evaluated at r = 100 Å, and r = 30 Å, respectively. The upper and lower envelopes for the laboratory and synchrotron PDFs are shown in Figure 21a and b, respectively, using the same color code as above, with the PDFs themselves plotted superimposed in lighter colors.

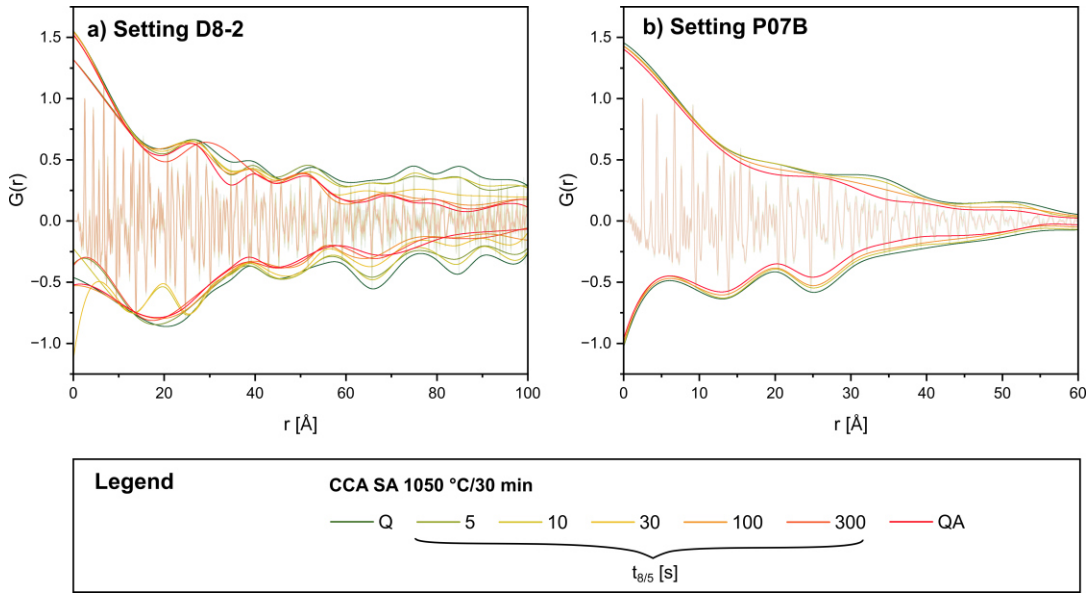

Figure 21: Calculated upper and lower envelope curves for (a) laboratory PDFs obtained with setting D8-2, and (b) synchrotron PDFs obtained with setting P07B, as a function of material state of the investigated CCA. The experimental PDFs themselves are plotted superimposed in lighter colors. It can be seen that the PDFs are damped more strongly with increasing cooling time from Q to QA state.

The upper and lower envelope values extracted from laboratory and synchrotron PDFs at r = 100 Å, and r = 30 Å, respectively, are given as a function of material state of the investigated CCA in Figure 22a and b, respectively. It can be seen that both laboratory and synchrotron PDFs of the CCA states decay more rapidly with increasing cooling time from the Q to the QA state. For example, the upper envelope value of the laboratory PDFs at r = 100 Å decreases from 0.287 normalized units in the

Q state to 0.112 normalized units in the QA state, while the absolute value of the lower envelope also decreases from 0.264 (Q) to 0.066 (QA). Similarly, the absolute upper and lower envelope value of the synchrotron PDFs at $r = 30$ Å decrease from 0.380 (Q) to 0.283 (QA), and from 0.384 (Q) to 0.285 (QA), respectively.

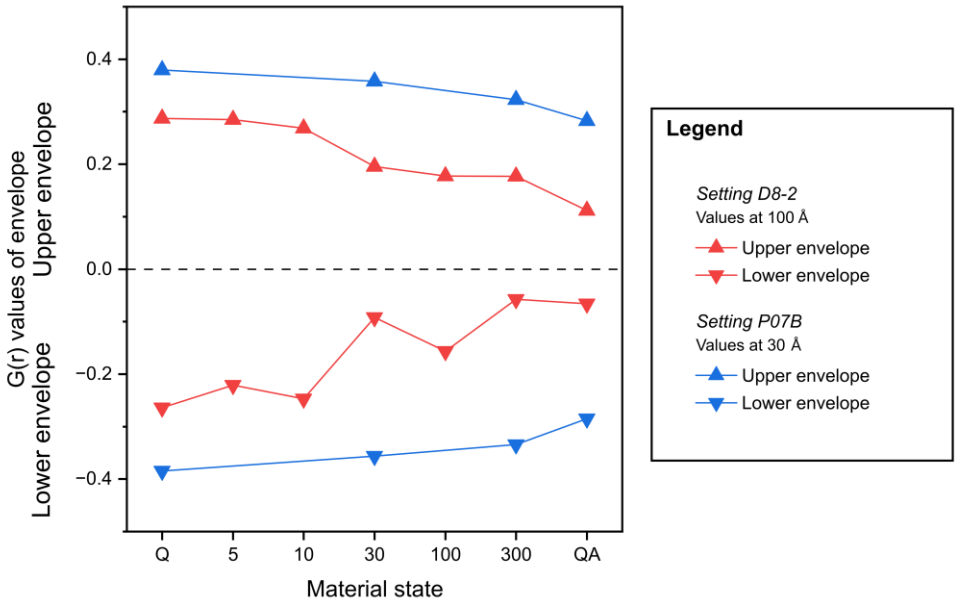

Figure 22: Values of the upper (upwards triangle) and lower (downwards triangle) envelope of the laboratory PDFs of the CCA obtained with setting D8-2 (red) and the synchrotron PDFs of the CCA obtained with setting P07B (blue), evaluated at $r = 100$ Å, and $r = 30$ Å, respectively. It can be seen that the absolute value of upper and lower envelopes decreases with increasing cooling time of the CCA from Q to QA state, indicating stronger damping of both laboratory and synchrotron PDFs with material state.

In the low-*r* region (0-15 Å) depicted in Figure 19b and Figure 20b, respectively, both laboratory and synchrotron PDFs of the considered CCA states are largely similar within each experimental setting, i.e. D8-2 or P07B. However, a more thorough analysis of selected PDF peaks revealed some differences. In the following, results are presented from analysis of the NN, 2NN, 3NN peaks, as well as the 13th and the 26th physical PDF peaks, situated at approximately $r = 9.1$ Å and $r = 13.1$ Å, and termed 'Peak 13' and 'Peak 26', respectively. A detailed view of these peaks in the laboratory and the synchrotron PDFs of the investigated CCA states is given in Figure 23a and b, respectively, where the peaks are marked by arrows.

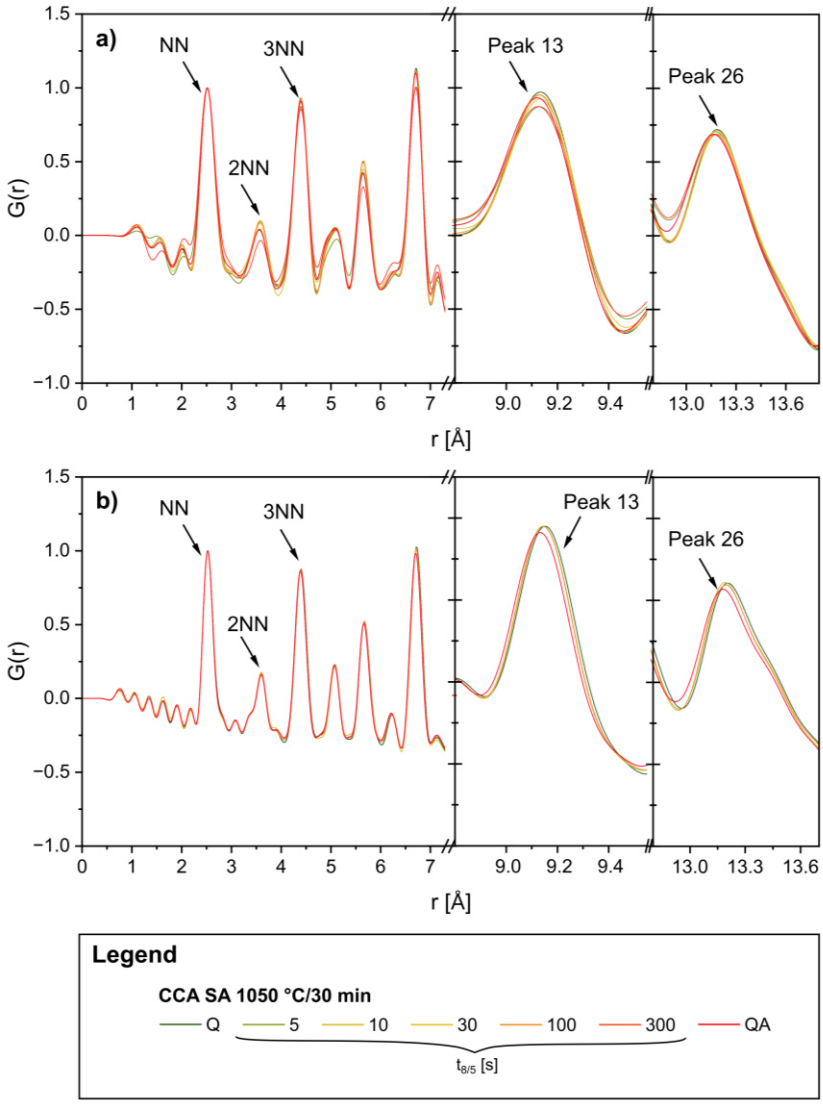

Figure 23: Detailed view of selected analyzed PDF peaks (NN, 2NN, 3NN; Peak 13 and Peak 26; marked by arrows) in (a) the laboratory PDF data, and (b) the synchrotron PDF data of the investigated CCA.

Figure 24a and c depict the relative deviation of the PDF peak height from the mean for the NN (grey squares), 2NN (red circles), and 3NN (blue triangles) peaks as a function of material state of the investigated CCA extracted from laboratory and synchrotron PDF data, respectively. It should be noted that the relative deviation in the case of the laboratory data reached absolute values of up to 30 % for the 300 state, with other values between 0 and 10 %, while for synchrotron data, the deviation reached a maximum absolute value of approximately 3 % for the 300 state, and values between 0 and 1 % in the other states. Complementary, Figure 24b and d show the PDF peak width of these peaks as a function of CCA material state for laboratory and

synchrotron setting, respectively. It can be seen that for both laboratory and synchrotron data, there is no significant correlation between PDF peak shape of the NN, 2NN and 3NN peaks with material state of the CCA, neither with regard to peak height nor with regard to peak width.

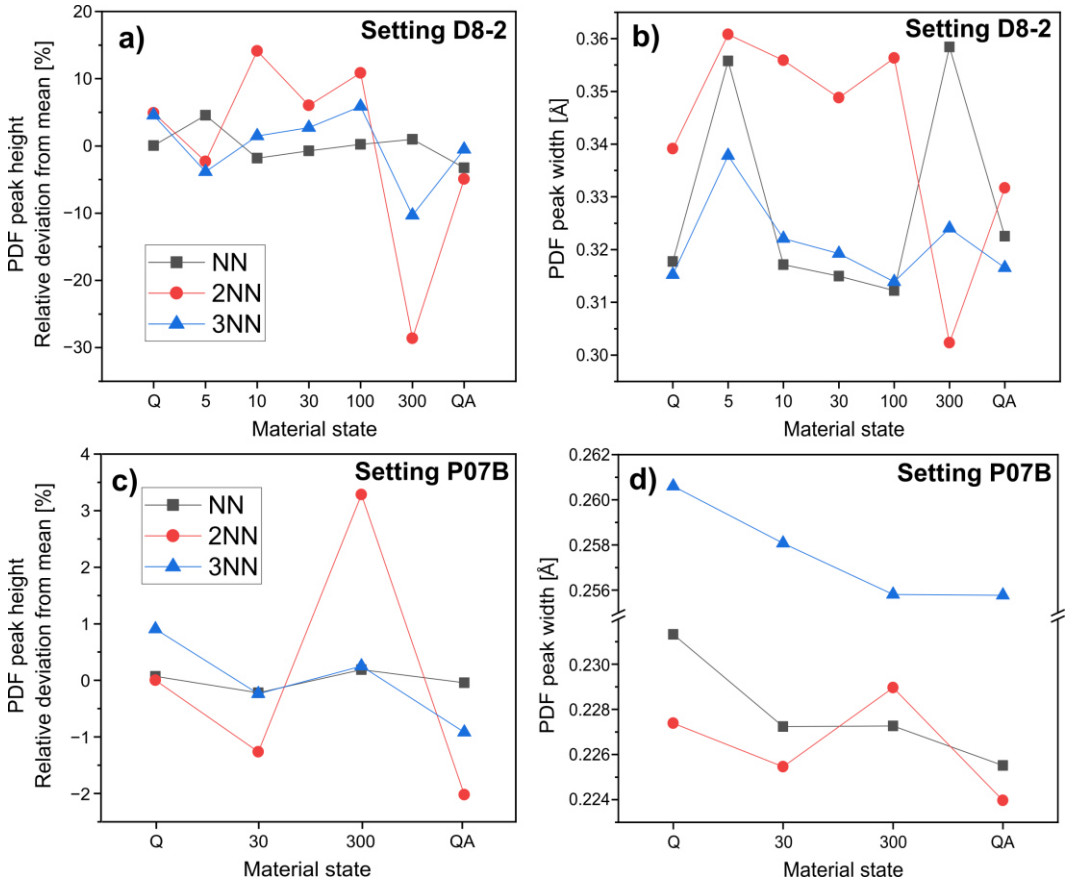

Figure 24: Dependence of (a, c) PDF peak height (relative deviation from mean), and (b, d) PDF peak width of NN (grey squares), 2NN (red circles), and 3NN (blue triangles) peaks on CCA material state in laboratory data from setting D8-2 (a, b), and synchrotron data from setting P07B (c, d). No clear correlation between PDF peak height or shape of the three peaks, and CCA material state can be seen.

However, it was found for both laboratory and synchrotron PDF data that there is a significant positional shift of PDF peaks towards lower *r*-values with increasing cooling time of the investigated CCA from the Q to the QA state. This is shown in exemplary manner by Figure Aba and b, which depict the positions of Peak 13 (red squares), and Peak 26 (blue circles) as a function of the CCA material state for setting D8-2 (filled symbols) and setting P07B (open symbols), respectively. For example, Peak 26 was found to shift in the laboratory PDFs from $r = 13.185$ Å in the Q state to

r = 13.163 Å in the QA state. Similarly, the observed shift of Peak 26 in the synchrotron PDFs was from r = 13.205 Å (Q) to r = 13.178 Å (QA).

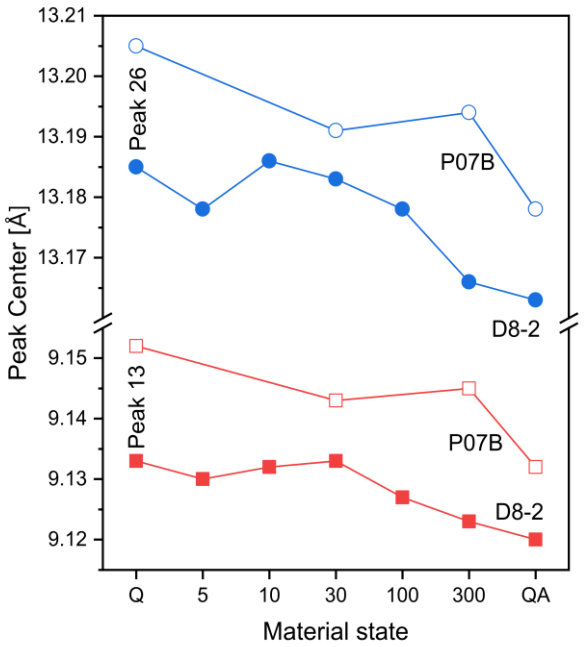

Figure 25: Evolution of peak position of Peak 13 (red squares), and Peak 26 (blue circles) with CCA material state for laboratory data from setting D8-2 (filled symbols), and synchrotron data from setting P07B (open symbols). It can be seen that there is a shift of the PDF peaks towards lower r-values with increasing cooling time from Q to QA state.

4.6.3. Fitting of laboratory and synchrotron PDF data from CCA samples

Graphical results of the fitting of PDF data from the CCA samples are shown in Figure 26. Observed (blue open circles) and calculated (red solid line) data from CCA states Q, 30, 300 and QA are shown together with difference (green solid line) and the achieved R-factor for both laboratory (left column) and synchrotron (right column) PDF data.

In the laboratory data, fit quality was generally acceptable with R between 12.2 % (100 state) and 16.6 % (QA) except for the two states 5 and 300 with R = 22.5 % and 26.8 %, respectively. In the synchrotron data, good fits were obtained for all CCA states (R between 14.0 % for QA and 17.9 % for Q), however a systematic error in fitting of the PDF damping remained in all fits.

Refined values for the phase fraction of model γ′ phase and the lattice parameters of γ and γ′ phase were extracted from the fits of laboratory and synchrotron data. Figure 27 shows these results as a function of the CCA material state.

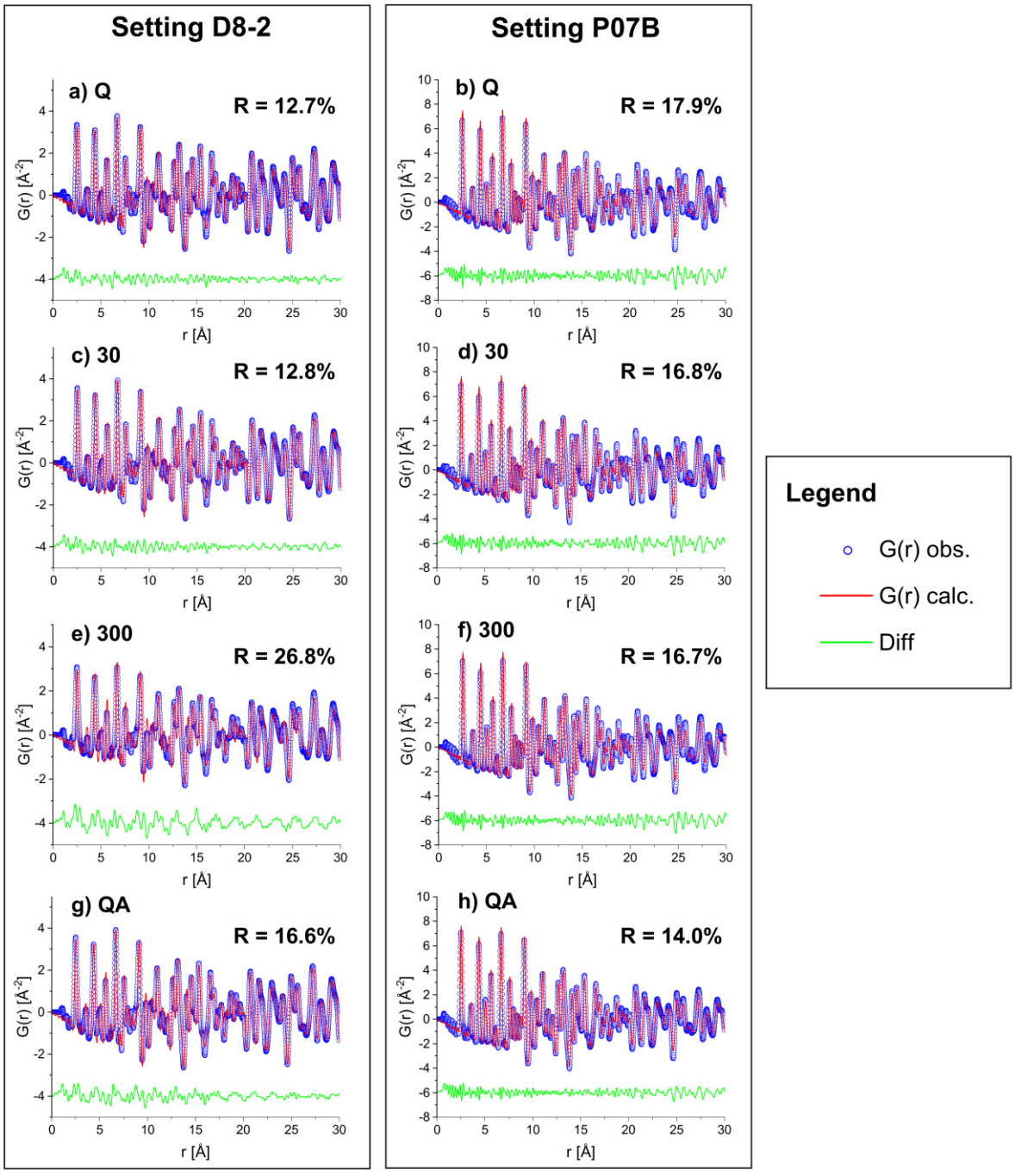

Figure 26: Graphical results from PDF fitting of laboratory (left column) and synchrotron (right column) PDF data from CCA states Q (a, b), 30 (c, d), 300 (e, f) and QA (g, h). Observed (blue open circles) and calculated (red solid lines) data plotted together with difference (green solid lines) and achieved R-factors.

The evolution of the refined γ′ phase fraction is given in Figure 27a, while Figure 27b and c show the evolution of the γ and γ′ lattice parameters, respectively. Results from PDF refinement (blue circles) are plotted in contrast to results from Rietveld refinement (red squares) of laboratory (full symbols) and synchrotron (open symbols) data reported earlier in section 4.6.1. Uncertainties are marked by error bars.

In PDF refinement of synchrotron data, the γ′ phase fraction was found to increase from 0.7 ± 11 at.% in the Q state to 33.6 ± 1.3 at.% in the QA state. As can be seen in Figure 27a, the refinement of laboratory data yielded a similar trend with increasing cooling time for the CCA states 5 (γ′ phase fraction: 5.1 ± 1.8 at.%) to QA (32.4 ± 2.1 at.%). In the maximally quenched Q state, the γ′ phase fraction could not be determined due to insufficient separability of the γ and γ′ model structures in this state.

Nonetheless, PDF refinement of both laboratory and synchrotron data revealed a trend of decreasing lattice parameter of the γ matrix phase with cooling time of the CCA states (see Figure 27b). While the γ lattice parameter was found from laboratory data to decrease from 3.5836 ± 0.013 Å in the Q state to 3.5729 ± 3E-4 Å in the QA state, the decrease found from synchrotron data was from 3.5932 ± 0.002 Å (Q) to 3.5821 ± 0.001 Å (QA).

Contrary to this, there is no clear trend with CCA material state in the evolution of the refined γ′ lattice parameter from either laboratory or synchrotron PDF data. From synchrotron PDF data, the refined γ′ lattice parameter was found to be similar between all considered the CCA states with a variation between 3.5896 ± 0.29 Å for the Q state to 3.5910 ± 0.003 Å for the QA state. From refinement of laboratory PDF data, however, the refined γ′ lattice parameter was found to fluctuate heavily with material state (see Figure 27c), taking values between 3.5837 ± 8E-4 Å (Q state) and 3.6703 ± 0.017 Å (10 state). In particular, it has to be pointed out that the γ′ lattice parameters found from PDF refinement in the more rapidly quenched states 5, 10, and 30 are highly overestimated in comparison to results from Rietveld refinement. This discrepancy is moderated in the states with lower quenching rate, i.e. 100 and 300, as well as in the QA reference state. For example, the refined γ′ lattice parameter of 3.5929 ± 0.020 Å in the QA state found from laboratory PDF refinement does not significantly differ from the value of 3.5910 ± 0.003 Å for the same state found from Rietveld refinement.

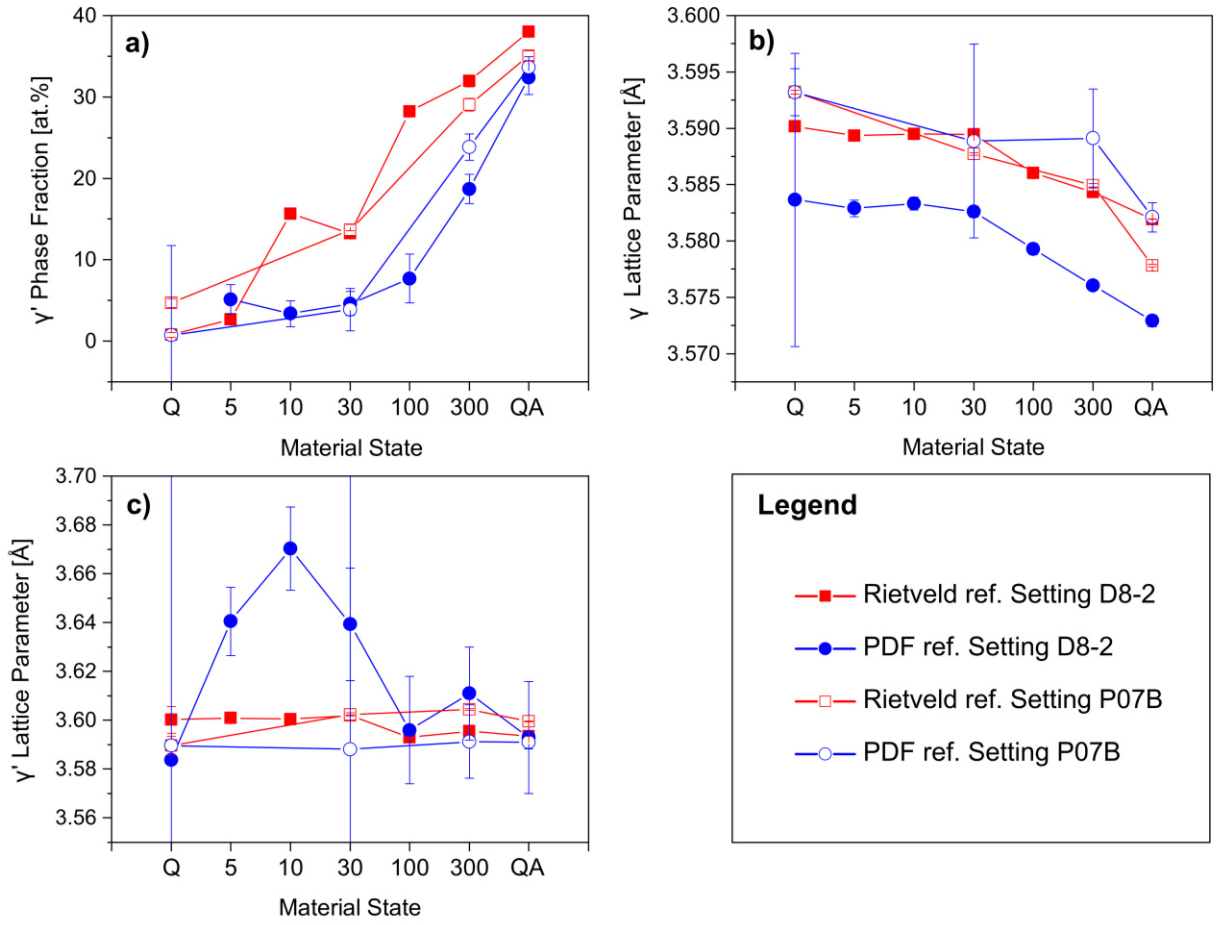

Figure 27: Comparison of (a) refined values for γ′ phase fraction, and lattice parameters of (b) γ matrix, and (c) γ′ phase from Rietveld (red squares) and PDF (blue circles) refinement of laboratory (full symbols) and synchrotron (open symbols) data.

5. Discussion

5.1. Assessment of laboratory XTS approach for PDF measurement

The laboratory approach for XTS experiments shall be assessed regarding its suitability for PDF measurement of powdered crystalline materials in general. For this, both the methodology of data collection and processing, as well as the quality of obtained PDF data of powdered Ni is reviewed critically. Ultimately, however, the laboratory approach was aimed at PDF measurement of solid crystalline samples such as the investigated Ni-11 wt.% Ti binary alloy and the precipitation-strengthened CCA, which will be discussed in greater detail in section 5.2.

5.1.1. Assessment of laboratory XTS data collection and processing

Radiation choice and *Q*-range. To obtain high quality PDF data, the scanned Q-range must be maximized to collect as much structural information as possible. In the presented laboratory approach, this was attempted by exhausting the technically possible scanning range for the scattering angle 2θ in the diffractometer up to $2\theta = 150\,°$, as well as employing a Mo anode giving X-rays of short wavelength (MoKα = 0.71 Å). With this, a maximum Q-value, i.e. Q_{max}, of 16.9 Å^{-1} could be achieved in the laboratory setting. In practice, most experimental setups for laboratory PDF measurement use MoKα radiation ($\lambda_{MoK\alpha}$ = 0.71 Å) [102,125–127,129,161,162], or AgKα radiation ($\lambda_{AgK\alpha}$ = 0.56 Å) [100,101,126,135,136,163–165], which allow $Q_{max} \cong 17$ Å^{-1} and $Q_{max} \cong 22$ Å^{-1}, respectively. Hence, by using an Ag anode instead of Mo, and for an otherwise identical setup, Q_{max} in the laboratory setting could have been increased to ideally 22 Å^{-1}. On the other hand, the benefit of Mo radiation compared to Ag radiation is the higher flux and higher detection efficiency of commonly used Si strip detectors [100,136].

In general, Q_{max} values of above 22 Å^{-1} in XTS experiments can only be obtained with synchrotron radiation. In recent works, PDF measurements were conducted using synchrotron radiation at various beamlines (e.g. ID11, ID15, ID22 and ID31 at ESRF; 6-ID-D, 11-ID-B and 11-ID-C at APS; A2 at CHESS; P02.1 at DESY) to achieve Q_{max} values between 18.5 Å^{-1} and, typically, 30 Å^{-1} [120,123–125,128,129,132,166–168]. In light of

this, it can be stated that with the laboratory approach of this work, the gap to the Q_{max} region of synchrotron approaches could be narrowed down to a difference of only 1.6 Å^{-1}. On the other hand, the Q_{max} value of 25.8 Å^{-1} reached in the synchrotron setting P07B of this work is situated in the typical range for synchrotron XTS experiments.

The spectrum of the employed Mo radiation in the laboratory settings contained both Kα_1 and Kα_2 components. In this regard, no subsequent data corrections for separation of the components were applied in the present work. Some authors, however, explicitly performed numerical elimination of Kα_2 contribution in laboratory PDF analysis [134,169], with Tsymbarenko et al. [169] finding that Kα_2-stripping significantly improved the resolution and peak positions in the obtained PDF of LaB_6 standard for $r > 35$ Å. This suggests that in future laboratory PDF analysis, elimination of non-principal radiation contributions (e.g. Kα_2 component) should be attempted and assessed with respect to the obtained PDF data.

Instrument *Q*-resolution. As a result of the high sampling rates of the total angular 2θ scan range in the laboratory settings D8-1 and D8-2, the instrumental Q-resolutions, $\Delta Q/Q$, achieved in the laboratory settings D8-1 and D8-2 significantly surpass the Q-resolution of the synchrotron setting P07B by an order of magnitude (see section 4.3). Corroborating this, Rietveld analysis of Ni data yielded higher refined values for Caglioti parameter W for setting P07B compared to settings D8-1 and D8-2, indicating broader, less resolved Bragg peaks (see section 4.3.2).

The higher Q-resolution in the laboratory settings is important for PDF measurement since lower resolution leads to increased decay of the PDF peak magnitude with increasing r, and to increased PDF peak broadening (see section 2.3.4.3). For example, Thomae et al. [100] found substantially decreased damping in laboratory PDF data of TiO_2 nanoparticles compared to synchrotron PDF data. To the knowledge of the author, in the field of PDF measurement, the instrumental resolutions obtainable with laboratory diffractometers are unrivaled by synchrotron data collection systems where such high resolutions can typically only be achieved at the cost of critically decreased Q_{max}.

Detector choice. To achieve higher counting statistics in the laboratory measurements, it was opted to employ an area detector EIGER2 R 500K with Si sensor in azimuth-optimized mode in setting D8-2 as compared to the Si strip detector

LYNXEYE XE-T used in setting D8-1. In recent works, both line detectors [101,102,125,135,136,162] and area detectors [100,126,129,164] have been successfully used for laboratory PDF measurement, with area detectors having the benefit of faster scanning rate compared to strip detectors. Furthermore, several works prove the potential of diffractometers from Bruker AXS, such as the diffractometer D8 Discover used in this work, for total scattering studies [126,162,164].

Statistics and data collection time. Using a VCT strategy and long data collection times of several hours in the laboratory settings, XTS data was collected with high instrumental *Q*-resolution and good signal-to-noise ratio, even at high *Q*-values up to Q_{max} (see section 4.2). The good signal-to-noise ratio at high *Q*-values must be emphasized as a strength of the laboratory XTS approach. This is because the sufficiently low noise component at high *Q*-values made it possible to almost use the full range of the collected data (data was collected up to $Q = 17.11$ Å^{-1}) in the PDF calculation. The marginal amount of $F(Q)$ data from 16.9 Å^{-1} to 17.11 Å^{-1} was trimmed to ensure that $F(Q_{max})$ data reached a value close to unity in order to minimize the termination error in the PDF. Also, since the high-*Q* region of $S(Q)$ and $F(Q)$ is amplified due to normalization (see section 2.3.3), the high quality of collected high-*Q* data translates into the PDF with a high weight.

In contrast to the laboratory measurements, in the synchrotron measurements conducted with setting P07B, an overall data acquisition time of only 0.1 s per image was used (plus summation of 10 single images per total image), which is low compared to data acquisition times of 8 s and 27 s used by Zea-Garcia et al. [125] for PDF analysis at beamlines ID15A and ID22 at ESRF, respectively. In mitigation, it was found there that increasing the acquisition time above these values did not yield significantly better PDF data. Still, it is suggested that for future synchrotron PDF measurement, the effect of data acquisition time in the order of 1 s and below on the quality of PDF data should be critically investigated.

Scattering from sample's environment. The increased background scattering intensity at scattering angles 2θ below 10 ° in laboratory setting D8-2 with respect to settings D8-1 and P07B (see section 4.3) is a result of undesired air scattering. In setting D8-1, the air scattering was shielded off with a blade-shaped MASS. For setting D8-2, however, the application of the MASS was found to coincide with critical

normalization errors in the integrated intensity data, giving rise to distorted low-r peaks in the obtained PDF data. The origin of these errors remains unclear at the time of writing this thesis. Hence, it was opted to omit the MASS in setting D8-2, purposefully neglecting the elimination of air scattering. This can potentially be detrimental for PDF analysis. For example, the spurious increased background scattering at low 2θ angles could compromise real coherent scattering from the sample at these angles that may contain crucial structural information, e.g. the superstructure peaks found in scattering patterns of the the CCA samples (see section 4.6.1).

Additionally, in both laboratory settings, at scattering angles 2θ angles below 10 °, also the glass sample holder beneath the sample was irradiated to some amount due to the elliptical beam spot on the sample exceeding the sample length of 40 mm. Therefore, also diffuse scattering from the sample holder was measured. However, it was not possible to separate the scattering contribution of the sample holder from the total scattered intensity, hence why this could not be corrected in subsequent data processing.

Data corrections. Collected data from the laboratory XTS measurements was not independently corrected for any inelastic and incoherent contributions such as Compton scattering before data processing with software PDFgetX3. Much rather, established empirical corrections for these contributions routinely implemented in software PDFgetX3 were exploited for this. While this undoubtedly facilitates the demanding data processing, it obviously takes away control and insight from the user regarding the exact applied data corrections, especially the treatment of background and diffuse scattering.

5.1.2. Comparison of laboratory XTS data generated with settings D8-1 and D8-2

In general, for both laboratory settings D8-1 and D8-2, agreement of collected and fitted XTS data of Ni was shown to be good from Rietveld refinement (see section 4.3.2). However, it was also seen there that considerable differences between measured and calculated scattering intensity remained for the major Bragg peaks (111) and (200) in data from setting D8-1, while these differences were smaller for setting D8-2. This indicates that the Bragg scattering model used in the Rietveld refinement

could not replicate the excessive scattering intensity for the first two Bragg peaks in setting D8-1.

The origin of these considerable intensity differences between settings D8-1 and D8-2 must lie in the different data collection and processing strategies employed in the different settings, as outlined in section 3.3. Most noticeably, in setting D8-1, the scattered beam was collimated by a secondary Soller slit with angular width of 2.5 ° before reaching the Si strip detector (i.e. only a 2.5 ° section of each diffraction ring was actually detected). In this setting, the full angular range of the scattering pattern was obtained simply from normalization of the observed counts of scattering events over the entire scanning time to counts per second. On the contrary, in setting D8-2, the observed section of each diffraction ring on the sensitive detector area was much larger as a consequence of using a two-dimensional detector in optimized position, and the full observed diffraction ring sections were integrated and automatically corrected using the full frame cursor in software DIFFRAC.EVA. This means that also the small remaining axial divergence of the beam, despite employing a Goebel mirror for parallel beam geometry, was included in the azimuthal integration, resulting in the instrument-related broadening of diffraction rings with increasing azimuth (see section 4.2.2). Hence, due to the different data collection and reduction schemes of the two settings, also the comparability of the PDF data calculated from the XTS data collected with either laboratory setting is limited. In line with this, the discrepancy between the experimental Ni PDFs obtained with settings D8-1 and D8-2, respectively, considerably increased with r (see section 4.4.2).

5.1.3. Assessment of quality of laboratory PDF data in comparison to synchrotron PDF data by the example of Ni

The higher Q-resolution achieved in the laboratory settings as compared to the synchrotron enlarged the accessible range of structural information in the laboratory PDF (up to 200 Å) compared to the synchrotron PDF (60-70 Å) (see section 4.4.2). In particular, this means that large-r structural features could only be inferred from the laboratory PDFs without disruptive instrument-related limits. This surplus of structural information can be crucial for in-depth structural analysis and accurate size determination of nanoparticles or precipitates with sizes above approximately 5 nm,

which is comparable to the estimated size of the γ′ precipitates in the more rapidly quenched states of the CCA investigated in this work (a more detailed discussion in this regard is given in section 5.2.4). As an example from literature, Sommariva [101] and Thomae et al. [100] independently were able to determine particle sizes between 7 and 9 nm for TiO_2 nanoparticle samples by refinement of laboratory PDF data.

The good agreement of the collected data with fitted data for a model FCC Ni structure (see section 4.4.1) further solidifies the high quality of the data and the laboratory approach. In the absence of comparable laboratory PDF data of Ni from literature, no validation of the measured data of this work with referential experimental data can be given. The closest reference is a laboratory PDF study on Ni conducted by Biswas et al. [135] using AgKα radiation, yet data there was only collected up to Q_{max} = 14.4 Å^{-1}, and PDF data was only calculated up to r = 20 Å, as opposed to r = 50 Å in this work. In PDF fitting with software PDFgui, the authors there obtained a goodness of fit (i.e. weighted R-factor) of R_w = 9.52 % for the r-range from 0 to 20 Å. The R-factors achieved in the present work over the r-range from 1.0 to 50.0 Å (D8-1: 16.63 %; D8-2: 15.52 %) were slightly larger than this, however they compare well to R-factors obtained for laboratory PDFs of other crystalline materials in literature [100,111,129]. Hence, it can be confidently said that with the presented laboratory XTS approach, for the first time, PDF data of Ni was fitted with high accuracy up to an r-value of 50 Å.

However, some shortcomings of the PDF data generated with laboratory setting D8-2 must be addressed. Firstly, undesired features contained in the laboratory XTS data, such as the unshielded background scattering from sample environment, most certainly leave spurious features in the PDF data. However, due to the vast difference in scattered intensity in comparison to Bragg scattering, it can be assumed that these effects are small in comparison to the features stemming from Bragg scattering. An exact quantification of the effect of these features on the PDF, however, is out of the scope of this work.

Secondly, the lower Q_{max} achieved in the laboratory settings compared to the synchrotron setting gave rise to a larger termination error. For example, the termination ripples and the larger peak width of the NN, 2NN, and 3NN peaks in the laboratory PDFs of Ni (see section 4.4.2) point to this. However, in mitigation it should

be stated that the achieved Q_{max} values of both laboratory and synchrotron approach fall significantly short of the threshold for a negligible termination error, i.e. $3/\sqrt{\langle u^2 \rangle}$ (see sections 2.3.4.3), calculated from the results of PDF refinement (see section 4.4.1). Hence, both laboratory and synchrotron PDF data were affected by a significant termination error. The theoretically required Q_{max} values for negligible termination error, according to the results from PDF refinement (see section 4.4.1), would lie between 35.6 $Å^{-1}$ and 43.6 $Å^{-1}$ for settings D8-1 and P07B, respectively, which can hardly be reached in practice, even with synchrotron radiation sources.

The absence of structural information in the laboratory PDFs contained in the high-Q region above 16.9 $Å^{-1}$ likely resulted in some small theoretically expected peaks in the low-r range of the laboratory PDFs, i.e. up to r = 15 Å not being resolved sufficiently. These peaks could only be identified in the synchrotron PDF data of Ni (see section 4.4.2). However, in mitigation, the gain of structural information linked to these peaks can be described as rather small. Hence, despite the lower Q_{max}, the laboratory Ni PDFs in the range from 0 to 15 Å were found to be qualitatively similar to their synchrotron counterpart in large parts, and thus it can be said that the relevant structural data were well retained in the laboratory PDFs using the laboratory approach.

Lastly, the structural fit parameters found from Rietveld and PDF refinement (see sections 4.3.2 and 4.4.1) shall be compared and assessed. While in Rietveld analysis, microstructural parameters such as phase fractions and the isotropic crystallite size could be refined, PDF analysis with PDFgui allowed insight into more atom-related parameters such as the isotropic ADPs (via fit parameter $\langle u^2 \rangle$), and the correlation of atomic motion (via parameter δ_2). In both Rietveld and PDF analysis, the lattice parameter of the Ni structure could be refined with high accuracy (uncertainties in the range of 10^{-4} to 10^{-5} Å), but only in the case of the synchrotron data, the results from either analysis agree within the uncertainty. In both laboratory settings D8-1 and D8-2, the refined lattice parameters from PDF analysis are significantly lower than from Rietveld analysis with differences of 0.0031 Å and 0.0067 Å, respectively. No definitive explanation for this discrepancy can be given at the time of writing this thesis, as this would require an in-depth parameter study of the calculation and fitting parameters of software PDFgetX3 and PDFgui, respectively. On the other hand, the refined values

for $\langle u^2 \rangle$ and δ_2 from PDF refinement of laboratory and synchrotron Ni PDFs were in the same order of magnitude and hence comparable. This indicates that with the PDF analysis of laboratory data, the magnitude of the atomic vibrations and the correlation of atomic motion in the investigated structure could largely be reproduced with respect to the benchmark synchrotron data.

5.2. Application of laboratory and synchrotron XTS approach for the study of atomic ordering in Ni-Ti binary alloy and CCA

The second aim of this work was to investigate ordering phenomena, in particular SRO, and their evolution with material state, in the Ni-Ti binary alloy and the precipitation-strengthened CCA. This was accomplished by analysis of the collected XTS and PDF data by means of Rietveld and PDF refinement, respectively, in corroboration with microstructural and chemical characterization methods.

The refinement of laboratory and synchrotron PDF data with software PDFgui, as used in the present work, is a 'small-box' modelling method, i.e. only structural parameters of one unit cell representing the entire structure are refined. In this aspect, it is comparable to the Rietveld refinement, which is also based on unit cell models [155,158]. This is opposed to 'large-box' modelling methods, as implemented in software such as RMCProfile [170] and DISCUS [115], in which the structure is refined atom by atom in larger volumes of typically several hundred unit cells. Hence, while the chosen method for PDF analysis is suited for the investigation of LRO phases such as the identified η and γ' phases in the Ni-Ti binary alloy and the CCA, respectively, it cannot account for SRO directly. Still, the method allows to draw conclusions about SRO as an extreme case where the LRO model structures cannot describe the data in sufficient manner anymore.

In this chapter, first the application of the laboratory XTS approach to solid samples from Ni-Ti binary alloy and the CCA shall be assessed with regard to sample preparation (section 5.2.1) as well as grain statistics and its influence on data quality (section 5.2.2). Then, the findings on ordered phases in Ni-Ti binary alloy (section 5.2.3) and CCA (section 5.2.4) are reviewed with a particular focus on indications of possible SRO. Finally, the suitability of the chosen method for PDF

analysis for the investigation of ordered phases in the two alloys of the present work is critically assessed.

5.2.1. Remarks on solid sample preparation

Using the laboratory XTS approach, total scattering of solid polycrystalline samples from Ni-Ti binary alloy and the CCA was measured. An important consideration reported in literature for PDF measurement in flat-plate reflection geometry, as in this work, is that the solid samples should be of uniform density with no macroscopic holes or cracks, have smooth surface, small and uniform grain sizes [75]. A uniform density is important to ensure that the atomic pair density encountered in the small irradiated volume is representative of the bulk material. If the surface is not smooth, X-ray absorption may reduce the intensity of peaks at low scattering angles 2θ. The grain size must be small to bring a high number of grains into diffracting position and thus enhance grain statistics. Egami & Billinge [75] mention that a mean grain size of solid samples below 40 μm is recommended for PDF analysis. This was achieved in the present work by processing the bulk Ni-Ti binary alloy and CCA from fine metallic powders, resulting in mean grain sizes of 12.24 μm ± 5 % and 23.18 μm ± 5 % in the Q states, respectively.

Secondly, texture formation in samples should be avoided by any means as it is not understood well how a pronounced texture quantitatively affects the PDF [171]. This was guaranteed in the present work by the manufacturing of samples via the PM route using HIP to minimize strain gradients in the materials that could lead to texture formation.

Lastly, care must be taken that the beam footprint on the sample does not extend over the edge of the sample at very low scattering angles 2θ below approximately 5 ° to avoid undesired scattering contributions from the sample's environment [75]. To achieve this in the present work, the sample length was defined to be at least 40 mm. However, the width of the heat-treated cylindrical samples was constrained to 4 mm by the geometrical requirements of the dilatometer employed for heat treatment. The particular length of 40 mm was inferred from calculations of the length of the elliptical beam footprint on the flat sample surface as a function of the scattering angle 2θ for the given primary goniometer radius of 350 mm. However, at lowest 2θ angles below

approximately 10 °, the beam footprint extending slightly over the sample edge could not be prevented, hence a low amount of undesired scattering from the glass sample holder was also included in the measured signal.

5.2.2. The issue of grain statistics in laboratory XTS measurements of solid samples

Due to the small required width of the cylindrical samples of only 4 mm, it was chosen in laboratory setting D8-2 to collimate the primary beam twice to ensure a width of the beam footprint on the sample surface of only approximately 1 mm. Of course, this severely limited the irradiated sample volume, and thus the grain statistics. However, the oscillation of the samples during the scans significantly mitigated this issue and increased particle statistics by approximately one order of magnitude (see section 4.2.1). This underscores the importance of sample oscillation for good particle statistics.

Still, the distinct 'spottiness' of diffraction rings in the laboratory XTS measurements of the solid Ni-Ti binary alloy and the CCA samples with setting D8-2 (see section 4.2.2) indicates that the achieved grain statistics were likely insufficient. Such an appearance of diffraction rings is a result of a low number of irradiated crystallites coming into diffracting position, resulting in fewer diffraction spots along the ring.

The grain statistics in an XTS experiment depend mainly on two things. Firstly, the mean grain volume in the sample is important. For example, assuming equiaxed grains, if the grain size in one dimension is doubled, the number of irradiated grains is reduced to an eighth assuming constant sample volume. This is exactly what was seen from comparison of the particle statistics between the Q states of Ni-Ti binary alloy and the CCA (see section 4.2.1). The calculated number of irradiated grains in the the CCA SA 1050-Q state was almost 8 times lower compared to the Ni-Ti SA 1200-Q state due to the mean grain size of 23.18 μm of the the CCA state being almost double the mean grain size in the Ni-Ti state, which was 12.24 μm. This underscores the necessity to produce samples with fine grain sizes, ideally below approximately 10 μm, for sufficient particle statistics.

Secondly, on part of the measurement parameters, the irradiated sample volume and thus the number of irradiated crystallites depends on the measurement geometry, as well as the radiation wavelength affect the number of irradiated crystallites during the scan. For transmission geometry, high-energy X-rays, and large area detectors, as was the case in the synchrotron setting P07B, grain statistics are not an issue since the irradiated sample volume then extends over the entire sample thickness. However, for reflection geometry and, in comparison, lower-energy radiation, such as in both laboratory settings D8-1 and D8-2, the issue of particle statistics becomes critical as in this case only those particles with diffracting lattice planes parallel to the sample surface contribute to the measured intensity [119]. In laboratory setting D8-2 however, the diffraction condition was much less strict, owing to the two-dimensional measurement. Firstly, the large 2θ range of approximately 10 ° covered by the area detector in each frame allows for many more particles in diffracting positions. Additionally, in setting D8-2, an area detector was used in azimuth-optimized mode (see section 3.3.1) to maximize the number of recorded scattering events. This certainly immensely improved statistics, yet apparently still did not fully eliminate the issue.

As a result of the insufficient grain statistics, it is likely that the number of crystallites in diffracting position significantly varied between otherwise comparable measurements of Ni-Ti binary alloy and the CCA samples. It is suspected that this led to the significant intensity differences between laboratory XTS data for these samples (see sections 4.5.1 and 4.6.1). In line with this, an effect of material state after HT and of texture formation on the observed intensity differences could largely be ruled out. First of all, no clear correlation between the intensity differences in the laboratory data with cooling time could be found for either the Ni-Ti states or the the CCA states. Also, texture formation in the samples was regarded to be very unlikely since all samples were machined from homogenized and HIPed bulk materials. Supporting this, the intensities of similar (h00) peaks (h = 2, 4, 6) in the scattering data from the CCA samples showed no indication for the presence of a texture in any of the the CCA samples (section 4.6.1).

Furthermore, the poor particle statistics likely introduced considerable errors into the laboratory PDFs. This is why laboratory PDFs of some Ni-Ti and the CCA states

showed inexplicably large differences already in the low *r*-region compared to the other states with no correlation to material state, for example the Ni-Ti SA 1200-100 state (see section 4.5.2) and the the CCA SA 1050-5 state (see section 4.6.2). This issue of course critically undermines the comparability of the laboratory PDFs, and complicates meaningful interpretation of the PDFs since the effect of poor particle statistics on the PDF cannot be well quantified or corrected [118,119].

5.2.3. Ordered phases in Ni-Ti binary alloy

In Ni-Ti binary alloy, SEM and EDX analysis revealed the presence of the ordered hexagonal η phase in the FC state in the form of nano-sized cuboidal precipitates (see Figure 4e and f). The formation of η phase is thought to occur in Ni-based alloys by consuming γ′ phase or by direct precipitation from the matrix during cooling [172]. Hence, it is possible that during FC of the Ni-Ti binary alloy, there was first precipitation of γ′ phase, followed by transformation to the observed η phase.

Refinement of laboratory PDFs yielded considerable η phase fractions in all quenched Ni-Ti states (weighted mean value: 4.25 ± 1.12 at.%), and an even higher phase fraction of 11.63 ± 2.50 at.% in the FC state, suggesting the presence of η phase in all considered Ni-Ti states. However, this was strongly contradicted by the results of Rietveld analysis of laboratory XTS data, where, in line with the results from SEM and EDX analysis, η phase was solely detected in the FC state with a refined phase fraction of 6.65 ± 5E-4 at.% (see section 4.5.1). The refinement of the synchrotron PDFs yielded more concise results in this regard (see section 4.5.3), with the estimated η phase fraction of 3.33 ± 1.7 at.% in the same range as that obtained from Rietveld refinement.

Hence, it can be said that while in relative terms, the PDF refinement of laboratory PDF data rightly reflected the change of the η phase fraction from quenched to FC state, the absolute phase fractions found there are falsely overestimated. It is assumed that the η phase fractions were overestimated by software PDFgui to compensate for the instrumental damping of the laboratory Ni-Ti PDFs described by fitting parameter Q_{damp}, which apparently could not be well reproduced with software PDFgui. Despite their nominally different crystal structure (FCC vs. hexagonal $D0_{24}$), the abundant γ matrix and the share multiple atomic positions with identical distances, i.e. they share multiple PDF peaks. Thus, by increasing the amount of η phase, certain PDF peaks

stemming also from the γ matrix could be better adjusted to the experimental damping of the laboratory PDFs, explaining the systematic overestimation.

However, the formation of η phase in the investigated Ni-Ti binary alloy is also reflected in the significant decrease of the γ matrix lattice parameter from Ni-Ti state 300 to FC found from Rietveld and PDF refinement of laboratory data (see sections 4.5.1 and 4.5.3). This is because η phase formation leads to a depletion of Ti in the γ matrix, resulting in a lower γ lattice parameter [172]. The decrease of the γ lattice parameter could also be inferred from the observed shift of PDF peaks in the laboratory Ni-Ti PDFs to lower *r*-values (see section 4.5.2).

Additionally, TiC phase was identified in all Ni-Ti binary alloy samples (see section 4.1). This is likely due to suspected carburization of the compacted Ni-Ti binary alloy powder from the steel capsule during HIP. Rietveld refinement of laboratory XTS data, where distinct TiC peaks could be observed (see section 4.5.1) suggested similar TiC phase fractions in the considered Ni-Ti states with a weighted mean value of 3.81 at.% (see section 4.5.3). However, in PDF refinement of laboratory PDF data, the TiC phase fractions was estimated to be negligibly small in all considered Ni-Ti states, while at the same time the η phase was overestimated compared to Rietveld refinement. This shows that the PDF analysis method in combination with laboratory PDF data for the Ni-Ti binary alloy was not sensitive to ordered phases present in low amounts in contrast to Rietveld refinement.

5.2.4. Ordered phases in the CCA: Transition from LRO γ' precipitation to suspected SRO

SEM and EDX analysis revealed the presence of ordered coherent γ' phase in the CCA 300 and QA state in the form of precipitates with sizes between 10 and 20 nm and phase fractions of 31 vol.% and 18 vol.%, respectively, while no indication of this ordered phase was found for the other quenched CCA states (see sections 4.1). In line with the results from SEM and EDX analysis of the aged state, Rietveld refinement of laboratory and synchrotron XTS data suggested γ' phase fractions of 38.0 ± 0.5 at.% and 35.1 ± 0.6 at.%, respectively (see section 4.6.1). Similarly, PDF refinement of laboratory and synchrotron data suggested γ' phase fractions in the QA state of 32.4 ± 0.02 at.% and 33.6 ± 0.01 at.%, respectively (see section 4.6.3).

The precipitation of ordered γ′ phase in the CCA investigated in this work is in line with findings from literature for similar precipitation-strengthened CCAs. For example, Chang et al. [30] computed that the equilibrium phase constitution of the precipitation-strengthened CCA $Al_{3.63}Co_{27.27}Cr_{18.18}Fe_{18.18}Ni_{27.27}Ti_{5.45}$, from which the CCA investigated in this work is derived, is FCC γ matrix + $L1_2$-structured γ′ phase. SEM analysis of the 750 °C/50 h aged state of the CCA in that work suggested a γ′ phase fraction of approximately 28 vol.%. Corroborating this, Biermair et al. [64], who investigated a similar precipitation-strengthened CCA, found a γ′ phase fraction of approximately 35 vol.% from APT reconstructions of the same aged state.

However, in analysis of laboratory and synchrotron XTS data, also the other quenched CCA samples were found to exhibit superstructure peaks at scattering angles 2θ below 30 ° (see section 4.6.1). Superstructure peaks arise from additional ordered structures superimposed on a higher-symmetry crystal structure such as the FCC structure in the case of the CCA. For a random or disordered SS alloy with FCC structure, which is an idealized state of the CCA after sufficient holding time in the SA temperature regime, these peaks are forbidden by symmetry.

The origin of the specific observed superstructure peaks could be linked to the presence of γ′ phase also in the rapidly quenched CCA states. The γ′ superstructure peaks found in the scattering data of the CCA investigated in this work evolved from sharp peaks in the QA and the states with lower quenching rate (300, 100) to much more broadly diffuse 'bumps' in the states with higher quenching rate (Q, 5, 10). For the Q state, these 'bumps' seem to almost disappear in the background scattering (see section 4.6.1). This is also reflected in the evolution of the relative peak height and the FWHM of the superstructure peaks with material state (see section 4.6.1). The broadening of the γ′ superstructure peaks indicates a decrease in precipitate size and volume fraction of the (partially) ordered γ′ phase with increasingly rapid quenching rates. From comparison to the γ′ particle size observed in SEM analysis of the CCA QA state, which was between 10 and 20 nm (see Figure 5d and e), the size of the (partially) ordered regions in the maximally quenched states (Q, 5) can be assumed to be smaller than 5 nm. This is below the resolution limit reached in SEM, which is why no indication of the regions could be found in the SEM images.

The evolution of the γ′ superstructure peaks with increasing quenching rate from sharp Bragg peaks towards broad 'bumps' (see Figure 16d and Figure 18) is interpreted as a transition from LRO γ′ precipitation to suspected SRO extending over only a few nanometers in the investigated CCA. Strengthening this hypothesis, it is generally understood that SRO in crystalline materials gives rise to diffuse scattering (see section 2.3.1). In particular, if LRO structures are replaced by SRO regions, the Bragg peaks associated with the LRO structure become so broad that they appear as diffuse 'bumps' in the scattering pattern. For example, Proffen et al. [167] compared total scattering patterns from ordered and disordered Cu_3Au, and found the sharp superstructure peaks (100) and (110) in the ordered state to be replaced by a broad 'bump' at $2\theta \cong 7\,^\circ$ in the disordered state, indicating chemical SRO of Cu and Au in the latter. Furthermore, Biermair et al. [64] found small (approximately 3 nm sized) regions enriched in Ni and Ti in the WQ state of a similar CCA from APT reconstructions after homogenization (1150 °C/12 h/in air) and SA, hinting at possible SRO between Ni and Ti in this alloy. They also investigated material states after 10, 30 and 50 h of aging, where growth of such regions, which were identified as γ′ precipitates in these states, was observed to average sizes of 11-14 nm. Hence, it can be assumed that in the maximally quenched states of the CCA investigated in this work, SRO of Ni and Ti is present as an early stage and precursor of γ′ precipitation.

The presence of such SRO regions even in the maximally quenched CCA state (Q) shows the high ordering tendencies between different atom types, mainly between Ni, and Al and Ti, in the CCA. This leads to the assumption that this material can hardly be manufactured in a totally supersaturated state. The particular ordering between said elements, Ni, Al and Ti, is also plausible from thermodynamic considerations. The binary enthalpies of mixing between different pairs of elements in the Al-Co-Cr-Fe-Ni-Ti system in the liquid state [173] are depicted in Figure 28. It can be seen that the binary enthalpies of mixing are the most negative for the pairs Ni and Al (-22 kJ/mol), and Ni and Ti (-35 kJ/mol), indicating a strong ordering tendency between these atom types. In this light, it may even seem plausible that SRO between Ni, Al and Ti is already present to some degree in the investigated CCA in the SA temperature regime, i.e. at 1050 °C.

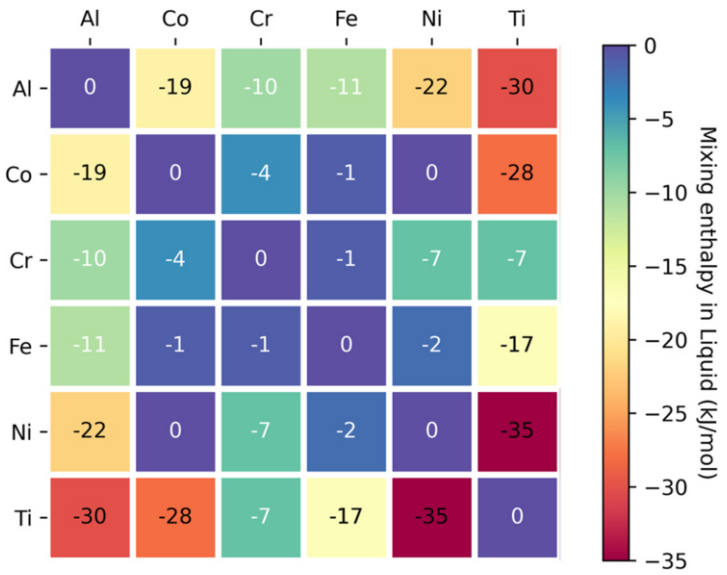

Figure 28: Calculated binary enthalpies of mixing for elements in the Al-Co-Cr-Fe-Ni-Ti system in the liquid state [173] *(figure adopted from* [174]*). Mixing enthalpies reach most negative values for Ni-Ti, Ni-Al, and Ti-Al pairs, indicating strong ordering tendency.*

The evolution towards increased γ′ precipitation with increasing cooling time of the investigated CCA states up to the QA state is evident from Rietveld refinement of both laboratory and synchrotron XTS data (see section 4.6.1). In Figure 27a, a consistent increase of γ′ phase fraction with cooling time of the CCA could be seen from 0.76 ± 0.28 at.% in the Q state to 38.04 ± 0.50 at.% in the QA state in the laboratory data, and from 4.68 ± 0.54 at.% (Q) to 35.06 ± 0.62 at.% (QA) in synchrotron data. Shown in the same graph, PDF refinement of both laboratory and synchrotron data yielded a similar trend of γ′ phase fraction with material state. Additionally, Rietveld refinement of laboratory and synchrotron XTS data showed a significant decrease of the γ lattice parameter with increasing cooling time from Q to QA state, while the refined γ′ lattice parameter remained largely constant, or slightly decreased with material state (see section 4.6.3). The decrease of the γ lattice parameter, which is caused by the depletion of Ti and Al in the matrix upon γ′ precipitation [64], could also be inferred directly from laboratory and synchrotron PDFs of the CCA. There, a shift of PDF peaks to lower *r*-values, i.e. smaller interatomic distances, with increasing cooling time was visible (see Figure 25). In line with this, PDF refinement of laboratory and synchrotron PDF data of the investigated CCA also showed a decrease of the γ lattice parameter with cooling time (see Figure 27). However, in laboratory PDF refinement, the refined γ′ lattice parameter was falsely overestimated in the more

rapidly quenched CCA states (5, 10) with refined values up to 3.67 Å, which is contradicted by the coherent nature of the γ′ phase in the investigated alloy.

The observed increasing lattice parameter mismatch between γ and γ′ phase with cooling time indicates the accumulation of increasingly long-ranging microstrain at the γ-γ′ phase boundaries in the investigated CCA upon γ′ precipitation. The increased microstrain in the CCA samples resulted in a broadening of Bragg peaks with increasing cooling time from Q to QA state, which is visible in the high-2θ region of the laboratory XTS data shown in Figure 16d. This strain-induced Bragg peak broadening, in turn, led to a stronger damping of the PDFs with CCA material state, which was observed for both laboratory and synchrotron data (see Figure 22). The observed damping was more pronounced in the laboratory data than in the synchrotron data, which could stem partially from the larger spatial extent of the laboratory PDFs compared to the synchrotron PDFs, but could also be exaggerated to a certain degree due to measurement discrepancies with setting D8-2.

Unfortunately, the presence of γ′ phase could not be directly inferred from either laboratory or synchrotron PDF data of the CCA investigated in this work. The local chemical deviations, particularly of Ni and Ti, between the γ matrix and the coherent γ′ phase or SRO regions apparently could not be resolved in either laboratory or synchrotron PDF data. This is evident by the evolution of PDF peak height and peak width of the NN, 2NN, and 3NN peaks (see Figure 24), which showed no significant correlation with material state of the investigated CCA. Theoretically, one might expect that the increased local chemical ordering with increasing cooling time would lead to different heights of PDF peaks, in particular those corresponding to the NN, 2NN, and 3NN interactions, due to the difference in scattering power between different elements (see section 2.3.3). For example, Proffen et al. [167] observed significant differences in the first few PDF peaks between ordered and disordered Cu_3Au.

However, it must be stated that the PDF analysis of the early stages of γ′ precipitation in the investigated CCA was severely complicated from the beginning on the part of the material itself for two reasons. First, due to the coherent nature of the γ′ phase having the same principal atomic arrangement as the γ matrix, no significant change of the peak sequence in the PDF indicative of ordering was to be expected. Secondly,

due to the low amounts of γ′-forming elements Ti (5.87 at.%) and Al (3.29 at.%) in the CCA, the chemical differences between the γ matrix and the coherent SRO or LRO γ′-type regions were so marginal in terms of atomic scattering factors, that their effect on the low-*r* region of the laboratory and synchrotron PDFs was likely overshadowed by instrumental influences such as the termination error, as well as – in the case of laboratory setting D8-2 – the significant differences in scattered intensity resulting from pronounced 'spotiness' of the recorded diffractograms (see sections 4.2.2 and 5.2.2). Hence, despite the aforementioned experimental shortcomings of the laboratory approach in setting D8-2 compared to setting P07B, it can be assumed that the direct observation of SRO between Ni and Ti in the investigated CCA from PDF analysis is hardly possible in general.

6. Conclusion & Outlook

The first aim of the present work was to present and assess a laboratory approach for PDF measurement of crystalline materials. Two laboratory settings using a diffractometer D8 Discover from Bruker AXS in reflection geometry were presented in detail. Key requirements for PDF measurement, such as high Q-range, and sufficient counting statistics, were satisfied by using Mo radiation and utilizing a VCT strategy together with long data collection times of several hours, as well as using an area detector in setting D8-2. With this laboratory setup, a value of Q_{max} = 16.9 Å^{-1} could be achieved, which can be regarded as satisfactory in the scope of laboratory PDF measurement, but naturally falls short of the synchrotron setting at beamline P07B, where the achieved Q_{max} was 25.8 Å^{-1}.

From comparison of the generated laboratory PDF data for standard Ni powder with synchrotron data and data from literature, however, it can still be concluded that with the laboratory approach, high-quality PDFs of crystalline structures can be measured. Highlighting the strength of the laboratory approach, the high instrument Q-resolution reached in the laboratory settings produced structural information in the PDFs up to r = 200 Å or 20 nm, as opposed to only r = 70 Å or 7 nm in the synchrotron PDFs. This can be crucial for the structural investigation of nanoparticles with sizes above approximately 7 nm.

However, the unresolved issue of eliminating undesired background scattering from air and sample holder at small scattering angles 2θ in laboratory setting D8-2 makes the presented approach objectionable, and must be addressed on all accounts in future work. One solution would be to perform a corrective measurement on a highly crystalline calibration sample of same geometry as the actual samples of interest which gives no diffraction peaks in the critical 2θ range below approximately 20 °, e.g. high-Miller index Si crystals.

The second aim of the present work was the investigation of ordering effects, and in particular SRO, in solid polycrystalline samples from Ni-Ti binary alloy and a precipitation-strengthened CCA as a function of cooling time after SA. For this, Rietveld and PDF analysis of laboratory and synchrotron data from settings D8-2 and

P07B, respectively, were used in combination with microstructural and chemical characterization methods, i.e. SEM and EDX analysis.

Requirements on samples for the laboratory PDF measurement in reflection geometry, such as uniform density, smooth surface, and negligible texture, were satisfied with the chosen preparation methods. In particular, HIP of the utilized material powders with small particle sizes below 25 μm guaranteed small to no sample texture. However, the crucial prerequisite for sufficient grain statistics in the laboratory measurement of the solid samples could not be met, and led to distinct 'spotiness' of recorded diffractograms for both Ni-Ti binary alloy and CCA samples in laboratory setting D8-2. As a result, considerable discrepancies in scattered intensity arose between different material states in the laboratory XTS data, which likely had a detrimental effect also on the PDFs. Hence, the improvement of grain statistics in laboratory PDF measurement must be addressed in future work. To this end, three reasonable suggestions can be made. Firstly, grain size of solid samples should be reduced to below approximately 10 μm. Also, care should be taken to avoid large grain growth during manufacturing and heat treatment of samples. Secondly, it would be desirable for samples to have larger width compared to the cylindrical samples in this work. This way, in future laboratory XTS experiments, the full beam width of approximately 12-15 mm could be used, thereby allowing for a much larger irradiated sample volume. Lastly, while the oscillation of the samples during the measurement significantly added to the grain statistics, further movement of samples is thinkable, e.g. rocking about the sample axis, to bring even more crystallites into diffraction.

In the Ni-Ti binary alloy, the ordered hexagonal η phase was found after slow cooling in the FC state, with no indication of ordered phases in the quenched Ni-Ti states. In this regard, the findings from SEM and EDX analysis were corroborated by results from Rietveld refinement of the measured XTS data, but PDF refinement falsely overestimated the amount of η phase in the quenched Ni-Ti states. This showed that the chosen method for PDF analysis had trouble modelling the instrument-related effects in the case of laboratory PDFs, and to separate this from the influence of ordered phases with low amounts and similar atomic structure as the matrix.

In the investigated CCA, γ′ phase with a phase fraction of approximately 30 vol.% was revealed in the QA state by SEM and EDX analysis, and γ′ superstructure peaks

found in the measured XTS data indicated the presence of an ordered coherent phase of γ′ type also in the rapidly quenched CCA states. The evolution of the superstructure peaks with increasing quenching rate from sharp Bragg peaks in the QA state to broadly 'diffuse' bumps in the maximally quenched CCA states was interpreted as a transition from LRO γ′ phase to smaller SRO regions enriched in Ni and Ti acting as precursors for γ′ formation in the investigated CCA. This hypothesis is supported by findings in literature, and would deepen the understanding of the formation mechanism of the strengthening γ′ phase not only in the CCA, but in general. The transition towards increased γ′ phase fraction in the CCA states with longer cooling time up to the aged state was shown not only from Rietveld refinement of laboratory and synchrotron XTS data, but also from PDF refinement of synchrotron data. Additionally, both Rietveld and PDF refinement revealed a simultaneous decrease of the γ lattice parameter and a stagnation, or slight increase of the γ′ lattice parameter with increasing cooling time of the CCA, indicating the accumulation of microstrain in the CCA samples upon γ′ precipitation.

The evolution of γ′ precipitation in the CCA could be inferred indirectly from the shift of PDF peaks towards lower *r*-values with increasing cooling time, reflecting the decrease of the γ lattice parameter observed with other methods, as well as from an increased strain-induced damping of laboratory and synchrotron PDFs of the CCA. However, no direct evidence for γ′ or SRO in the CCA could be found from either laboratory or synchrotron PDFs. This can be attributed to instrument-related influences overshadowing the decisive small features in PDFs indicative of SRO. However, this was further complicated on part of the investigated material due to the coherent nature of the γ′ phase, and the low amounts of SRO- or γ′-forming elements Ti and Al in the CCA. Hence, a direct observation of SRO between Ni and Ti in the investigated CCA using PDF analysis is likely hardly possible in general.

In this regard, two paths for future research can be sketched. On the methodological part, an optimized laboratory approach for PDF analysis could be tested on chemically simpler systems such as the extensively studied Cu_3Au. On the material part, direct observation of SRO in the investigated precipitation-strengthened CCA would necessitate atomic resolution imaging techniques such as APT and HR-TEM, as were used for this with success in two recent works [53,60].

In conclusion, this work proved that PDF analysis in combination with the presented laboratory approach for PDF measurement can be a valuable and comparably fast tool for investigation and characterization of the local structure of polycrystalline materials and also alloys with increased chemical complexity up to CCAs. This will pave the way to a more fundamental understanding of the effect of atomic-scale ordering on the material properties of CCAs designed for highly demanding applications in the future.

List of references

[1] D.B. Miracle, O.N. Senkov, A critical review of high entropy alloys and related concepts, Acta Mater. 122 (2017) 448–511. https://doi.org/10.1016/j.actamat.2016.08.081.

[2] J. Chen, X. Zhou, W. Wang, B. Liu, Y. Lv, W. Yang, D. Xu, Y. Liu, A review on fundamental of high entropy alloys with promising high–temperature properties, J. Alloys Compd. 760 (2018) 15–30. https://doi.org/10.1016/j.jallcom.2018.05.067.

[3] Y. Zhang, T.T. Zuo, Z. Tang, M.C. Gao, K.A. Dahmen, P.K. Liaw, Z.P. Lu, Microstructures and properties of high-entropy alloys, Prog. Mater. Sci. 61 (2014) 1–93. https://doi.org/10.1016/j.pmatsci.2013.10.001.

[4] J. Brechtl, S. Chen, C. Lee, Y. Shi, R. Feng, X. Xie, D. Hamblin, A.M. Coleman, B. Straka, H. Shortt, R.J. Spurling, P.K. Liaw, A review of the serrated-flow phenomenon and its role in the deformation behavior of high-entropy alloys, Metals (Basel). 10 (2020) 1–72. https://doi.org/10.3390/met10081101.

[5] S. Maiti, W. Steurer, Structural-disorder and its effect on mechanical properties in single-phase TaNbHfZr high-entropy alloy, Acta Mater. 106 (2016) 87–97. https://doi.org/10.1016/j.actamat.2016.01.018.

[6] S. Pourbabak, X. Wang, D. Van Dyck, B. VerlinDen, D. Schryvers, Ni cluster formation in low temperature annealed Ni50.6Ti49.4, Funct. Mater. Lett. 10 (2017) 1–7. https://doi.org/10.1142/S1793604717400057.

[7] H.L. Hong, Q. Wang, C. Dong, P.K. Liaw, Understanding the Cu-Zn brass alloys using a short-range-order cluster model: Significance of specific compositions of industrial alloys, Sci. Rep. 4 (2014) 10–13. https://doi.org/10.1038/srep07065.

[8] L. Reinhard, B. Schönfeld, G. Kostorz, W. Bührer, Short-range order in -brass, Phys. Rev. B. 41 (1990) 1727–1734. https://doi.org/10.1103/PhysRevB.41.1727.

[9] H. Wood, G.D.W. Smith, A. Cerezo, Short range order and phase separation in Ti-Al alloys, Mater. Sci. Eng. A. 250 (1998) 83–87. https://doi.org/10.1016/S0921-5093(98)00540-1.

[10] S. Pourbabak, X. Wang, B. Verlinden, J. Van Humbeeck, D. Schryvers, Short-range-order (SRO) in quenched Ni-rich Ni-Ti alloys, Eur. Microsc. Congr. 2016 Proc. (2016) 635–636. https://doi.org/10.1002/9783527808465.emc2016.6780.

[11] P.R. Okamoto, G. Thomas, On short range order and micro-domains in the Ni4Mo system, Acta Metall. 19 (1971) 825–841. https://doi.org/10.1016/0001-6160(71)90139-8.

[12] X. Chang, M. Zeng, K. Liu, L. Fu, Phase Engineering of High-Entropy Alloys, Adv. Mater. 32 (2020) 1–22. https://doi.org/10.1002/adma.201907226.

[13] Z. Tang, Processing , Microstructures , and Mechanical Behavior of High-

Entropy Alloys, (2012).

[14] D.B. Miracle, High-Entropy Alloys: A Current Evaluation of Founding Ideas and Core Effects and Exploring "Nonlinear Alloys," Jom. 69 (2017) 2130–2136. https://doi.org/10.1007/s11837-017-2527-z.

[15] M.C. Gao, J.-W. Yeh, P.K. Liaw, Y. Zhang, High-Entropy Alloys, n.d.

[16] J.W. Yeh, S.K. Chen, S.J. Lin, J.Y. Gan, T.S. Chin, T.T. Shun, C.H. Tsau, S.Y. Chang, Nanostructured high-entropy alloys with multiple principal elements: Novel alloy design concepts and outcomes, Adv. Eng. Mater. 6 (2004) 299–303. https://doi.org/10.1002/adem.200300567.

[17] B. Cantor, I.T.H. Chang, P. Knight, A.J.B. Vincent, Microstructural development in equiatomic multicomponent alloys, Mater. Sci. Eng. A. 375–377 (2004) 213–218. https://doi.org/10.1016/j.msea.2003.10.257.

[18] J.-W. Yeh, S.-J. Lin, T.-S. Chin, J.-Y. Gan, P.-H. Lee, T.-T. Shun, C.-H. Tsau, S.-Y. Chou, Formation of simple crystal structures in Cu-Co-Ni-Cr-Al-Fe-Ti-V alloys with multiprincipal metallic elements, Metall. Mater. Trans. A. 35 (2004) 2533–2536. https://doi.org/10.1007/s11661-006-0234-4.

[19] F. Otto, A. Dlouhý, C. Somsen, H. Bei, G. Eggeler, E.P. George, The influences of temperature and microstructure on the tensile properties of a CoCrFeMnNi high-entropy alloy, Acta Mater. 61 (2013) 5743–5755. https://doi.org/10.1016/j.actamat.2013.06.018.

[20] A. Gali, E.P. George, Tensile properties of high- and medium-entropy alloys, Intermetallics. 39 (2013) 74–78. https://doi.org/10.1016/j.intermet.2013.03.018.

[21] N. Gao, D.H. Lu, Y.Y. Zhao, X.W. Liu, G.H. Liu, Y. Wu, G. Liu, Z.T. Fan, Z.P. Lu, E.P. George, Strengthening of a CrMnFeCoNi high-entropy alloy by carbide precipitation, J. Alloys Compd. 792 (2019) 1028–1035. https://doi.org/10.1016/J.JALLCOM.2019.04.121.

[22] K. Zhang, H. Wen, B. Zhao, X. Dong, L. Zhang, Precipitation behavior and its impact on mechanical properties in an aged carbon-containing Al0.3Cu0.5CrFeNi2 high-entropy alloy, Mater. Charact. 155 (2019) 109792. https://doi.org/10.1016/J.MATCHAR.2019.109792.

[23] W.H. Liu, J.Y. He, H.L. Huang, H. Wang, Z.P. Lu, C.T. Liu, Effects of Nb additions on the microstructure and mechanical property of CoCrFeNi high-entropy alloys, Intermetallics. 60 (2015) 1–8. https://doi.org/10.1016/J.INTERMET.2015.01.004.

[24] Y.T. Chen, Y.J. Chang, H. Murakami, S. Gorsse, A.C. Yeh, Designing high entropy superalloys for elevated temperature application, Scr. Mater. 187 (2020) 177–182. https://doi.org/10.1016/j.scriptamat.2020.06.002.

[25] A.. Yeh, T.K. Tsao, Y.J. Chang, K.C. Chang, J.W. Yeh, M.S. Chiou, S.R. Jian, C.M. Kuo, W.R. Wang, H. Murakami, Developing New Type of High Temperature Alloys–High Entropy Superalloys., Int. J. Metall. Mater. Eng. 1 (2015) 1–4. http://dx.doi.org/10.15344/2455-2372/2015/107%0AInternational.

[26] Q. Wang, Z. Li, S. Pang, X. Li, C. Dong, P.K. Liaw, Coherent precipitation and

strengthening in compositionally complex alloys: A review, Entropy. 20 (2018). https://doi.org/10.3390/e20110878.

[27] R.C. Reed, The Superalloys: Fundamentals and Applications, Cambridge University Press, 2006. https://doi.org/10.1017/CBO9780511541285.

[28] Y.L. Zhao, T. Yang, Y.R. Li, L. Fan, B. Han, Z.B. Jiao, D. Chen, C.T. Liu, J.J. Kai, Superior high-temperature properties and deformation-induced planar faults in a novel L12-strengthened high-entropy alloy, Acta Mater. 188 (2020) 517–527. https://doi.org/10.1016/j.actamat.2020.02.028.

[29] T. Yang, Y. Zhao, W. Liu, J. Kai, C. Liu, L12-strengthened high-entropy alloys for advanced structural applications, J. Mater. Res. 33 (2018) 2983–2997. https://doi.org/10.1557/jmr.2018.186.

[30] Y.J. Chang, A.C. Yeh, The evolution of microstructures and high temperature properties of AlxCo1.5CrFeNi1.5Tiy high entropy alloys, J. Alloys Compd. 653 (2015) 379–385. https://doi.org/10.1016/j.jallcom.2015.09.042.

[31] W. Li, D. Xie, D. Li, Y. Zhang, Y. Gao, P.K. Liaw, Mechanical behavior of high-entropy alloys, Prog. Mater. Sci. 118 (2021) 100777. https://doi.org/10.1016/j.pmatsci.2021.100777.

[32] M.R. Chen, S.J. Lin, J.W. Yeh, S.K. Chen, Y.S. Huang, C.P. Tu, Microstructure and properties of Al0.5CoCrCuFeNiTix (x = 0-2.0) high-entropy alloys, Mater. Trans. 47 (2006) 1395–1401. https://doi.org/10.2320/matertrans.47.1395.

[33] M.H. Chuang, M.H. Tsai, W.R. Wang, S.J. Lin, J.W. Yeh, Microstructure and wear behavior of AlxCo1.5CrFeNi1.5Tiy high-entropy alloys, Acta Mater. 59 (2011) 6308–6317. https://doi.org/10.1016/J.ACTAMAT.2011.06.041.

[34] C.-Y. Hsu, J.-W. Yeh, S.-K. Chen, T.-T. Shun, Wear resistance and high-temperature compression strength of Fcc CuCoNiCrAl0.5Fe alloy with boron addition, Metall. Mater. Trans. A. 35 (2004) 1465–1469. https://doi.org/10.1007/s11661-004-0254-x.

[35] S.T. Chen, W.Y. Tang, Y.F. Kuo, S.Y. Chen, C.H. Tsau, T.T. Shun, J.W. Yeh, Microstructure and properties of age-hardenable AlxCrFe1.5MnNi0.5 alloys, Mater. Sci. Eng. A. 527 (2010) 5818–5825. https://doi.org/10.1016/j.msea.2010.05.052.

[36] E.J. Pickering, N.G. Jones, High-entropy alloys: a critical assessment of their founding principles and future prospects, Int. Mater. Rev. 61 (2016) 183–202. https://doi.org/10.1080/09506608.2016.1180020.

[37] J. Dąbrowa, M. Danielewski, State-of-the-art diffusion studies in the high entropy alloys, Metals (Basel). 10 (2020). https://doi.org/10.3390/met10030347.

[38] Z. Li, S. Zhao, R.O. Ritchie, M.A. Meyers, Mechanical properties of high-entropy alloys with emphasis on face-centered cubic alloys, Prog. Mater. Sci. 102 (2019) 296–345. https://doi.org/10.1016/J.PMATSCI.2018.12.003.

[39] L. Guo, J. Gu, X. Gong, K. Li, S. Ni, Y. Liu, M. Song, Short-range ordering induced serrated flow in a carbon contained FeCoCrNiMn high entropy alloy,

Micron. 126 (2019). https://doi.org/10.1016/j.micron.2019.102739.

[40] J.B. Cohen, M.E. Fine, Some aspects of short-range order, J. Phys. Le Radium. 23 (1962) 749–762. https://doi.org/10.1051/jphysrad:019620023010074901.

[41] J.M. Cowley, An approximate theory of order in alloys, Phys. Rev. 77 (1950) 669–675.

[42] J.M. Cowley, Short- and long-range order parameters in disordered solid solutions, Phys. Rev. 120 (1960) 1648–1657. https://doi.org/10.1103/PhysRev.120.1648.

[43] C. Wolverton, V. Ozoliņš, A. Zunger, Short-range-order types in binary alloys: A reflection of coherent phase stability, J. Phys. Condens. Matter. 12 (2000) 2749–2768. https://doi.org/10.1088/0953-8984/12/12/314.

[44] L. Trieb, G. Veith, Kinetic study of short range order in α-CuAl alloys, Acta Metall. 26 (1978) 185–196. https://doi.org/10.1016/0001-6160(78)90215-8.

[45] H. Warlimont, H.P. Aubauer, Disperse Ordnung - ein Modell für den teilgeordneten Zustand konzentrierter Legierungsmischkristalle, I. Exp. Beobachtungen und Grundlagen des Modells. 64 (1973) 484–491. https://doi.org/doi:10.1515/ijmr-1973-640704.

[46] L.R. Owen, H.Y. Playford, H.J. Stone, M.G. Tucker, A new approach to the analysis of short-range order in alloys using total scattering, Acta Mater. 115 (2016) 155–166. https://doi.org/10.1016/j.actamat.2016.05.031.

[47] M. Zehetbauer, L. Trieb, H.P. Aubauer, Effect of Short-Range Order on the Mechanical Properties of α-Cu Al, 67 (1976) 431–433. https://doi.org/doi:10.1515/ijmr-1976-670611.

[48] B. Chakravarti, E.A. Starke, C.J. Sparks, R.O. Williams, Short range order and the development of long range order in Ni4Mo, J. Phys. Chem. Solids. 35 (1974) 1317–1326. https://doi.org/10.1016/S0022-3697(74)80157-5.

[49] W. Schweika, H.-G. Haubold, Neutron-scattering and Monte Carlo study of short-range order and atomic interaction in ${\mathrm{Ni}}_{0.89}$${\mathrm{Cr}}_{0.11}$, Phys. Rev. B. 37 (1988) 9240–9248. https://doi.org/10.1103/PhysRevB.37.9240.

[50] A. Marucco, B. Nath, Effects of ordering on the properties of Ni-Cr alloys, J. Mater. Sci. 23 (1988) 2107–2114. https://doi.org/10.1007/BF01115776.

[51] B. Schönfeld, L. Reinhard, G. Kostorz, W. Bührer, Short-Range Order and Atomic Displacements in Ni–20 at% Cr Single Crystals, Phys. Status Solidi. 148 (1988) 457–471. https://doi.org/https://doi.org/10.1002/pssb.2221480203.

[52] H. Wood, G.D.W. Smith, A. Cerezo, Short range order and phase separation in Ti–Al alloys, Mater. Sci. Eng. A. 250 (1998) 83–87. https://doi.org/10.1016/S0921-5093(98)00540-1.

[53] R. Zhang, S. Zhao, C. Ophus, Y. Deng, S.J. Vachhani, B. Ozdol, R. Traylor, K.C. Bustillo, J.W. Morris, D.C. Chrzan, M. Asta, A.M. Minor, Direct imaging of short-range order and its impact on deformation in Ti-6Al, Sci. Adv. 5 (2019) 1–8. https://doi.org/10.1126/sciadv.aax2799.

[54] A. Radecka, P.A.J. Bagot, T.L. Martin, J. Coakley, V.A. Vorontsov, M.P. Moody, H. Ishii, D. Rugg, D. Dye, The formation of ordered clusters in Ti–7Al and Ti–6Al–4V, Acta Mater. 112 (2016) 141–149. https://doi.org/10.1016/J.ACTAMAT.2016.03.080.

[55] P. Castany, F. Pettinari-Sturmel, J. Douin, A. Coujou, TEM quantitative characterization of short-range order and its effects on the deformation micromechanims in a Ti-6Al-4V alloy, Mater. Sci. Eng. A. 680 (2017) 85–91. https://doi.org/10.1016/J.MSEA.2016.10.020.

[56] F. Pettinari, M. Prem, G. Krexner, P. Caron, A. Coujou, H.O.K. Kirchner, N. Clément, Local order in industrial and model γ phases of superalloys, Acta Mater. 49 (2001) 2549–2556. https://doi.org/10.1016/S1359-6454(01)00103-3.

[57] F. Pettinari-Sturmel, A. Coujou, N. Clément, The fluctuation of short-range order evidenced by mobile dislocations in the γ-phase of a nickel-based superalloy, Mater. Sci. Eng. A. 400–401 (2005) 114–117. https://doi.org/10.1016/j.msea.2005.02.072.

[58] A. Tamm, A. Aabloo, M. Klintenberg, M. Stocks, A. Caro, Atomic-scale properties of Ni-based FCC ternary, and quaternary alloys, Acta Mater. 99 (2015) 307–312. https://doi.org/10.1016/j.actamat.2015.08.015.

[59] R. Zhang, S. Zhao, J. Ding, Y. Chong, T. Jia, C. Ophus, M. Asta, R.O. Ritchie, A.M. Minor, Short-range order and its impact on the CrCoNi medium-entropy alloy, Nature. 581 (2020) 283–287. https://doi.org/10.1038/s41586-020-2275-z.

[60] X. Chen, Q. Wang, Z. Cheng, M. Zhu, H. Zhou, P. Jiang, L. Zhou, Q. Xue, F. Yuan, J. Zhu, X. Wu, E. Ma, Direct observation of chemical short-range order in a medium-entropy alloy, Nature. 592 (2021) 712–716. https://doi.org/10.1038/s41586-021-03428-z.

[61] C. Niu, A.J. Zaddach, A.A. Oni, X. Sang, J.W. Hurt III, J.M. LeBeau, C.C. Koch, D.L. Irving, Spin-driven ordering of Cr in the equiatomic high entropy alloy NiFeCrCo, Appl. Phys. Lett. 106 (2015) 161906. https://doi.org/10.1063/1.4918996.

[62] X.D. Xu, P. Liu, S. Guo, A. Hirata, T. Fujita, T.G. Nieh, C.T. Liu, M.W. Chen, Nanoscale phase separation in a fcc-based CoCrCuFeNiAl0.5 high-entropy alloy, Acta Mater. 84 (2015) 145–152. https://doi.org/10.1016/J.ACTAMAT.2014.10.033.

[63] A. Fantin, G.O. Lepore, A.M. Manzoni, S. Kasatikov, T. Scherb, T. Huthwelker, F. d'Acapito, G. Schumacher, Short-range chemical order and local lattice distortion in a compositionally complex alloy, Acta Mater. 193 (2020) 329–337. https://doi.org/10.1016/J.ACTAMAT.2020.04.034.

[64] F. Biermair, F. Mendez-Martin, V.I. Razumovskiy, F. Moitzi, G. Ressel, Microstructure-Property Correlation and Its Evolution during Aging in an Al4.4Co26Cr19Fe18Ni27Ti5.6 High-Entropy Alloy, Mater. 2023, Vol. 16, Page 2821. 16 (2023) 2821. https://doi.org/10.3390/MA16072821.

[65] Y. Wu, F. Zhang, X. Yuan, H. Huang, X. Wen, Y. Wang, M. Zhang, H. Wu, X. Liu, H. Wang, S. Jiang, Z. Lu, Short-range ordering and its effects on

mechanical properties of high-entropy alloys, J. Mater. Sci. Technol. 62 (2021) 214–220. https://doi.org/10.1016/j.jmst.2020.06.018.

[66] J. Ding, Q. Yu, M. Asta, R.O. Ritchie, Tunable stacking fault energies by tailoring local chemical order in CrCoNi medium-entropy alloys, Proc. Natl. Acad. Sci. U. S. A. 115 (2018) 8919–8924. https://doi.org/10.1073/pnas.1808660115.

[67] T. Neeraj, M.J. Mills, Short-range order (SRO) and its effect on the primary creep behavior of a Ti-6wt.%Al alloy, Mater. Sci. Eng. A. 319–321 (2001) 415–419. https://doi.org/10.1016/S0921-5093(01)01045-0.

[68] J.C. Fisher, On the strength of solid solution alloys, Acta Metall. 2 (1954) 9–10. https://doi.org/10.1016/0001-6160(54)90087-5.

[69] C.G. Schön, On short-range order strengthening and its role in high-entropy alloys, Scr. Mater. 196 (2021). https://doi.org/10.1016/j.scriptamat.2021.113754.

[70] V. Gerold, H.P. Karnthaler, On the origin of planar slip in f.c.c. alloys, Acta Metall. 37 (1989) 2177–2183. https://doi.org/10.1016/0001-6160(89)90143-0.

[71] Y.J. Zhang, D. Han, X.W. Li, A unique two-stage strength-ductility match in low solid-solution hardening Ni-Cr alloys: Decisive role of short range ordering, Scr. Mater. 178 (2020) 269–273. https://doi.org/10.1016/J.SCRIPTAMAT.2019.11.049.

[72] D. Han, Z.Y. Wang, Y. Yan, F. Shi, X.W. Li, A good strength-ductility match in Cu-Mn alloys with high stacking fault energies: Determinant effect of short range ordering, Scr. Mater. 133 (2017) 59–64. https://doi.org/10.1016/J.SCRIPTAMAT.2017.02.010.

[73] W.L. Bragg, The Diffraction of Short Electromagnetic Waves by a Crystal, Proc. Camb. Philol. Soc. XVII (1913).

[74] L.R. Owen, The analysis of local structural effects in alloys using total scattering and reverse Monte Carlo techniques, University of Cambridge, 2017.

[75] T. Egami, S.J.L. Billinge, Underneath the Bragg Peaks: Structural Analysis of Complex Materials, 1st ed., Pergamon, 2003. https://doi.org/10.1016/B978-0-08-097133-9.00013-7.

[76] M. von Laue, X-ray interference and mixed crystals, Ann. Phys. 56 (1918) 497–506.

[77] B. Warren, B. Averbach, B. Roberts, Atomic size effect in the X-ray scattering by alloys, J. Appl. Phys. 22 (1951) 1493–1496.

[78] P. Debye, Interferenz von Röntgenstrahlen und Wärmebewegung, Ann. Phys. 348 (1913) 49–92. https://doi.org/10.1002/ANDP.19133480105.

[79] I. Waller, Zur Frage der Einwirkung der Wärmebewegung auf die Interferenz von Röntgenstrahlen, Zeitschrift Für Phys. 17 (1923) 398–408. https://doi.org/10.1007/BF01328696/METRICS.

[80] K. Huang, X-ray reflexions from dilute solid solutions, Proc. R. Soc. A Math.

Phys. Eng. Sci. 190 (1947) 102–117.

[81] S.J.L. Billinge, The rise of the X-ray atomic pair distribution function method: A series of fortunate events, Philos. Trans. R. Soc. A Math. Phys. Eng. Sci. 377 (2019). https://doi.org/10.1098/rsta.018.0413.

[82] F. Zernike, J.A. Prins, Die Beugung von Röntgenstrahlen in Flüssigkeiten als Effekt der Molekülanordnung [The diffraction of x-rays in liquids as an effect of the molecular arrangement], Zeitschrift Für Phys. 41 (1927) 184–194. http://link.springer.com/10.1007/BF01391926.

[83] P. Debye, H. Menke, Bestimmung der inneren Struktur von Flüssigkeiten mit Röntgenstrahlen, Phys. Z. 31 (1930) 797-.

[84] L.P. Tarasov, B.E. Warren, X-ray diffraction study of liquid sodium, J. Chem. Phys. 4 (1936) 236–238.

[85] B.E. Warren, X-ray diffraction study of carbon black, J. Chem. Phys. 2 (1934) 551–555.

[86] B.E. Warren, N.S. Gingrich, Fourier integral analysis of X-ray powder patterns, Phys. Rev. 46 (1934) 368–372.

[87] J. Morgan, B.E. Warren, X-Ray analysis of the structure of water, J. Chem. Phys. 6 (1938) 666–668.

[88] B.E. Warren, H. Krutter, O. Morningstar, Fourier analysis of X-ray patterns of vitreous SiO2 and B2O3, J. Am. Chem. Soc. 19 (1936) 202–206.

[89] D.D. Kofalt, S. Nanoa, T. Egami, Differential anomalous-X-ray-scattering studies of icosahedral and amorphous Pd58.8U20.6Si20.6, Phys. Rev. Lett. 57 (1986) 114–117.

[90] D.D. Kofalt, I.A. Morrison, T. Egami, Quasicrystallinity of icosahedralPd58.8U20.6Si20.6, Phys. Rev. B. 35 (1987) 4489–4492.

[91] W. Dmowski, B.H. Toby, T. Egami, M.A. Subramanian, J. Gopalakrishnan, A.W. Sleight, Disorder in Tl plane, Phys. Rev. Lett. 61 (1988) 2608.

[92] I. Levin, V. Krayzman, J.C. Woicik, Local structure in perovskite (Ba,Sr)TiO3: reverse Monte Carlo refinements from multiple measurement techniques, Phys. Rev. B. 89 (2014) 024106.

[93] V. Petkov, M. Gateshki, M. Niederberger, Atomic-scale structure of nanocrystalline BaxSr1-xTiO3 (x = 1, 0.5, 0) by x-ray diffraction and the atomic pair distribution function technique, Chem. Mater. 18 (2006) 814.

[94] K. Page, T. Proffen, H. Terrones, Direct observation of the structure of gold nanoparticles by total scattering neutron powder diffraction, Chem. Phys. Lett. (2004) 385–388.

[95] K.M.Ø. Jensen, P. Juhas, M.A. Tofanelli, C.L. Heinecke, G. Vaughan, C.J. Ackerson, S.J.L. Billinge, Polymorphism in magic-sized Au144 (SR)60 clusters, Nat. Commun. 7 (2016) 1–8. https://doi.org/10.1038/ncomms11859.

[96] O. Lopez-Acevedo, J. Akola, R.L. Whetten, H. Grönbeck, H. Häkkinen, Structure and bonding in the ubiquitous icosahedral metallic gold cluster Au

144(SR) 60, J. Phys. Chem. C. 113 (2009) 5035–5038. https://doi.org/10.1021/jp8115098.

[97] V. Petkov, S.D. Shastri, Element-specific structure of materials with intrinsic disorder by high-energy resonant x-ray diffraction and differential atomic pair-distribution functions: A study of PtPd nanosized catalysts, Phys. Rev. B - Condens. Matter Mater. Phys. 81 (2010). https://doi.org/10.1103/PhysRevB.81.165428.

[98] X. Yang, A.S. Masadeh, J.R. McBride, E.S. Božin, S.J. Rosenthal, S.J.L. Billinge, Confirmation of disordered structure of ultrasmall CdSe nanoparticles from X-ray atomic pair distribution function analysis, Phys. Chem. Chem. Phys. 15 (2013) 8480–8486. https://doi.org/10.1039/C3CP00111C.

[99] A.S. Masadeh, E.S. Božin, C.L. Farrow, G. Paglia, P. Juhas, S.J.L. Billinge, A. Karkamkar, M.G. Kanatzidis, Quantitative size-dependent structure and strain determination of CdSe nanoparticles using atomic pair distribution function analysis, Phys. Rev. B - Condens. Matter Mater. Phys. 76 (2007) 115413. https://doi.org/10.1103/PHYSREVB.76.115413/FIGURES/10/MEDIUM.

[100] S.L.J. Thomae, N. Prinz, T. Hartmann, M. Teck, S. Correll, M. Zobel, Pushing data quality for laboratory pair distribution function experiments, Rev. Sci. Instrum. 90 (2019). https://doi.org/10.1063/1.5093714.

[101] M. Sommariva, Multi-technique approach for nanoparticles characterization on a laboratory X-Ray diffractometer, Solid State Phenom. 203–204 (2013) 17–20. https://doi.org/10.4028/www.scientific.net/SSP.203-204.17.

[102] M. Sommariva, M. Gateshki, J.A. Gertenbach, J. Bolze, U. König, B.Ş. Vasile, V.A. Surdu, Characterizing nanoparticles with a laboratory diffractometer: From small-angle to total X-ray scattering, Powder Diffr. 29 (2014) S47–S53. https://doi.org/10.1017/S0885715614001043.

[103] W. Guo, W. Dmowski, J.Y. Noh, P. Rack, P.K. Liaw, T. Egami, Local atomic structure of a high-entropy alloy: An X-Ray and neutron scattering study, Metall. Mater. Trans. A Phys. Metall. Mater. Sci. 44 (2013) 1994–1997. https://doi.org/10.1007/s11661-012-1474-0.

[104] L.R. Owen, E.J. Pickering, H.Y. Playford, H.J. Stone, M.G. Tucker, N.G. Jones, An assessment of the lattice strain in the CrMnFeCoNi high-entropy alloy, Acta Mater. 122 (2017) 11–18. https://doi.org/10.1016/j.actamat.2016.09.032.

[105] F.X. Zhang, S. Zhao, K. Jin, H. Xue, G. Velisa, H. Bei, R. Huang, J.Y.P. Ko, D.C. Pagan, J.C. Neuefeind, W.J. Weber, Y. Zhang, Local Structure and Short-Range Order in a NiCoCr Solid Solution Alloy, Phys. Rev. Lett. 118 (2017) 1–6. https://doi.org/10.1103/PhysRevLett.118.205501.

[106] Y. Ma, Q. Wang, C. Li, L.J. Santodonato, M. Feygenson, C. Dong, P.K. Liaw, Chemical short-range orders and the induced structural transition in high-entropy alloys, Scr. Mater. 144 (2018) 64–68. https://doi.org/10.1016/j.scriptamat.2017.09.049.

[107] C.L. Farrow, P. Juhas, J.W. Liu, D. Bryndin, E.S. Boin, J. Bloch, T. Proffen, S.J.L. Billinge, PDFfit2 and PDFgui: Computer programs for studying nanostructure

in crystals, J. Phys. Condens. Matter. 19 (2007). https://doi.org/10.1088/0953-8984/19/33/335219.

[108] D.A. Keen, A comparison of various commonly used correlation functions for describing total scattering, J. Appl. Crystallogr. 34 (2001) 172–177. https://doi.org/10.1107/S0021889800019993.

[109] P.F. Peterson, D. Olds, M.T. McDonnell, K. Page, Illustrated formalisms for total scattering data: A guide for new practitioners, J. Appl. Crystallogr. 54 (2021) 317–332. https://doi.org/10.1107/S1600576720015630.

[110] B.E. Warren, X-Ray Diffraction.pdf, Dover Publications, Inc., New York, 1990.

[111] P. Juhás, T. Davis, C.L. Farrow, S.J.L. Billinge, PDFgetX3: a rapid and highly automatable program for processing powder diffraction data into total scattering pair distribution functions, J. Appl. Crystallogr. 46 (2013) 560–566. https://doi.org/10.1107/S0021889813005190.

[112] V.I. Korsunskiy, R.B. Neder, A. Hofmann, S. Dembski, C. Graf, E. Rühl, Aspects of the modelling of the radial distribution function for small nanoparticles, Urn:Issn:0021-8898. 40 (2007) 975–985. https://doi.org/10.1107/S0021889807038174.

[113] K. Page, T.C. Hood, T. Proffen, R.B. Neder, Building and refining complete nanoparticle structures with total scattering data, Urn:Issn:0021-8898. 44 (2011) 327–336. https://doi.org/10.1107/S0021889811001968.

[114] P. Scherrer, Bestimmung der Größe und der inneren Struktur von Kolloidteilchen mittels Röntgenstrahlen, Nachrichten von Der Gesellschaft Der Wissenschaften Zu Göttingen, Math. Klasse. 1918 (1918) 98–100. http://eudml.org/doc/59018.

[115] R.B. Neder, T. Proffen, Diffuse Scattering and Defect Structure Simulations: A Cook Book Using the Program DISCUS, 1st ed., Oxford University Press, 2008.

[116] E.J. Mittemeijer, U. Welzel, The “state of the art” of the diffraction analysis of crystallite size and lattice strain, 223 (2008) 552–560. https://doi.org/doi:10.1524/zkri.2008.1213.

[117] J. Beyer, N. Roth, B. Brummerstedt Iversen, Effects of Voigt diffraction peak profiles on the pair distribution function, Acta Crystallogr. Sect. A, Found. Adv. 78 (2022) 10–20. https://doi.org/10.1107/S2053273321011840.

[118] N.J. Elton, P.D. Salt, Particle statistics in quantitative X-ray diffractometry, Powder Diffr. 11 (1996) 218–229. https://doi.org/10.1017/S0885715600009155.

[119] D.K. Smith, Particle statistics and whole-pattern methods in quantitative X-ray powder diffraction analysis, Powder Diffr. 16 (2001) 186–191. https://doi.org/10.1154/1.1423285.

[120] V. Petkov, Pair Distribution Functions Analysis, Charact. Mater. (2012) 1361–1372. https://doi.org/10.1002/0471266965.com159.

[121] B.H. Toby, T. Egami, Accuracy of pair distribution function analysis applied to crystalline and non-crystalline materials, Acta Crystallogr. Sect. A. 48 (1992) 336–346. https://doi.org/10.1107/S0108767391011327.

[122] R.B. Neder, T. Proffen, Exact and fast calculation of the X-ray pair distribution function, J. Appl. Crystallogr. 53 (2020) 710–721. https://doi.org/10.1107/S1600576720004616.

[123] H. Zhu, Y. Huang, J. Ren, B. Zhang, Y. Ke, A.K.Y. Jen, Q. Zhang, X.L. Wang, Q. Liu, Bridging Structural Inhomogeneity to Functionality: Pair Distribution Function Methods for Functional Materials Development, Adv. Sci. 8 (2021) 1–31. https://doi.org/10.1002/advs.202003534.

[124] P.J. Chupas, X. Qiu, J.C. Hanson, P.L. Lee, C.P. Grey, S.J.L. Billinge, Rapid-acquisition pair distribution function (RA-PDF) analysis, J. Appl. Crystallogr. 36 (2003) 1342–1347. https://doi.org/10.1107/S0021889803017564.

[125] J.D. Zea-Garcia, A.G. De la Torre, M.A.G. Aranda, A. Cuesta, A Comparative study of experimental configurations in synchrotron pair distribution function, Materials (Basel). 12 (2019) 1–15. https://doi.org/10.3390/ma12081347.

[126] D. Tsymbarenko, D. Grebenyuk, M. Burlakova, M. Zobel, Quick and robust PDF data acquisition using a laboratory single-crystal X-ray diffractometer for study of polynuclear lanthanide complexes in solid form and in solution, J. Appl. Crystallogr. 55 (2022) 890–900. https://doi.org/10.1107/S1600576722005878.

[127] P. Bordet, Application of the pair distribution function analysis for the study of cultural heritage materials, Comptes Rendus Phys. 19 (2018) 561–574. https://doi.org/10.1016/j.crhy.2018.06.001.

[128] D.A. Keen, Total scattering and the pair distribution function in crystallography, Crystallogr. Rev. 26 (2020) 141–199. https://doi.org/10.1080/0889311X.2020.1797708.

[129] G. Confalonieri, M. Dapiaggi, M. Sommariva, M. Gateshki, A.N. Fitch, A. Bernasconi, Comparison of total scattering data from various sources: The case of a nanometric spinel, Powder Diffr. 30 (2015) S65–S69. https://doi.org/10.1017/S0885715614001389.

[130] U.P. Dang, Probing Short-Range Structural Distortion of Stereochemically Active Lone Pairs in Extended Solid-State Materials, The University of Texas at Arlington, 2022.

[131] H. Ruppersberg, D. Lee, C.N.J. Wagner, Observation of chemical short-range order in an amorphous Ni 40Ti60 alloy, J. Phys. F Met. Phys. 10 (1980) 1645–1652. https://doi.org/10.1088/0305-4608/10/8/004.

[132] A.S. Masadeh, Total scattering atomic pair distribution function: new methodology for nanostructure determination, J. Exp. Nanosci. 11 (2016) 951–974. https://doi.org/10.1080/17458080.2016.1184769.

[133] P. Bordet, Local structure studies using the pair distribution function, EPJ Web Conf. 104 (2015). https://doi.org/10.1051/epjconf/201510401003.

[134] J. Te Nijenhuis, M. Gateshki, M.J. Fransen, Possibilities and limitations of X-ray diffraction using high-energy X-rays on a laboratory system, Zeitschrift Fur Krist. Suppl. 30 (2009) 163–169. https://doi.org/10.1524/zksu.2009.0023.

[135] R.K. Biswas, J. Ghosh, M. Kuttanellore, Study of Short-range Ordering in Amorphous and Nanocrystalline Materials from Laboratory based Pair Distribution Function (LPDF), Trans. Indian Ceram. Soc. 79 (2020) 158–165. https://doi.org/10.1080/0371750X.2020.1787866.

[136] C.A. Reiss, A. Kharchenko, M. Gateshki, On the use of laboratory X-ray diffraction equipment for Pair Distribution Function (PDF) studies, Zeitschrift Fur Krist. 227 (2012) 257–261. https://doi.org/10.1524/zkri.2012.1492.

[137] X. Wang, S. Tan, X.Q. Yang, E. Hu, Pair distribution function analysis: Fundamentals and application to battery materials, Chinese Phys. B. 29 (2020). https://doi.org/10.1088/1674-1056/ab6656.

[138] K. Kozma, Structural Elucidation of Metal-Oxo Systems by X-Ray Scattering Methods, Oregon State University, 2019.

[139] M. Bini, S. Ferrari, D. Capsoni, P. Mustarelli, G. Spina, F. Del Giallo, M. Lantieri, C. Leonelli, A. Rizzuti, V. Massarotti, Pair distribution function analysis and Mössbauer study of defects in microwave-hydrothermal LiFePO 4, RSC Adv. 2 (2012) 250–258. https://doi.org/10.1039/c1ra00525a.

[140] R.K. Biswas, P. Khan, S. Mukherjee, A.K. Mukhopadhyay, J. Ghosh, K. Muraleedharan, Study of short range structure of amorphous Silica from PDF using Ag radiation in laboratory XRD system, RAMAN and NEXAFS, J. Non. Cryst. Solids. 488 (2018) 1–9. https://doi.org/10.1016/j.jnoncrysol.2018.02.037.

[141] DIFFRAC.EVA | Bruker, (n.d.). https://www.bruker.com/en/products-and-solutions/diffractometers-and-x-ray-microscopes/x-ray-diffractometers/diffrac-suite-software/diffrac-eva.html (accessed May 9, 2023).

[142] A.K. Soper, E.R. Barney, Extracting the pair distribution function from white-beam X-ray total scattering data, Urn:Issn:0021-8898. 44 (2011) 714–726. https://doi.org/10.1107/S0021889811021455.

[143] D. Olds, C.N. Saunders, M. Peters, T. Proffen, J. Neuefeind, K. Page, Precise implications for real-space pair distribution function modeling of effects intrinsic to modern time-of-flight neutron diffractometers, Acta Crystallogr. Sect. A Found. Adv. 74 (2018) 293–307. https://doi.org/10.1107/S2053273318003224.

[144] C.L. Farrow, P. Juhas, J.W. Liu, D. Bryndin, E.S. Bozin, J. Bloch, T. Proffen, S.J.L. Billinge, PDFgui user guide, PDFGUI User Guid. (2009).

[145] E112 Standard Test Methods for Determining Average Grain Size, (n.d.). https://www.astm.org/e0112-13r21.html (accessed May 15, 2023).

[146] R.L. Higginson, C.M. Sellars, Worked Examples in Quantitative Metallography, Maney, 2003. https://books.google.at/books?id=29ZGAAAAYAAJ.

[147] N. Schell, A. King, F. Beckmann, T. Fischer, M. Müller, A. Schreyer, The High Energy Materials Science Beamline (HEMS) at PETRA III, Mater. Sci. Forum. 772 (2014) 57–61. https://doi.org/10.4028/www.scientific.net/MSF.772.57.

[148] R.W.G. Wyckoff, Crystal Structures, Vol. 1, 2nd ed., Interscience Publishers,

New York, 1963.

[149] C. Prescher, V.B. Prakapenka, DIOPTAS: A program for reduction of two-dimensional X-ray diffraction data and data exploration, High Press. Res. 35 (2015) 223–230. https://doi.org/10.1080/08957959.2015.1059835.

[150] Band-pass filtering by Difference of Gaussians — skimage v0.20.0 docs, (n.d.). https://scikit-image.org/docs/stable/auto_examples/filters/plot_dog.html (accessed May 10, 2023).

[151] G.K. Wertheim, M.A. Butler, K.W. West, D.N.E. Buchanan, Determination of the Gaussian and Lorentzian content of experimental line shapes, Rev. Sci. Instrum. 45 (1974) 1369–1371. https://doi.org/10.1063/1.1686503.

[152] R.A. Young, D.B. Wiles, IUCr, Profile shape functions in Rietveld refinements, Urn:Issn:0021-8898. 15 (1982) 430–438. https://doi.org/10.1107/S002188988201231X.

[153] Built-in Fitting Models in the models module — Non-Linear Least-Squares Minimization and Curve-Fitting for Python, (n.d.). https://lmfit.github.io/lmfit-py/builtin_models.html#lmfit.models.PseudoVoigtModel (accessed May 15, 2023).

[154] J.J. Olivero, R.L. Longbothum, Empirical fits to the Voigt line width: A brief review, J. Quant. Spectrosc. Radiat. Transf. 17 (1977) 233–236. https://doi.org/10.1016/0022-4073(77)90161-3.

[155] L. Lutterotti, S. Matthies, H. Wenk, MAUD: a friendly Java program for material analysis using diffraction, (1999).

[156] S. Graulis, D. Chateigner, R.T. Downs, A.F.T. Yokochi, M. Quirós, L. Lutterotti, E. Manakova, J. Butkus, P. Moeck, A. Le Bail, Crystallography Open Database – an open-access collection of crystal structures, Urn:Issn:0021-8898. 42 (2009) 726–729. https://doi.org/10.1107/S0021889809016690.

[157] G. Caglioti, A. Paoletti, F.P. Ricci, Choice of collimators for a crystal spectrometer for neutron diffraction, Nucl. Instruments. 3 (1958) 223–228. https://doi.org/10.1016/0369-643X(58)90029-X.

[158] H.M. Rietveld, A profile refinement method for nuclear and magnetic structures, J. Appl. Crystallogr. 2 (1969) 65–71. https://doi.org/10.1107/S0021889869006558.

[159] B.H. Toby, R factors in Rietveld analysis: How good is good enough?, Powder Diffr. 21 (2006) 67–70. https://doi.org/10.1154/1.2179804.

[160] G. Ressel, F. Biermair, S. Fellner, C. Gammer, V.I. Razumovskiy, Design of Laves phase-reinforced compositionally complex alloy, Sci. Rep. 13 (2023) 16874. https://doi.org/10.1038/s41598-023-43722-6.

[161] T. Proffen, S. Billinge, PDFFIT 1.2 Users Guide, (2003).

[162] Lab Report XRD 87: PDF Analysis with the D8 ADVANCE, (2016) 4.

[163] Y. Yang, H. Su, T. Wu, Y. Jiang, D. Liu, P. Yan, H. Tian, H. Yu, Atomic pair

distribution function research on Li 2 MnO 3 electrode structure evolution, Sci. Bull. 64 (2019) 553–561. https://doi.org/10.1016/j.scib.2019.03.019.

[164] Lab Report XRD 90: PDF Analysis with D8 ADVANCE, (2018) 4.

[165] R.K. Biswas, P. Khan, A.K. Mukhopadhyay, J. Ghosh, M. Kuttanellore, Laboratory X-ray diffractometer for PDF experiments using Ag radiation, Acta Crystallogr. Sect. A Found. Adv. 73 (2017) C885–C885. https://doi.org/10.1107/s2053273317086892.

[166] V. Petkov, I.K. Jeong, J.S. Chung, M.F. Thorpe, S. Kycia, S.J.L. Billinge, High real-space resolution measurement of the local structure of Ga1-xInxAs using X-Ray diffraction, Phys. Rev. Lett. 83 (1999) 4089–4092. https://doi.org/10.1103/PhysRevLett.83.4089.

[167] T. Proffen, V. Petkov, S.J.L. Billinge, T. Vogt, Chemical short range order obtained from the atomic pair distribution function, Zeitschrift Fur Krist. 217 (2002) 47–50. https://doi.org/10.1524/zkri.217.2.47.20626.

[168] S. Engberg, J. Symonowicz, J. Schou, S. Canulescu, K.M.Ø. Jensen, Characterization of Cu2ZnSnS4 Particles Obtained by the Hot-Injection Method, ACS Omega. 5 (2020) 10501–10509. https://doi.org/10.1021/acsomega.0c00657.

[169] D. Tsymbarenko, D. Grebenyuk, M. Burlakova, M. Zobel, Supporting information for article: Quick and robust PDF data acquisition using a laboratory single-crystal X-ray diffractometer for study of polynuclear lanthanide complexes in solid form and in solution, J. Appl. Crystallogr. 55 (2022) 890–900. https://doi.org/10.1107/S1600576722005878.

[170] M.G. Tucker, D.A. Keen, M.T. Dove, A.L. Goodwin, Q. Hui, RMCProfile: Reverse Monte Carlo for polycrystalline materials, J. Phys. Condens. Matter. 19 (2007). https://doi.org/10.1088/0953-8984/19/33/335218.

[171] A. Cervellino, R. Frison, Texture corrections for total scattering functions, Acta Crystallogr. Sect. A Found. Adv. 76 (2020) 302–317. https://doi.org/10.1107/S2053273320002521.

[172] M. Ou, Y. Ma, H. Ge, W. Xing, Y. Zhou, S. Zheng, K. Liu, Microstructure evolution and mechanical properties of a new cast Ni-base superalloy with various Ti contents, J. Alloys Compd. 735 (2018) 193–201. https://doi.org/https://doi.org/10.1016/j.jallcom.2017.11.074.

[173] A. Takeuchi, A. Inoue, Classification of Bulk Metallic Glasses by Atomic Size Difference, Heat of Mixing and Period of Constituent Elements and Its Application to Characterization of the Main Alloying Element, Mater. Trans. 46 (2005) 2817–2829. https://doi.org/10.2320/MATERTRANS.46.2817.

[174] S. Dasari, A. Jagetia, A. Sharma, M.S.K.K.Y. Nartu, V. Soni, B. Gwalani, S. Gorsse, R. Banerjee, Tuning the degree of chemical ordering in the solid solution of a complex concentrated alloy and its impact on mechanical properties, Acta Mater. 212 (2021) 116938. https://doi.org/10.1016/j.actamat.2021.116938.